Description of the Response of Reactor First Walls to Pulsed Thermonuclear Radiation (Part I)

T.O. Hunter and G.L. Kulcinski

February 1977

UWFDM-196

FUSION TECHNOLOGY INSTITUTE

UNIVERSITY OF WISCONSIN

MADISON WISCONSIN

Description of the Response of Reactor First Walls to Pulsed Thermonuclear Radiation (Part I)

T.O. Hunter and G.L. Kulcinski

Fusion Technology Institute
University of Wisconsin
1500 Engineering Drive
Madison, WI 53706

http://fti.neep.wisc.edu

February 1977

UWFDM-196

Description of the Response of Reactor First Walls to Pulsed Thermonuclear Radiation (Part I)

Thomas O. Hunter*
G. L. Kulcinski

March 1977

UWFDM-196

* Member Technical Staff, Sandia Laboratories, Albuquerque, NM 87115
Work partially supported by Department of Energy.

Fusion Research Program
Nuclear Engineering Department
University of Wisconsin
Madison, Wisconsin 53706

Abstract

This document is the initial segment in a general treatment of the response of materials to transient irradiation from thermonuclear sources. Its function is to develop the background material relating to the interaction mechanisms and commensurate displacement, thermal and stress responses which occur when materials are irradiated with neutron, photon, and ion pulses. In addition, the methodology for an analysis of the synergistic effect of these responses on materials is outlined. Subsequent publications will deal with preliminary results of such an analysis or with more detailed developments related to some of the specific phenomena involved.

TABLE OF CONTENTS

I. INTRODUCTION

The development of the technology for the confinement of a plasma which has sufficient density and temperature to achieve thermonuclear conditions has resulted in several alternative approaches to production of useful energy from controlled fusion. A principal distinction between these approaches is the time scale over which the energy is released from the thermonuclear reaction. The duration and magnitude of this energy release will determine the response of materials which are used in the design of a fusion reactor. Of particular interest is response of "first wall" materials which are directly exposed to the radiation from the fusion source.

In this document, the background material for a self consistent evaluation of the response of first wall materials to pulsed irradiation from thermonuclear sources will be developed. The analysis will include those initial responses due to primary interaction of radiation with wall materials as well as the longer term response when equilibrium is approached. Emphasis will be placed on the synergism between the thermal, stress and displacement damage responses and on the interaction of these transient states on subsequent effects.

I.1 Phenomenology and Spectral Sensitivity

The phenomenology associated with transient irradiation in a fusion environment is outlined in Figure 1. A necessary input to determine the multitude of associated response modes is a description of the irradiation source and a description of a first wall concept.

The primary pulsed fusion source radiation can be described by the spectra of neutron, charged particles, or photons produced in each pulse. The neutron spectrum will be determined by the fusing nuclei, the source density, and any non-fusing nuclei present in the source. The energy range of interest is limited to about 15 Mev.

The charged particle spectra from a thermonuclear source will consist of the fusing nuclei, product nuclei and non-fusing species. The range will be limited to approximately the maximum kinetic energy given to a product nucleus in a fusion reaction.

The photon spectrum will be determined by the confinement mechanism, source temperature, and the species present. For most short pulse duration systems, the energy range of interest for photons is up to about 100 Kev. However, higher energy photons will interact with the first wall

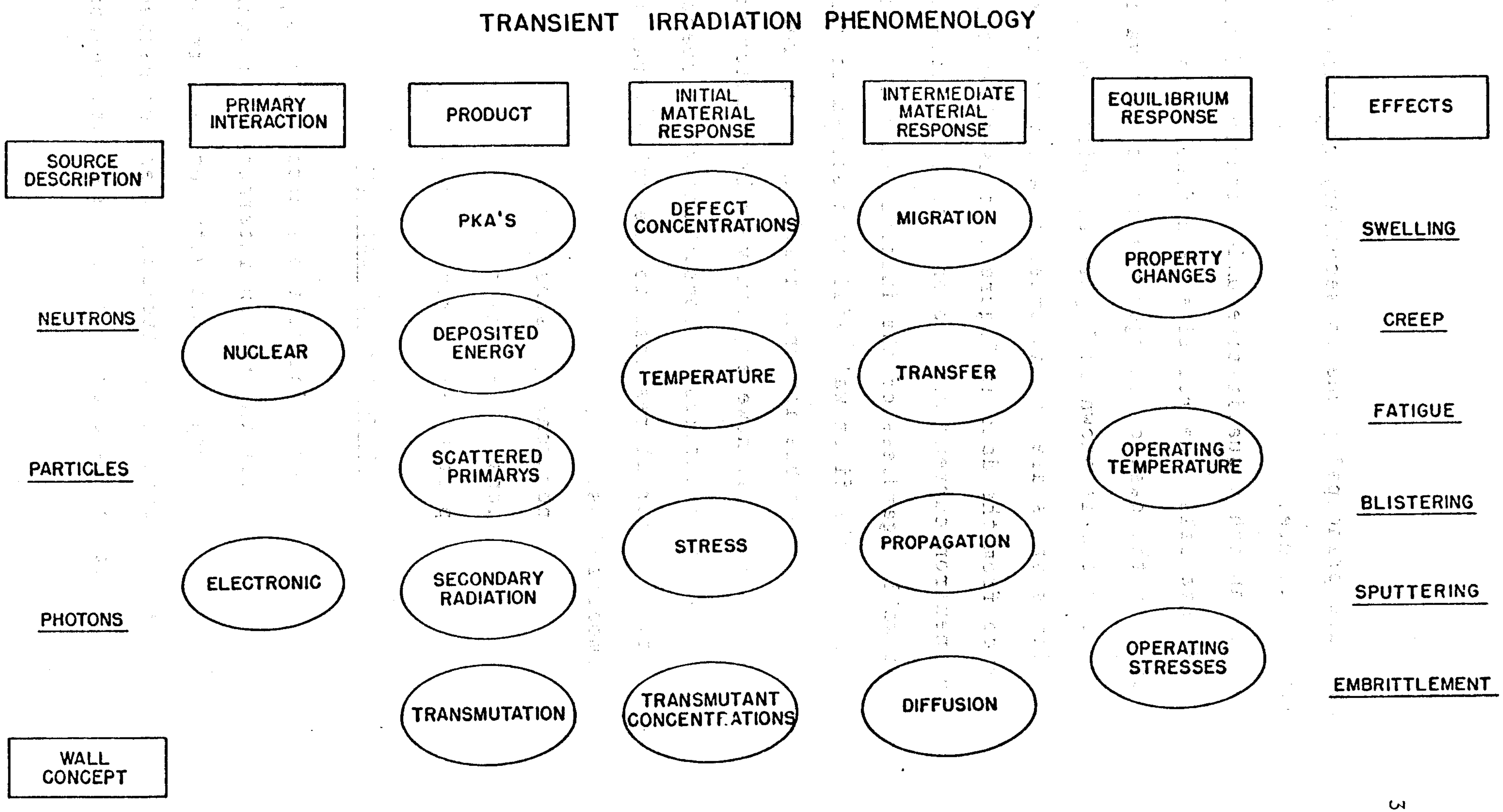
TRANSIENT IRRADIATION PHENOMENOLOGY
SOURCE DESCRIPTION
NEUTRONS
PARTICLES
PHOTONS
WALL CONCEPT
PRIMARY INTERACTION
NUCLEAR
ELECTRONIC
PRODUCT
PKA'S
DEPOSITED ENERGY
SCATTERED PRIMARYS
SECONDARY RADIATION
TRANSMUTATION
INITIAL MATERIAL RESPONSE
DEFECT CONCENTRATIONS
TEMPERATURE
STRESS
TRANSMUTANT CONCENTRATIONS
INTERMEDIATE MATERIAL RESPONSE
MIGRATION
TRANSFER
PROPAGATION
DIFFUSION
EQUILIBRIUM RESPONSE
PROPERTY CHANGES
OPERATING TEMPERATURE
OPERATING STRESSES
EFFECTS
SWELLING
CREEP
FATIGUE
BLISTERING
SPUTTERING
EMBRITTLEMENT

Figure 1

but they are principally due to secondary radiation such as neutron capture.

To establish a qualitative understanding of the response of materials, the relative mean free paths in carbon (range in the case of charged particles) for various energy radiations is shown in Figure 2. First walls for most fusion systems are on the order of a few mm in thickness, hence from the data in Figure 2 it is clear that the incident neutron current will be only slightly affected by the first wall regardless of the initial neutron spectrum. The ion flux on the first wall will be absorbed in the first 10 μm for all reasonable ion energies. The mean free path of the energetic photons, however, can vary by a factor of 10^7 over the energy range of interest. Consequently the spectral sensitivity of material response to the primary radiation can be summarized as:

neutrons -- insensitive
ions -- sensitive
photons -- extremely sensitive

I.2 Interaction Chronology

The primary interaction of the source neutrons is with the target nuclei while the photon interaction is with target electrons and ions interact with both electrons and nuclei. The partitioning of interaction energy between nuclei and electrons is crucial to the ultimate response of

MEAN FREE PATH AND RANGE OF FUSION IRRADIATIONS IN CARBON

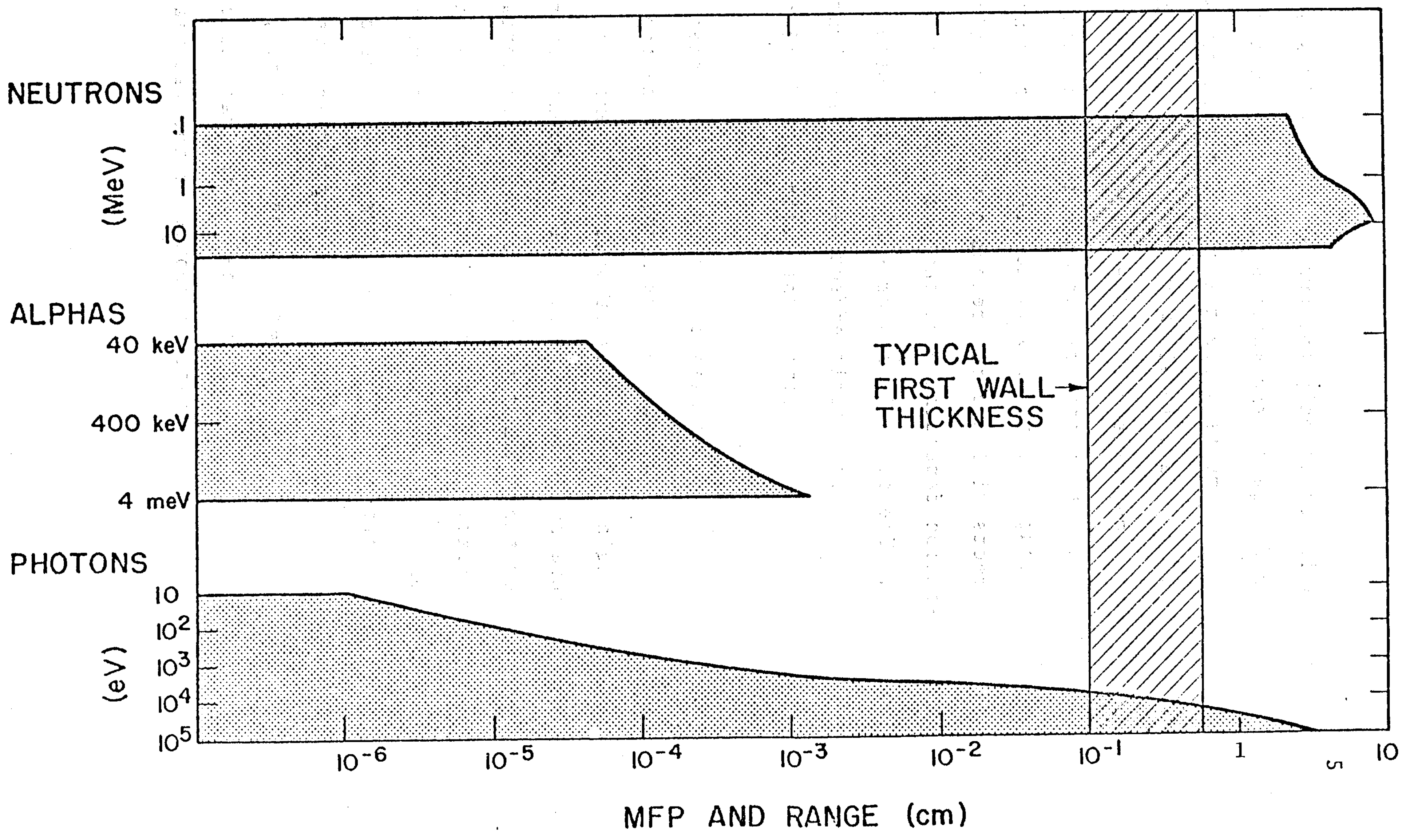

Figure 2

the material since only the nuclear energy losses will result in damage to the material structure in the form of atomic displacements while the electronic energy will produce ionization and local deposition of energy (heat).

The damage energy is given first to primary-knock-ons (PKA's) which then produce subsequent displacements as they travel through the material. The resulting concentration of point defects will undergo recombination, migration, and agglomeration depending upon the microstructure of the material. The accumulation of single and clustered defects can result in macroscopic effects such as swelling, creep, etc.,[1] which will determine the ultimate life of the first wall material.

The above processes do not occur independently from the thermodynamic state of the material since the destiny of the original defects is strongly influenced by the local temperature and stress state. The electronic energy deposited by the radiation source is also a potential source for the creation of local temperature and stress transients. The ultimate temperature history will be determined by the energy deposition time and the thermal response of the material, and an equilibrium operating temperature is approached following each energy pulse. Similarly, the stress history will be determined by the rate of energy deposition and the elastic response of the material.

I.3 Pulsed Fusion Systems

With the possible exception of mirrors, most confinement systems for thermonuclear fusion operate in a pulsed mode. Tokamak systems operate in a pseudo steady state manner but are limited in pulse duration by impurity buildup in the plasma and the available magnetic flux for plasma current. Theta pinches utilize pulsed magnetic fields for implosion heating and adiabatic compression of a toroidal plasma. These fields are programmed so that the ignited plasma will expand against the field but not be allowed to reach the first wall. Pulse durations are consequently on the order of 0.1 second.

Inertial confinement systems, which include lasers, electron beams and ion beams, rely on the rapid deposition of energy in the periphery of a small fuel pellet. This energy will cause the pellet to be compressed and heated to thermonuclear conditions. The duration of the power pulse is determined by the time necessary for hydrodynamic expansion to a state where temperatures and densities are insufficient for significant energy production.

Conceptual design studies have been performed for each of the above confinement schemes.[2-5] A general comparison of the burn characteristics and neutron wall loading is shown in Table 1 and it reveals the relative time scales over which the systems operate. Comparisons of different inertial confinement schemes will be made in later sections.

TABLE 1

PULSED FUSION SOURCE CHARACTERISTICS FROM TYPICAL FUSION REACTOR DESIGNS

	Tokamak(2)	Theta Pinch(3)	Laser(4)
Thermonuclear Burn Time (sec)	1800	0.07	10^{-11} - 10^{-10}
Thermonuclear Energy/pulse (GJ)	7300	30	0.10
Wall area (m^2)	1300	1100	310
14 Mev Fluence /pulse (n/cm^2)	$2x10^{17}$	$8.9x10^{14}$	$1.1x10^{13}$
Peak wall current (n/cm^2-sec)	$1.1x10^{14}$	$1.1x10^{16}$	$1.0x10^{21}$
Time Between Burns (sec)	100	10	.01
Average 14 Mev Neutron Wall Loading (MW/m^2)	2.5	2.0	2.5

The dynamic response of a first wall to pulsed radiation sources can only be significantly different from the steady state response if the duration of the loading pulse is smaller or the same order as the response time of interest. Consequently, the systems most likely to have a significant dynamic response contribution will be the inertial confinement approaches. The remainder of the discussion will address the phenomenology associated with these systems.

In inertial confinement systems only about 75% of the thermonuclear energy is released from the source in the form of high energy neutrons. The remainder of the energy will be distributed between the pellet debris, the reaction products, and attendant electromagnetic radiation. In addition, a portion of the energy from the compression source can be redirected towards the walls. As a result reflected laser light, scattered electrons, and ions can also contribute to the environment which a first wall encounters. This partitioning of energy between various form is discussed in Section V.1.

I.4 Pulsed Radiation Damage

Traditionally, radiation damage has been associated with those phenomena which arise from neutron irradiation of materials at low (10^{-7} to 10^{-6} DPA/sec) displacement rate which are in a uniform stress and temperature state. Such conditions are encountered in a fission reactor and in a pseudo steady state fusion reactor. The primary responses to such irradiation are displacement damage and transmutation reactions. These primary interactions lead to the subsequent phenomena as outlined in Figure 1 of sputtering, swelling, electrical resistivity changes, embrittlement, creep and compositional change.

Some of the phenomena are considered to be rate dependent and such dependence is usually characterized by the displacement rate or the rate of primary interaction. To a first approximation the displacement rate is proportional to the instantaneous flux in a material; however, the neutron spectrum can cause significant modification to the displacement rate (as measured by surviving defects) especially as more energetic neutrons are present. A qualitative comparison of displacement rates for metals for various environments in which displacement damage has been observed or is anticipated is given by Table 2.[6,7]

The effect of these various damage rates on specific phenomena such as swelling has recently been investigated.[8] Significantly different responses are observed; for example, there is a significant shift in the swelling vs. temperature behavior as the displacement rate is increased for the same total number of displacements.

An aspect of damage production which is more pertinent to inertial confinement systems is the pulsed nature of

TABLE 2

COMPARISON OF INSTANTANEOUS DISPLACEMENT RATES IN SOLID COMPONENTS OF NUCLEAR SYSTEMS

	dpa/sec
Tokamak Fusion First Wall	3×10^{-7}
Thermal Fission cladding	10^{-7}
Fast Fission-cladding	10^{-6}
Θ-pinch*	3×10^{-5}
HV Electron Microscope	10^{-3}
Heavy Ion Bombardment	10^{-4}-10^{-1}
Laser Fusion First Wall*	1-10

*Neutrons only.

the radiation. Damage is produced at very high rates for a short interval of time followed by a quiescent phase in which the material is free to respond with no driving source. Both the duration of the pulse and the interval between pulses can be of the same order as the life times of the interstitials and vacancies whose migration ultimately determines the swelling of an irradiated material. In addition, the defect migration is occurring during a period in which the temperature is oscillating with the frequency of the radiation pulses. A comparison of interstitial and vacancy life times with the pulse durations and pulse intervals for various temperatures in a typical metal (Cu) is shown in Figure 3. From this comparison it can be noted that neutron pulse durations are on the order of the interstitial lifetimes while subsequent pulses occur on the order of the vacancy lifetimes. In addition fluctuations in temperature have a slight effect on interstitial response and a significant effect on vacancy response. This effect is directly attributable to a factor of 20 difference in free energy of migration[9] between the two species.

The effect of short pulses of high displacement rates on swelling is currently being investigated by Ghoniem[10] under conditions of constant temperature and stress. That study is indicating that significant modification to swelling behavior can be expected if pulses are short (10^{-8} sec) and pulse intervals are on the order of 10^{-1} seconds at high temperatures. The emphasis of the investigation proposed in this paper will be to establish the transient temperature and stress conditions associated with the damage pulses and to estimate the effect on the swelling response due to the synergism of the effects. This relationship is shown schematically in Figure 4.

Figure 3

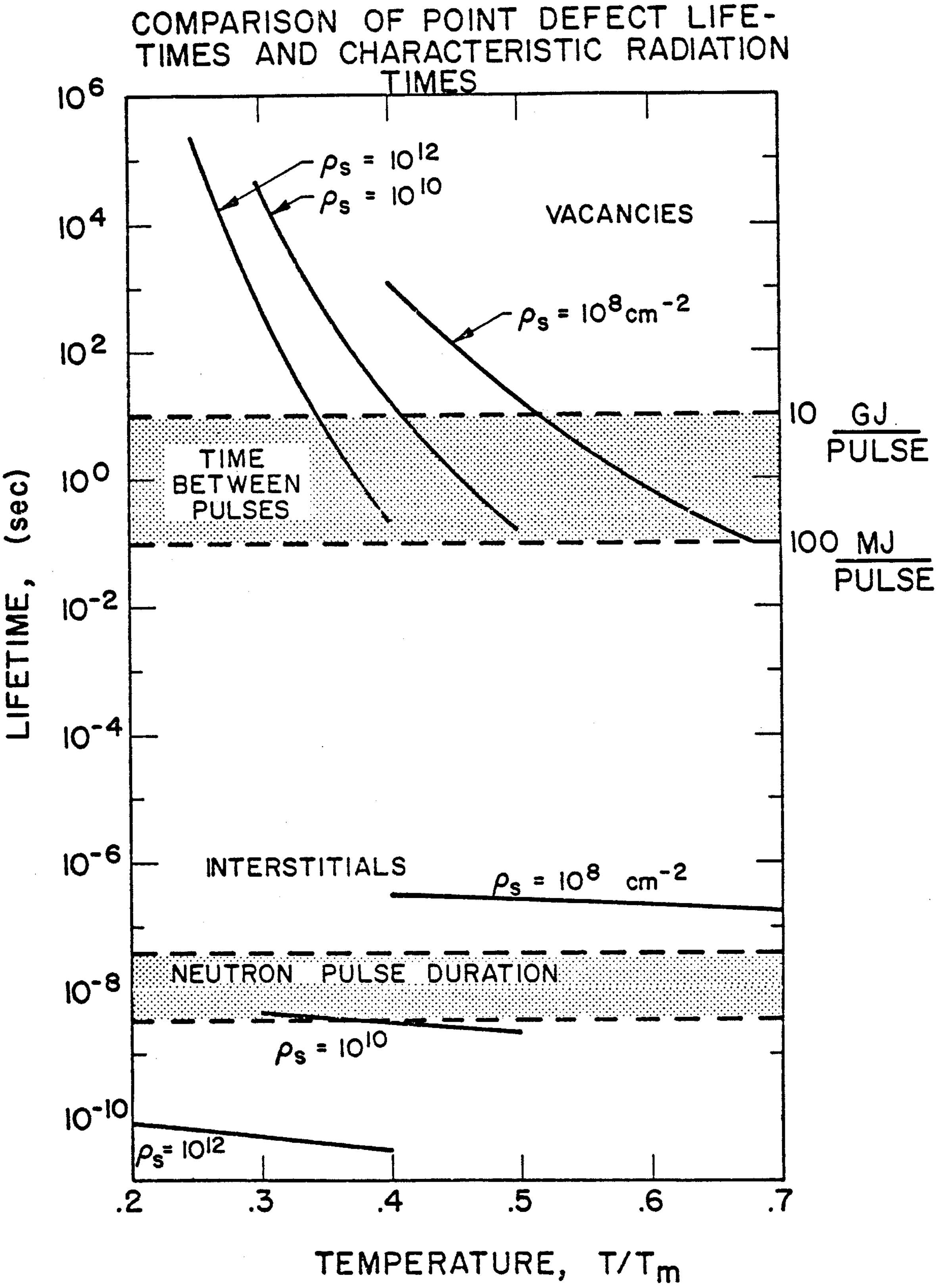
COMPARISON OF POINT DEFECT LIFETIMES AND CHARACTERISTIC RADIATION TIMES
LIFETIME, (sec)
TEMPERATURE, T/Tm
10^6
10^4
10^2
10^0
10^-2
10^-4
10^-6
10^-8
10^-10
.2
.3
.4
.5
.6
.7
VACANCIES
ρs = 10^12
ρs = 10^10
ρs = 10^8 cm^-2
TIME BETWEEN PULSES
10 GJ/PULSE
100 MJ/PULSE
INTERSTITIALS
ρs = 10^8 cm^-2
NEUTRON PULSE DURATION
ρs = 10^10
ρs = 10^12

Figure 4

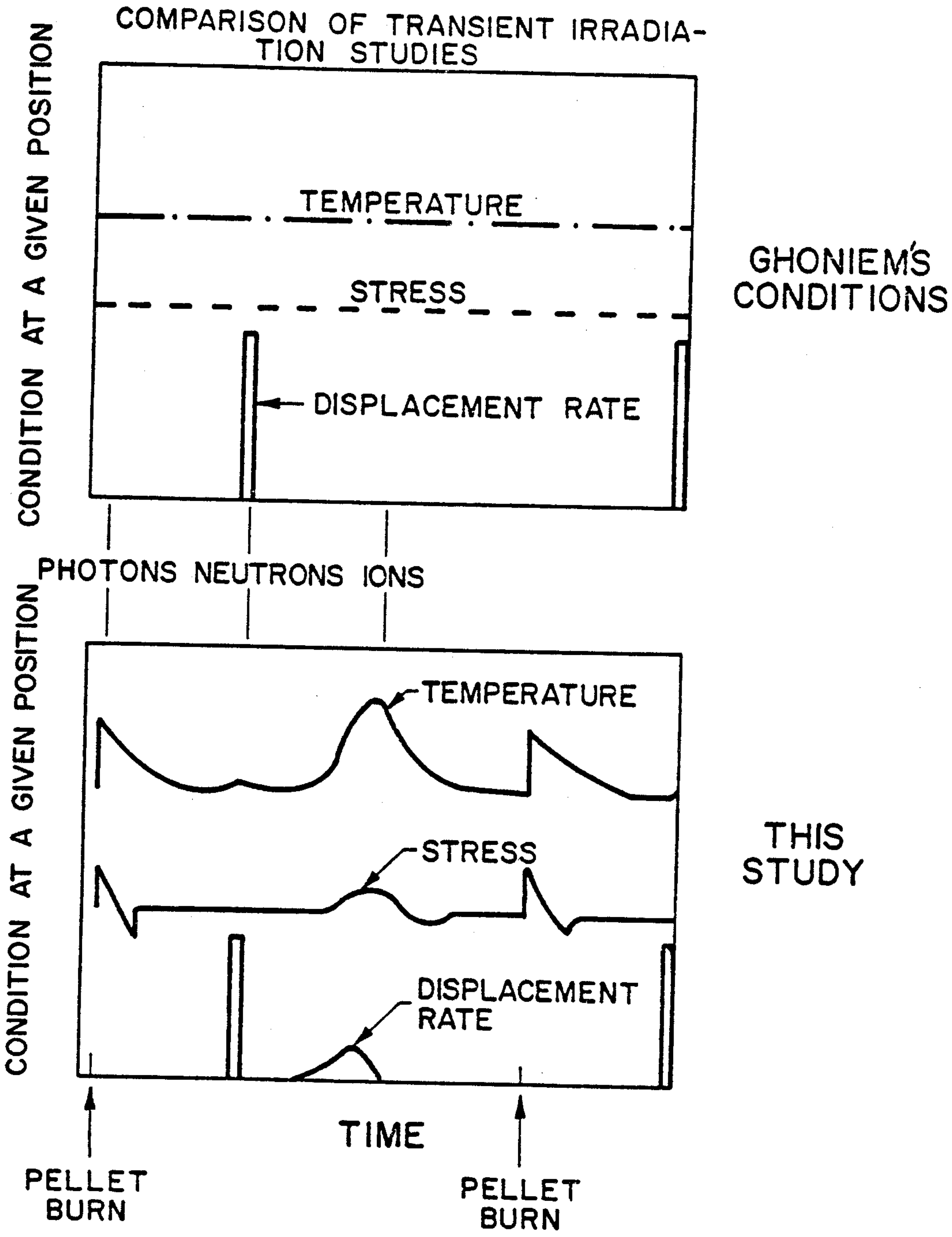
COMPARISON OF TRANSIENT IRRADIATION STUDIES
CONDITION AT A GIVEN POSITION
TEMPERATURE
STRESS
DISPLACEMENT RATE
GHONIEM'S CONDITIONS
PHOTONS
NEUTRONS
IONS
CONDITION AT A GIVEN POSITION
TEMPERATURE
STRESS
DISPLACEMENT RATE
THIS STUDY
TIME
PELLET BURN
PELLET BURN

I.5 Pulsed Material Response

That portion of the energy of incident radiation which is deposited as internal energy in the first wall will give rise to both temperature and stress excursions. The magnitude of the temperature excursion will depend on the rate of energy deposition at a given location versus the rate at which energy is lost by heat transfer from that point. It will be shown in subsequent sections that energy deposition from neutron and photon irradiation is sufficiently fast so that it may be approximated by impulse sources. On the other hand, significant heat conduction can take place over the long durations of ion irradiation.

Stress transients can be induced in the first wall due to either of two manifestations of the same basic phenomena. The first is a thermoelastic response to the deposition of energy. If the material is heated faster than its characteristic thermal expansion time, local stresses will develop which are then relieved as stress waves propagate throughout the material. The second is the creation of stress waves in response to an ablation of the surface due to energy deposition in excess of that required for incipient vaporization. This material will "blow off" and there will be an impulse imparted to the remaining solid surface equal to the momentum in the ablated material.

Both the stress and thermal response to various types of radiation can be determined from any of a number of computer codes[11,12] which can calculate the energy flow and the hydrodynamic or elastic response of materials subject to time dependent energy deposition or other boundary conditions. These methods are not well suited to calculating synergistic response of many radiation pulses nor are they efficient in performing parameter studies for variation in radiation spectra, for example.

This study will address the response of dry first walls in which ablation is not a consideration and hence stresses will be due to thermoelastic response only. The emphasis will be on efficient (analytical, where possible) solutions which can be performed for a large number of radiation spectra with a minimum of calculational effort.

II. ANALYSIS METHODOLOGY

This analysis will address computational techniques which will determine for a given pulsed thermonuclear source the combined thermal, stress and displacement damage response of a fusion reactor first wall. These techniques should allow arbitrary specification of the source spectra for neutron, ion, and photon radiation. Upon determining these conditions as functions of position and time, the implications upon subsequent phenomena which will affect the usefulness of candidate materials can be investigated with specific attention given to void swelling. With a self consistent analytical technique, an assessment of the sensitivity of first wall response to source output spectra and material description can be made. This process is displayed diagramatically in Figure 5.

Figure 5

TRANSIENT IRRADIATION
ANALYSIS
METHODOLOGY

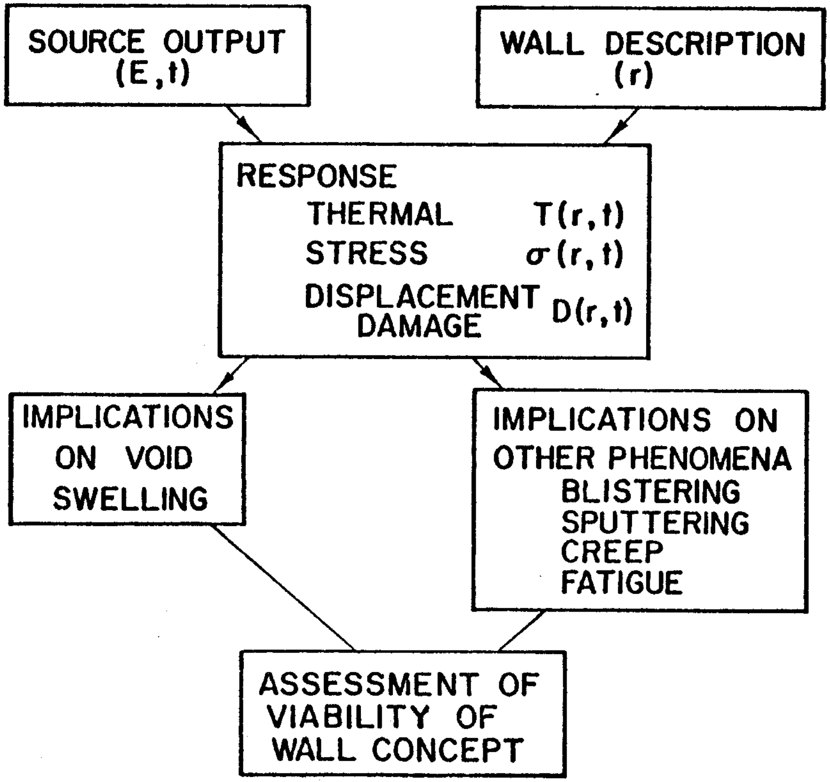

III. PURPOSE AND UTILITY

In addition to performing a correlation between the primary responses of a fusion first walls, the following applications for the proposed analysis have been identified:

a) Assess performance of candidate fusion first wall designs.

Various first walls, mirrors, insulators, or liners can be examined to determine optimum choices for pulsed fusion reactor concepts which do not employ ablative wall protection. In addition, allowable wall radii can be specified by determining the maximum radiation fluences.

b) Assess effectiveness of wall protection schemes.

Protection schemes which stop or partially block the source radiation can be evaluated in terms of reduction of first wall response. Potential schemes include magnetic protection, liners, and gaseous layers.

c) Evaluate the effectiveness of simulation schemes.

Simulation schemes, which are proposed to test materials prior to implementation of fusion reactors, can be evaluated in terms of the response provided relative to the total synergistic response in an actual reactor exposure. In addition, structural materials for simulation devices can be evaluated.

d) Evaluate rate effects on specific phenomena.

Information on the transient temperature and stress states in a wall material will allow specification of the conditions which can enhance other effects such as blistering or swelling.

e) Evaluate transient gas diffusion histories.

The transport of injected gas (He, T, D) and transmutation products (He, H, etc.) can be more accurately determined since the transient conditions which influence the diffusivity can be specified.

f) Evaluation of transients in magnetically confined systems.

Rapid energy releases in normally steady state devices such as plasma dumps in Tokamaks can be evaluated in terms of effect on the first wall.

IV. BASIC PRINCIPLES

Before outlining the different responses to pulsed irradiation, it is necessary to summarize the basic principles of radiation interactions. In this section the absorption or attenuation parameters for photon, ion, and neutron interaction will be examined. The response to this energy deposition will be developed in section VI.

IV.1 Photon Interactions

The first walls of inertially confined fusion reactors will encounter photon radiation which ranges from a few electron volts to a few million electron volts. The general relationship of these radiations to the electromagnetic spectrum is shown in Figure 6.

The primary interaction of photons with materials in these energy ranges are:

photoelectric effect
coherent scattering
incoherent scattering
pair production

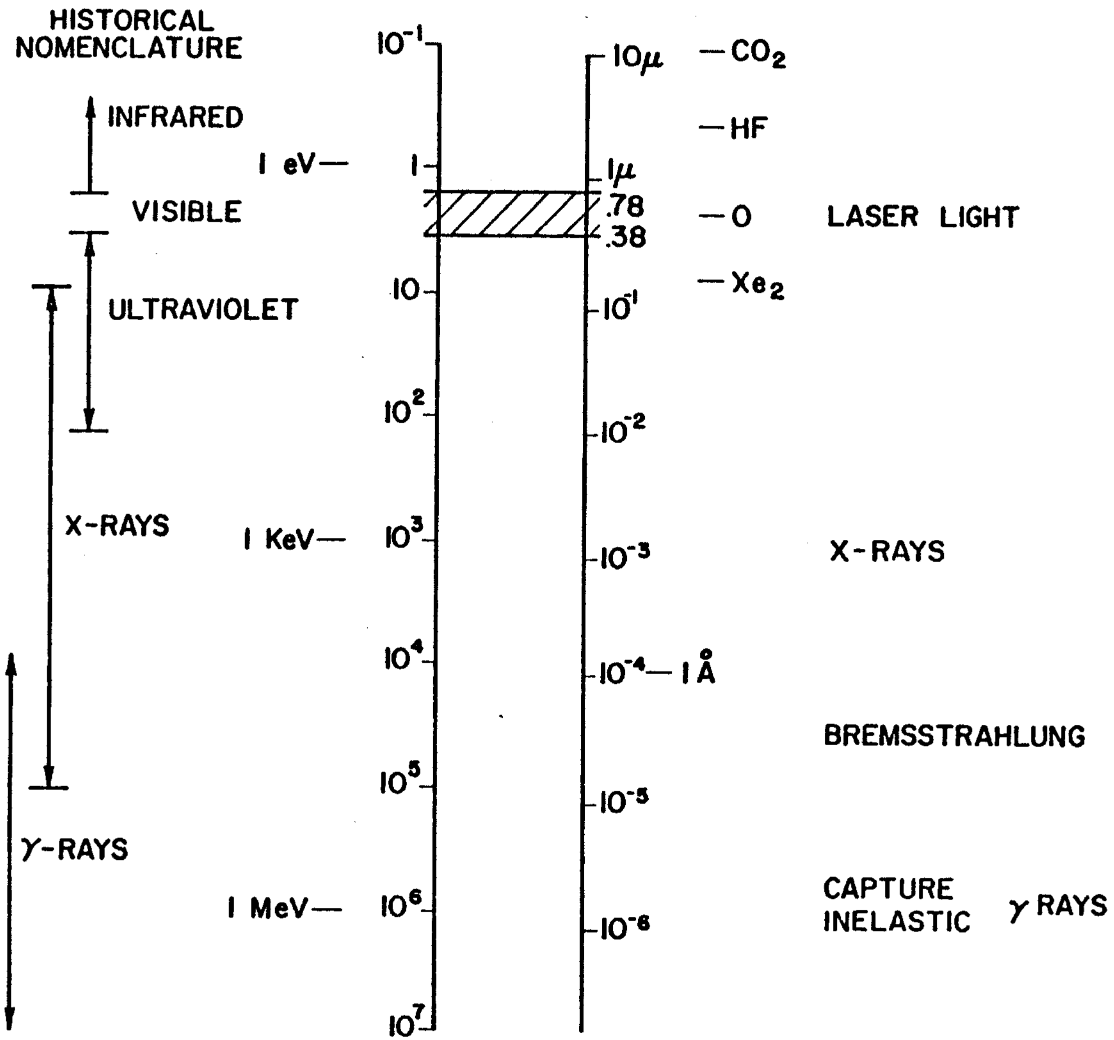

ELECTROMAGNETIC SPECTRUM

Figure 6

Cross sections for each of these reactions have been tabulated in various forms[13-15] and are available for numerical calculations. A brief discussion of the material and spectral dependence of the cross sections is, however, appropriate before development of material response from the radiation.

IV.1.1 Pair Production

At the high energy end of the spectrum pair production will be the dominant contributor to the total cross section. The pair production process is a photon-matter reaction which occurs when the electric field of the photon interacts with the electric field of an atomic nucleus. The incident photon is destroyed and a positron - negatron electron pair is created. Mathematically[16] the theory is similar to the bremsstrahlung process in which an electron undergoes a transition in which an photon is emitted. In pair production the photon is absorbed and an electron undergoes a transition out of a negative energy state into a positive energy state leaving a hole in the negative state or a positron. The reaction necessarily has a threshold energy of $2\ m_0c^2$ (1.02 MeV).

The interaction rate is dependent on the nuclear cross section and is therefore proportional to Z^2 of the absorbing material. Both the differential cross section in relation to the energy shared by the position and the total cross section, obtained by integrating over all positron energies, have analytic expressions[16] and accurate approximations.[17] Since the process is a nuclear interaction, the cross section is simply proportional to the nuclei density and Z^2 as above. A reasonable approximation (except for minor screening correction at high energies) for the total cross section can be determined as a function of a standard cross section for a material such as lead as:[16]

1) $$\mu_{pp} = \frac{\rho}{11.35} \frac{207.2}{A} \left(\frac{Z}{82}\right)^2 \mu_{pp}^{Pb}$$

where μ_{pp} = pair production attenuation coefficient (cm^{-1})

ρ = material density (g/cm^3)

A = atomic weight (amu)

Z = atomic number

and μ_{pp}^{Pb} is given by Figure 7.

The energy absorbed is normally taken as the kinetic energy of the electron-positron pair as:

2) $$\mu_a^{pp} = \mu\left(1 - \frac{2m_oc}{E}\right)$$

where μ_a^{pp} = pair production energy absorption coefficient

E = photon energy

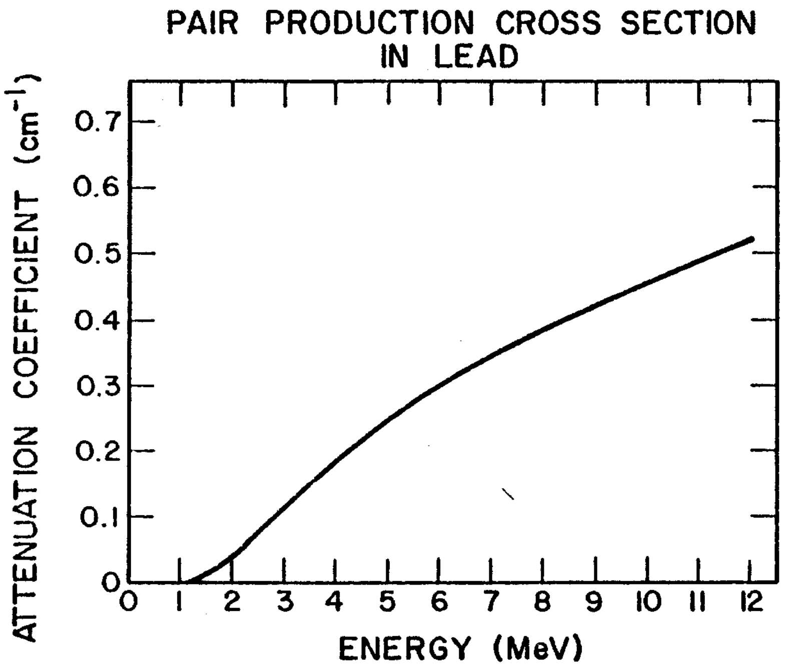

Figure 7
(Ref. 16)

However, the energy lost by the photon is not the local energy deposition since both the electron and positron have finite ranges in solid materials.

IV.1.2 Incoherent Scattering

At intermediate energies the principle photon interaction can be incoherent (or Compton) scattering. In this process energy is given by an incident photon to an electron and results in a scattered photon. The incoherent scattering cross section can be derived using quantum electrodynamics and is given by the Klein-Nishina formula for unpolarized incident radiation as:[16]

$$3)\quad \frac{d\sigma}{d\Omega} = \frac{r_o^2}{2} \quad [1+X(1-\cos\Theta)]^{-3} \; [1+\cos^2\Theta + \frac{X^2(1-\cos\Theta)^2}{1+X(1-\cos\Theta)}]$$

units = cm^2/electron

$\frac{d\sigma}{d\Omega}$ = differential cross section, (cm^2/electron)

where $X = E/m_oc^2$

r_o = classical electron radius = 2.818×10^{-13} cm

Θ = scattering angle

E = photon incident energy

This is the cross section for one electron and since Compton scattering implies incoherent field superposition, each electron adds independently. Thus for a given material the above formula is multiplied by Z to get the differential cross section per atom. Equation 3 can be integrated to give the total cross section as in Evans(16) in a form which is difficult to evaluate numerically. However, Biggs[18] gives a useful approximation as:

$$4)\quad \sigma_{tot}^{kn} = 0.4006 \ \frac{Z}{A}\left[\frac{1+1.148+0.6141X^2}{1+3.171X+0.9328X^2+0.02572X^3}\right] \left(\frac{cm^2}{gm}\right)$$

Both Equation 3 and 4 are for free electrons and must be corrected for electron binding effects. These corrections are made in reference 17 and will not be repeated here since the effect is most important for low photon energies where the incoherent cross section is a small contribution to the total cross section.

The portion of the incident photon energy which is deposited as kinetic energy of the electrons can be expressed in terms of an energy absorption cross section. The energy absorption cross section may be derived from Equation 3 by multiplying by the energy fraction given to the electron and integrating over all angles. Again the exact analytical expression is not convenient for numerical approximation and Biggs[18] proposes the following approximation:

$$5)\ \sigma_a^{kn} = 0.4006\ \frac{Z}{A}\left[\frac{X+0.825X^2+0.0323X^3}{1+5.393X+5.212X^2+0.878X^3+0.01599X^4}\right]$$

units = cm^2/gm

As before,an alternate energy absorption cross section can be derived which accounts for electron binding. Commensurate approximation of these results are also available for efficient numerical evaluation.

IV.1.3 Coherent Scattering

As the energy of the incident photon is reduced to low enough frequencies where the momentum can be ignored, Equation 3 approaches the classical formula for Thompson scattering for isolated electrons as:[19]

$$6)\qquad \frac{d\sigma}{d\Omega} = \frac{r_o^{\ 2}}{a}\ (1+\cos^2\Theta)$$

If Equation 6 is integrated over all directions, the total Thompson scattering cross section is obtained:

$$7)\qquad \sigma_c = \frac{8\pi}{3}\ r_o^{\ 2}\ = .665\ \text{barns/electron}$$

If Equation 6 is to be applied to a population of electrons it is necessary to account for the coherent effect of all the particles. This approach gives an intensity proportional to Z^2 and is limited to small scattering angles whose magnitudes are inversely proportional to the incident photon energies. Consequently, when this angular distribution and the effects of electron binding are accounted for, the total coherent cross section falls off with increasing energy.

Since coherent scattering is elastic, it does not result in any net loss of photon energy, and there is no significant local deposition of energy.

IV.1.4 Photoelectric Effect

At low photon energies the total photon cross section is dominated by the photoelectric cross section in which a photon transfers all its energy to an electron in the vicinity of a nucleus. The electron is emitted (Auger electron) with the photon energy minus its binding energy.

A universal theoretical treatment does not exist for the photoelectric effect, consequently empirical data are used in determining cross section values. A convenient form for fitting photoelectric cross sections has been proposed by Biggs and Lighthill as:[14]

8) $$\sigma_j = \sum_{k=1}^{4} C_{jk}\, e^{-k} \qquad \text{cm}^2/\text{gm}$$

where a set of four parameters, C_{jk}, are used for fitting the data within discrete energy intervals characterized by the parameter j. It is necessary to break the spectrum into different intervals in order to properly account for absorption edges.

The local energy absorption is usually determined by discounting the energy associated with the K shell fluorescence. This is essentially the same as deducting the binding energy from the photon energy and it reduces the total photoelectric cross section somewhat.

In general the photoelectric cross section shows a very strong material and spectral dependence. Useful approximations for these dependencies are given by Evans[16] for energies away from absorption edges as:

$$\sigma_{pe} \propto (Z/E)^{3 \text{ to } 4} \tag{9}$$

IV.1.5 Low Energy Photon Attenuation

Electromagnetic radiation in the near visible range (e.g., from reflected laser light) cannot be adequately described by the cross sections previously presented. Hovingh[20] has proposed a simple relation based on the propagation of electromagnetic radiation in homogeneous, isotropic, conducting media. This relation can be developed from basic electrodynamics[21] in the following manner:

The combination of Maxwell's equations and the relation of current density to the electric field in a conducting material,

10) $$J = \sigma E$$

yields the following relation for the electric vector:

11) $$\nabla^2 E = \frac{4\pi\sigma\mu}{c^2}\frac{\partial E}{\partial t} + \frac{\mu}{c}\frac{\partial^2 \xi E}{\partial t^2}$$

where J = current density
σ = specific conductivity
E = electric vector
c = velocity of light
μ = magnetic permeability
ξ = dielectric constant

Taking a Fourier transform in time and space gives the complex wave number as:

12) $$k^2 = \frac{\omega^2 \xi\mu}{c^2} \left(1 + i\,\frac{4\pi\sigma}{\omega\xi}\right)$$

Since the electric vector goes as $e^{i(kx-\omega t)}$ and the energy goes as E^2, the imaginary part of the wave number, multiplied by 2, gives the energy attenuation. Thus

13) $$k'' = \left[\frac{\sqrt{1 + \left(\frac{4\pi\sigma}{\omega\xi}\right)^2} - 1}{2} \right]^{1/2} \sqrt{\xi\mu}\ \frac{\omega}{c}$$

for a conductor $\frac{4\pi\sigma}{\omega\xi} >> 1$ and

14) $$\Sigma = 2k'' = \sqrt{\frac{8\pi\mu\omega\sigma}{c^2}} = 4\pi\sqrt{\frac{\mu\sigma}{\lambda c}}$$

where Σ = attenuation coefficient

ω = frequency

λ = wavelength

k = wave number, k'' = imaginary part

The absorbed energy can be determined by determining the reflectivity at the surface

15) $$R = \left| \frac{n-1}{n+1} \right|^2$$ n = complex refractive index

which for metals becomes

16) $$R = 1 - 2\sqrt{\frac{c}{\sigma\lambda}}$$

The absorptivity is then

17) $$\alpha = 1 - R = 2\sqrt{c/\sigma\lambda}$$

If the assumption is made that the surface is a black body $\alpha = 1$ and by multiplying Equation 14 by Equation 17, the attenuation coefficient can be found as

18) $$\Sigma = 8\pi/\lambda \qquad \text{cm}^{-1}$$

This development is based on principles which are derived for low frequency radiation and do not take into account the numerous phenomena which should be considered for photons with approximately 1 eV energy. Values from this relation are nevertheless plotted with the other cross sections in Figure 8 for comparison. Further investigation is necessary to obtain realistic values for laser irradiation. It is likely that only empirically determined values will be available.

IV.1.6 Comparison of Cross Sections

A comprehensive tabulation of parameters to be used in the previous equations have been made by Biggs.[14] These values have been examined for accuracy by comparing with other cross section files such as ENDF/B and by Simmons and Hubbell[22,23]. An example of the cross section from reference 14 for energies from 10 eV through 1 MeV is shown in Figure 8.

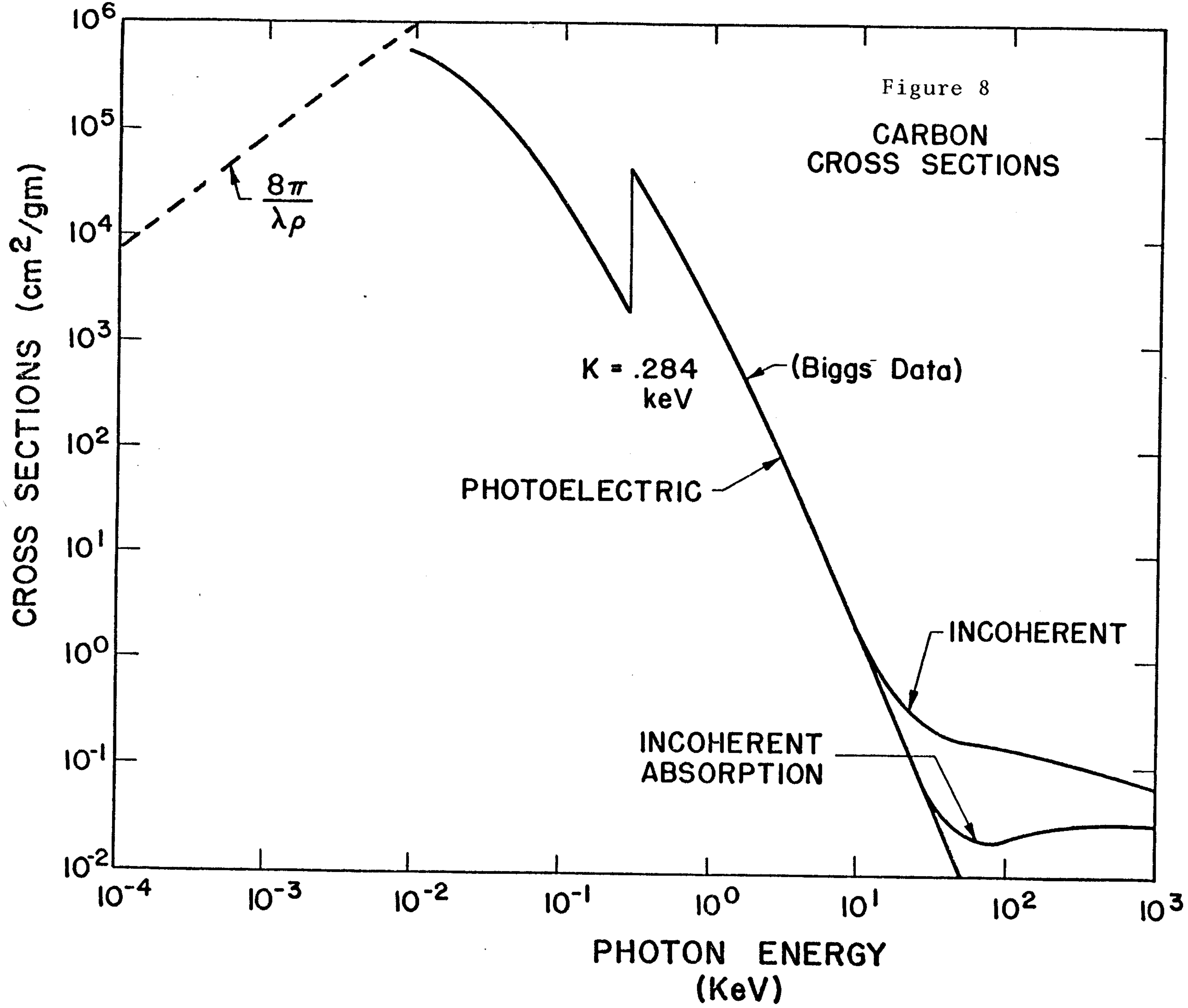

Figure 8

CARBON
CROSS SECTIONS
$\frac{8\pi}{\lambda\rho}$
K = .284
keV
(Biggs' Data)
PHOTOELECTRIC
INCOHERENT
INCOHERENT
ABSORPTION
CROSS SECTIONS (cm^2/gm)
10^6
10^5
10^4
10^3
10^2
10^1
10^0
10^{-1}
10^{-2}
10^{-4}
10^{-3}
10^{-2}
10^{-1}
10^0
10^1
10^2
10^3
PHOTON ENERGY
(KeV)

A significant increase (factor of 10) of the photoelectric cross section is noted at the K shell resonance (284 eV for carbon). This effect will result in a marked spectral sensitivity for first wall response and will be important for all materials. Figure 9, from data taken from reference 24, shows how the absorption edges vary with atomic number.

Determination of the energy deposited from a given spectrum must account also for transport of any scattered photons. Computational techniques are available to perform these calculations using the appropriate cross sections. These include ANISN[25] and BUCKL[26] in one dimension. If, however, the primary interaction is the photoelectric effect, the scattering can be ignored and an exponential deposition profile can be assumed. A reasonable criterion for determining if a spectrum is in the photoelectric region can be found from examination of Figure 10 which displays the ratio of the photoelectric cross section to the total cross section. As shown, the photoelectric effect comprises 90% of the interactions for photon energies up to 10 kev, 30 keV, 70 keV for carbon, iron, and molybdenum respectively.

A summary of the qualitative material and spectral dependence of the basic attenuation mechanisms is given in Table 3.

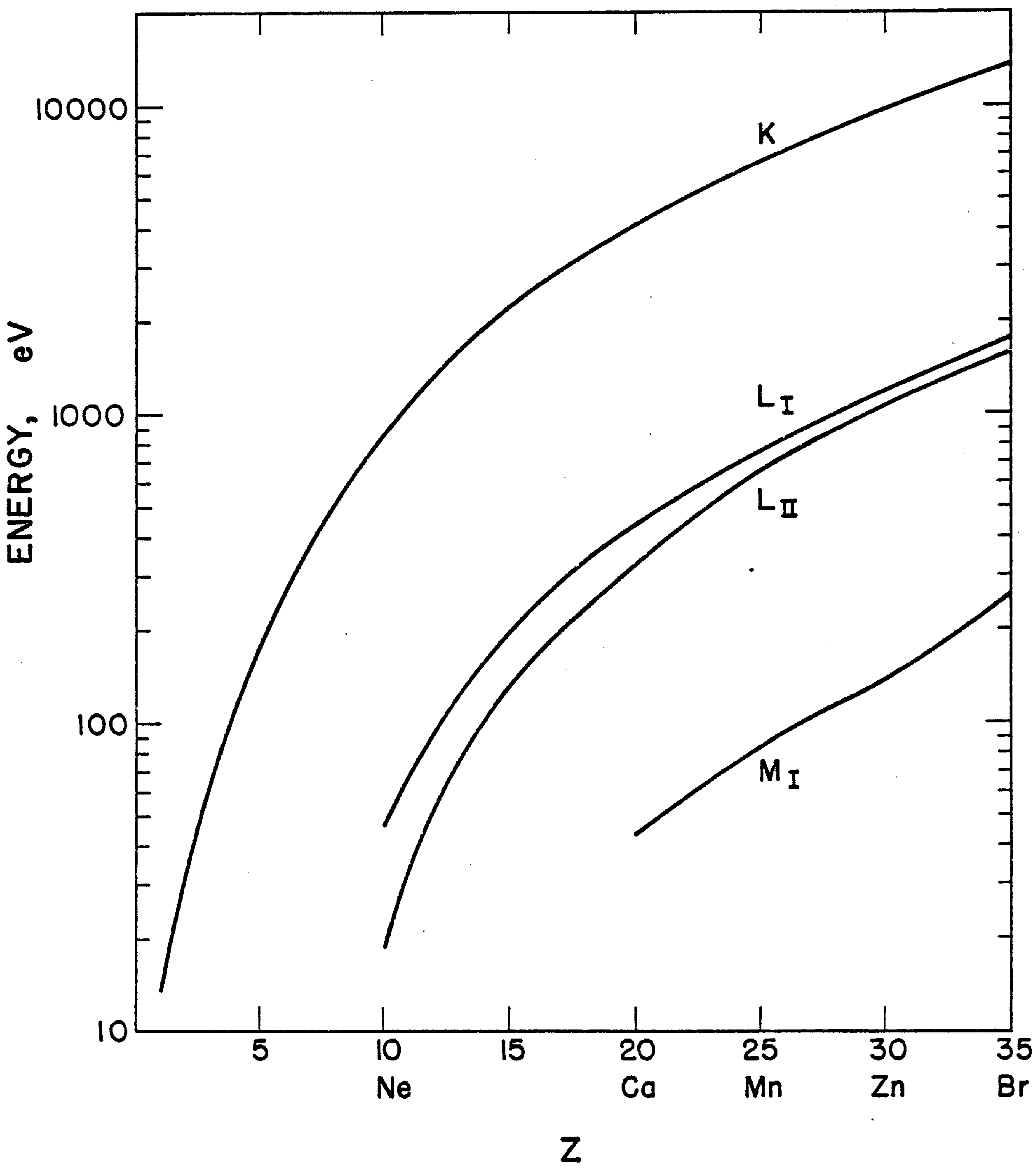
X-RAY ATOMIC ENERGY LEVELS
ENERGY, eV
10000
1000
100
10
K
L_I
L_{II}
M_I
5
10
Ne
15
20
Ca
25
Mn
30
Zn
35
Br
Z

Figure 9

TABLE 3

MATERIAL AND SPECTRAL DEPENDENCE OF PHOTON CROSS SECTION

	Photo-Electric	Coherent	Incoherent	Pair Production
Atomic Number	$Z^{3\text{ to }4}$	Z^2	Z	Z^2
Energy	$(1/E)^{3\text{ to }4}$	$(1/E)^{1\text{ to }2*}$	NSR	E

*E > 10 keV NSR = no simple relationship

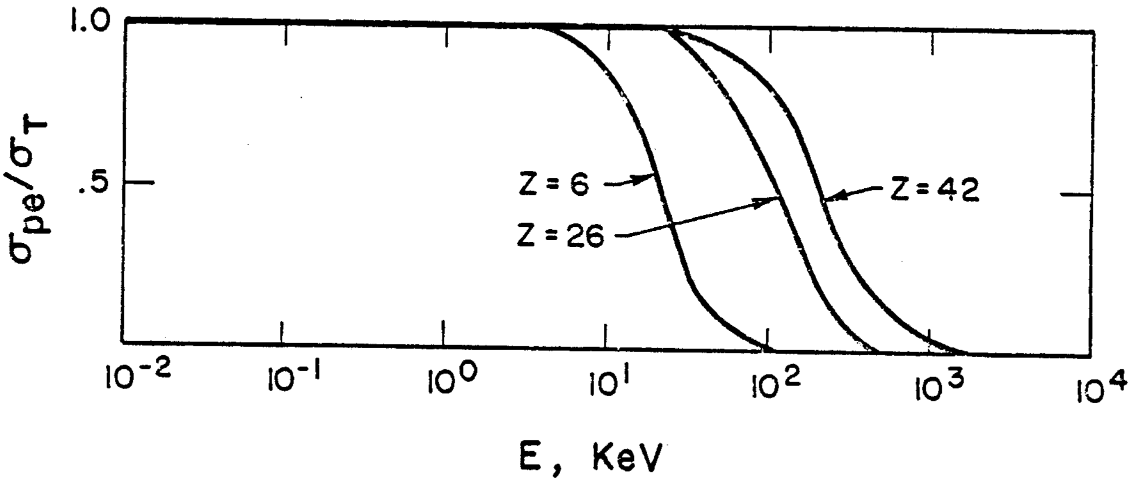

Fig. 10. Ratio of Photoelectric to Total Cross Section

IV.2 Ion Interaction

The slowing down of ions in materials is primarily due to two processes: the interaction of the electric fields of the ion with the electrons in the material (inelastic) and the collision of the ion with nuclei (elastic). The relative importance of these two phenomena is dependent upon the instantaneous energy of the ion and the energy loss associated with each can be determined if appropriate interaction potentials can be specified. For particles other than electrons, any radiation losses such as bremsstrahlung or Cerenkov can be neglected if the energies do not exceed 10 MeV.

IV.2.1 Electronic Energy Loss

The interaction of a charged particle with the electrons in a material is usually divided into three energy regimes: (i) a high energy regime in which the velocity of the particle greatly exceeds the velocities of the orbital electrons, (ii) an intermediate energy regime in which these velocities are on the same order, and (iii) a low energy regime in which the velocity of the particle is much smaller than the orbital velocities of the electrons.

The first region was investigated years ago by Bohr,[16] Bethe,[27] Bloch[27] and Fermi.[19] The most commonly accepted formula is that by Bethe-Bloch which is a quantum mechanical derivation of the original classical result by Bohr. The Bethe-Bloch formula for non-relativistic velocities is given as:

19) $$-\left.\frac{dE}{dx}\right)_e = \frac{4\pi Z_1^2 e^4 \; NZ_o}{m_o \; v^2} \quad \ln \frac{2m_o v^2}{I}$$

where Z_1 = particle charge
e = electron charge
N = atom density
Z_o = material atomic number
m_o = electron mass
v = particle velocity
I = mean ionization potential

The parameter I is a representation of the lower limit over which energy can be transferred in a coulomb collision and is given approximately by[16]

20) $$I = 12\ Z \quad (\text{eV})$$

In practice, I becomes an empirically adjusted factor for each target material. Numerous modifications have been proposed to Equation 19 but in general its energy dependence is reasonably accurate.

The most general treatment of fast particles in matter is given by the Fermi formula[15] which accounts for the modification of the electric field of the particle by the dielectric characteristics of the material. This formula will not be repeated here since it is most applicable at very high energies ($E > 5Mc^2$, where M is the particle mass). Implicit in all the above models is total stripping of all electrons from the incident ion.

At low energies the particles tend to retain all their electrons and can be modeled by treatments developed by Lindhard[28] (LSS) and Firsov.[29] In these models the energy loss is attributed to the electron flux between colliding atoms and is consequently proportional to the particle velocity. The Lindhard model for electronic losses is normally presented in non-dimensional form as:

21) $$\frac{d\varepsilon}{d\rho} = k\, \varepsilon^{\frac{1}{2}}$$

where $\varepsilon = E/E_L$

$\rho = r/R_L$

$$k = \frac{0.0793\, Z_1^{2/3}\, Z_2^{1/2}\, (1+A)^{3/2}}{(Z_1^{2/3} + Z_2^{2/3})^{3/4}\, M_2^{1/2}}$$

where Z_1e = particle charge

Z_2e = target charge

A = ratio of target mass to particle mass

M_2 = target mass (amu)

and

$$E_L = \left[\frac{1+A}{A}\right] \frac{Z_1 Z_2 e^2}{a} \qquad \text{(ergs)}$$

$$R_L = \frac{(1+A)^2}{4A\pi N a^2} \qquad \text{(cm)}$$

$$a = 0.4683\ (Z_1^{2/3} + Z_2^{2/3})^{-1/2} \times 10^{-8} \qquad \text{(cm)}$$

N = target atom density (a/cm^3)

In a more practical form

22) $$\frac{dE}{dX} = C\ E^{\frac{1}{2}}$$

where $$C = \frac{k\ (E_L/1.602 \times 10^{-9})^{\frac{1}{2}}}{R_L \times 10^4} \qquad (\text{keV}^{\frac{1}{2}}/\mu\text{m})$$

Equations 21 or 22 are normally considered applicable for particle velocities below the orbital velocity of the target electrons. Assuming a Thomas-Fermi atomic model this maximum energy becomes:

23) $$E_{MAX} = 25\ M_1\ Z_1^{4/3} \quad \text{(keV)}$$

where M_1 = particle mass (amu)

A tabulation of E_L, R_L, k, C, and E_{MAX} is given in Table 4 for deuterons, tritons, alpha particles and self ions interacting with most common metallic elements.

The intermediate energy regime between the upper limit of LSS theory and the Bethe-Bloch theory has no basic theoretical treatment at present. This region is characterized by a partially ionized particle. As a result, modifications to the effect charge and the interaction with outer shell electrons are sometimes incorporated into the Bethe-Bloch model which in its standard form (Eqn. 19) predicts a greater stopping power than observed experimentally.

A comprehensive semiphenomenological model has been proposed by Brice[30] which can predict the electronic stopping for all three energy regimes. This model is based on a modification of the Firsov method by giving a quantum mechanical treatment of the electron flux between adjacent interacting particles in terms of bound state wave functions. When this formalism is used with a hydrogenic 1s wave function, a general relationship is determined which depends on only three adjustable parameters which can be determined from experiments. One parameter is necessary for the low

TABLE 4(a)

LINDHARD PARAMETERS
DEUTERIUM
(E_{MAX} = 50 keV)

Target	Z2	M2 (amu)	ρ (gm/cm^3)	E_L (keV)	R_L (μm)	K	C (keV$^{1/2}$/μm)
BE	4	9.0	1.8	.282	.007	.263	20.20
B	5	10.8	2.3	.361	.008	.311	22.64
C	6	12.0	2.2	.447	.011	.345	20.57
MG	12	24.3	1.7	.998	.074	.667	8.95
AL	13	26.9	2.6	1.09	.061	.736	12.67
SI	14	28.0	2.3	1.20	.079	.767	10.63
TI	22	47.9	4.5	2.09	.145	1.29	12.87
V	23	50.9	6.1	2.21	.125	1.37	16.37
CR	24	51.9	7.1	2.34	.113	1.40	18.97
MN	25	54.9	7.4	2.46	.125	1.48	18.63
FE	26	55.8	7.8	2.59	.124	1.50	19.50
CO	27	59.9	8.9	2.70	.129	1.61	20.62
NI	28	58.7	8.9	2.84	.127	1.58	21.13
CU	29	63.5	8.9	2.97	.150	1.71	19.71
ZN	30	65.3	7.1	3.10	.203	1.76	15.30
GA	31	69.7	5.9	3.23	.283	1.87	11.92
GE	32	72.5	5.3	3.36	.347	1.95	10.34
ZR	40	91.2	6.5	4.47	.506	2.45	10.29
NB	41	92.9	8.5	4.62	.405	2.50	13.29
MO	42	95.9	10.2	4.76	.367	2.58	15.37
AG	47	107.8	10.5	5.51	.482	2.91	14.16
CD	48	112.4	8.6	5.66	.643	3.03	11.21
IN	49	114.8	7.3	5.81	.804	3.09	9.29
SN	50	118.6	7.3	5.96	.869	3.20	9.00
SB	51	121.7	6.6	6.12	1.0	3.25	8.04
HF	72	178.4	13.2	9.58	1.3	4.82	11.13
TA	73	180.9	16.6	9.75	1.1	4.89	13.72
W	74	183.8	19.3	9.92	.9	4.97	15.71
RE	75	186.2	21.0	10.1	.9	5.03	16.91
PT	78	195.0	21.4	10.6	1.0	5.28	16.50
AU	79	196.9	19.3	10.8	1.1	5.33	14.73
HG	80	200.5	13.5	10.9	1.7	5.43	10.15
PB	82	207.1	11.3	11.3	2.2	5.61	8.24
BI	83	208.9	9.7	11.5	2.7	5.66	7.02
U	92	238.0	18.9	13.1	1.9	6.45	12.05

TABLE 4(b)

LINDHARD PARAMETERS
TRITIUM
(E_{MAX} = 75 keV)

Target	Z2	M2 (amu)	ρ (g/cm^3)	E_L (keV)	R_L (μm)	K	C (keV$^{1/2}$/μm)
BE	4	9.0	1.8	.308	.006	.164	16.50
B	5	10.8	2.3	.390	.006	.190	18.50
C	6	12.0	2.2	.479	.009	.209	16.81
MG	12	24.3	1.7	1.0	.054	.385	7.31
AL	13	26.9	2.6	1.1	.043	.423	10.36
SI	14	28.0	2.3	1.2	.056	.440	8.68
TI	22	47.9	4.5	2.1	.101	.726	10.52
V	23	50.9	6.1	2.2	.086	.770	13.38
CR	24	51.9	7.1	2.3	.078	.787	15.50
MN	25	54.9	7.4	2.5	.086	.829	15.22
FE	26	55.8	7.8	2.6	.086	.844	15.93
CO	27	59.9	8.9	2.7	.089	.903	16.85
NI	28	58.7	8.9	2.8	.087	.887	17.26
CU	29	63.5	8.9	3.0	.103	.956	16.11
ZN	30	65.3	7.1	3.1	.140	.984	12.50
GA	31	69.7	5.9	3.2	.194	1.04	9.76
GE	32	72.5	5.3	3.4	.238	1.08	8.45
ZR	40	91.2	4.5	4.5	.345	1.36	8.41
NB	41	92.9	8.5	4.6	.276	1.38	10.86
MO	42	95.9	10.2	4.8	.250	1.43	12.56
AG	47	107.8	10.5	5.5	.328	1.61	11.57
CD	48	112.4	8.6	5.7	.437	1.67	9.16
IN	49	114.8	7.3	5.8	.546	1.71	7.59
SN	50	118.6	7.3	6.0	.590	1.76	7.35
SB	51	121.7	6.6	6.1	.686	1.81	6.57
HF	72	178.4	13.2	9.6	.907	2.65	9.09
TA	73	180.9	16.6	9.8	.752	2.69	11.21
W	74	183.8	19.3	9.9	.673	2.73	12.84
RE	75	186.2	21.0	10.1	.639	2.77	13.82
PT	78	195.0	21.4	10.6	.704	2.90	13.49
AU	79	196.9	19.3	10.8	.803	2.93	12.04
HG	80	200.5	13.5	11.0	1.1	2.98	8.29
PB	82	207.1	11.3	11.4	1.5	3.08	6.73
BI	83	208.9	9.7	11.5	1.8	3.11	5.74
U	92	238.0	18.9	13.2	1.3	3.54	9.84

TABLE 4(c)

LINDHARD PARAMETERS
He^4
(E_{MAX} = 250 keV)

Target	Z2	M2 (amu)	ρ (g/cm^3)	E_L (keV)	R_L (μm)	K	C ($keV^{1/2}/\mu m$)
BE	4	9.0	1.8	.720	.006	.170	25.52
B	5	10.8	2.3	.895	.006	.197	29.25
C	6	12.0	2.2	1.0	.008	.217	27.04
MG	12	24.3	1.7	2.2	.047	.394	12.45
AL	13	26.9	2.6	2.4	.038	.432	17.74
SI	14	28.0	2.3	2.6	.049	.450	14.95
TI	22	47.9	4.5	4.5	.084	.740	18.62
V	23	50.9	6.1	4.7	.072	.784	23.74
CR	24	51.9	7.1	5.0	.065	.801	27.56
MN	25	54.9	7.4	5.2	.071	.845	27.13
FE	26	55.8	7.8	5.5	.071	.860	28.45
CO	27	59.9	8.9	5.7	.073	.919	30.14
NI	28	58.7	8.9	6.0	.072	.904	30.94
CU	29	63.5	8.9	6.2	.085	.974	28.92
ZN	30	65.3	7.1	6.5	.114	1.00	22.48
GA	31	69.7	5.9	6.8	.159	1.06	17.54
GE	32	72.5	5.3	7.0	.194	1.10	15.25
ZR	40	91.2	6.5	9.3	.278	1.39	15.31
NB	41	92.9	8.5	9.6	.222	1.41	19.79
MO	42	95.9	10.2	9.9	.201	1.46	22.92
AG	47	107.8	10.5	11.4	.262	1.64	21.21
CD	48	112.4	8.6	11.7	.349	1.71	16.81
IN	49	114.8	7.3	12.0	.435	1.74	13.93
SN	50	118.6	7.3	12.3	.470	1.80	13.51
SB	51	121.7	6.6	12.6	.546	1.85	12.08
HF	72	178.4	13.2	19.6	.713	2.71	16.90
TA	73	180.9	16.6	20.0	.591	2.75	20.85
W	74	183.8	19.3	20.3	.529	2.79	23.88
RE	75	186.2	21.0	20.7	.502	2.83	25.71
PT	78	195.0	21.4	21.8	.552	2.97	25.12
AU	79	196.9	19.3	22.1	.629	2.99	22.43
HG	80	200.5	13.5	22.5	.937	3.05	15.46
PB	82	207.1	11.3	23.2	1.2	3.15	12.56
BI	83	208.9	9.7	23.6	1.4	3.18	10.71
U	92	238.0	18.9	26.9	1.0	3.62	18.42

TABLE 4 (d)

LINDHARD PARAMETERS
SELF ION

Target	Z2	M2 (amu)	ρ (g/cm^3)	E_L (keV)	R_L (μm)	K	C (keV$^{1/2}$/μm)	E_{MAX} (MeV)
BE	4	9.0	1.8	2.2	.006	.112	28.09	1.43
B	5	10.8	2.3	3.7	.007	.119	35.12	2.31
C	6	12.0	2.2	5.6	.008	.127	35.83	3.27
MG	12	24.3	1.7	28.6	.035	.142	21.49	16.7
AL	13	26.9	2.6	34.5	.027	.142	31.32	20.6
SI	14	28.0	2.3	41.0	.034	.146	27.76	23.7
TI	22	47.9	4.5	117.9	.040	.151	41.15	73.8
V	23	50.9	6.1	130.8	.032	.151	53.19	83.3
CR	24	51.9	7.1	144.5	.029	.154	63.78	90.0
MN	25	54.9	7.4	158.9	.030	.154	63.65	100.
FE	26	55.8	7.8	174.1	.030	.157	68.89	108.
CO	27	59.9	8.9	190.2	.029	.155	73.20	121.
NI	28	58.7	8.9	207.0	.029	.160	78.79	125.
CU	29	63.5	8.9	224.7	.032	.158	73.37	142.
ZN	30	65.3	7.1	243.2	.043	.159	58.22	152.
GA	31	69.7	5.9	262.5	.056	.158	45.49	170.
GE	32	72.5	5.3	282.7	.066	.158	40.04	184.
ZR	40	91.2	6.5	475.9	.079	.163	45.24	312.
NB	41	92.9	8.5	504.1	.062	.165	59.45	328.
MO	42	95.9	10.2	533.2	.055	.165	69.49	350.
AG	47	107.8	10.5	693.3	.064	.167	68.28	457.
CD	48	112.4	8.6	728.2	.083	.166	54.20	490.
IN	49	114.8	7.3	764.1	.101	.167	45.44	515.
SN	50	118.6	7.3	801.0	.106	.166	44.27	547.
SB	51	121.7	6.6	838.9	.121	.166	39.91	576.
HF	72	178.4	13.2	1875.6	.112	.173	66.79	1340.
TA	73	180.9	16.6	1937.0	.092	.173	83.05	1380.
W	74	183.8	19.3	1999.5	.081	.173	95.79	1430.
RE	75	186.2	21.0	2063.1	.076	.174	103.98	1470.
PT	78	195.0	21.4	2260.8	.080	.174	103.57	1630.
AU	79	196.9	19.3	2329.0	.090	.175	93.33	1670.
HG	80	200.5	13.5	2398.4	.133	.175	64.61	1730.
PB	82	207.1	11.3	2540.6	.166	.175	53.08	1850.
BI	83	208.9	9.7	2613.5	.197	.176	45.64	1890.
U	92	238.0	18.9	3323.1	.123	.176	82.31	2470.

energy regime and the other two are used for extension to higher energies.

The result of this model is given[31] by the following formulae:

24) $$S(E) = N\,(Z_1+Z_2)\,S_e(u)\,f(u) \qquad (\mathrm{eV/cm})$$

where $S(E)$ = electronic stopping power
E = particle energy (keV)
Z_1 = particle atomic number
Z_2 = target atomic number
N = target atomic density (a/cm^3)

and

25) $$S_e(u) = A\left(u^{\frac{1}{2}}\left[\frac{30u^2+53u+21}{3(1+u)^2}\right] + (10u+1)\,\mathrm{arc\,tan}\,(u^{\frac{1}{2}})\right)$$

$A = 0.60961 \times 10^{-15}$ eV-cm^2/atom
$u = E/(\zeta^2\,M_1E_1)$

where M_1 = particle mass (amu)
E_1 = 100 keV
*ζ = adjustable parameter

and

26) $$f(u) = [\,1 + (4\,\zeta^2\,a'^2\,u)^{n/2}\,]^{-1}$$

* a' = adjustable parameter

* n = adjustable parameter

The three adjustable parameters can be determined from sources of reliable experimental data or semi-empirical values determined from data in each of the three energy regimes. A tabulation of a significant number of calculations for various ions and targets has been compiled in reference 31. In this case parameters were determined from Ziegler and Chu[32] for the ions and the tabulated stopping powers of Northcliffe and Schilling.[33] The former represents a tabulation of a least squares fit to a large number of published experimental results and an interpolation to other materials by correlating with theoretical models for the Z dependence of stopping power. The latter is based on determining relative stopping cross sections for other materials and comparing with a set of particular known cross sections (aluminum in this case).

An example of electronic energy loss from the previously discussed models is shown in Figure 11. The LSS model is seen to predict large stopping powers (about 45% high) in the low energy region. The Bethe-Bloch model (BB) is normalized to the experimental points by adjusting I to 20 ev and shows a gross divergence at low energies. The Brice model, however, gives a reasonable fit over the entire spectrum.

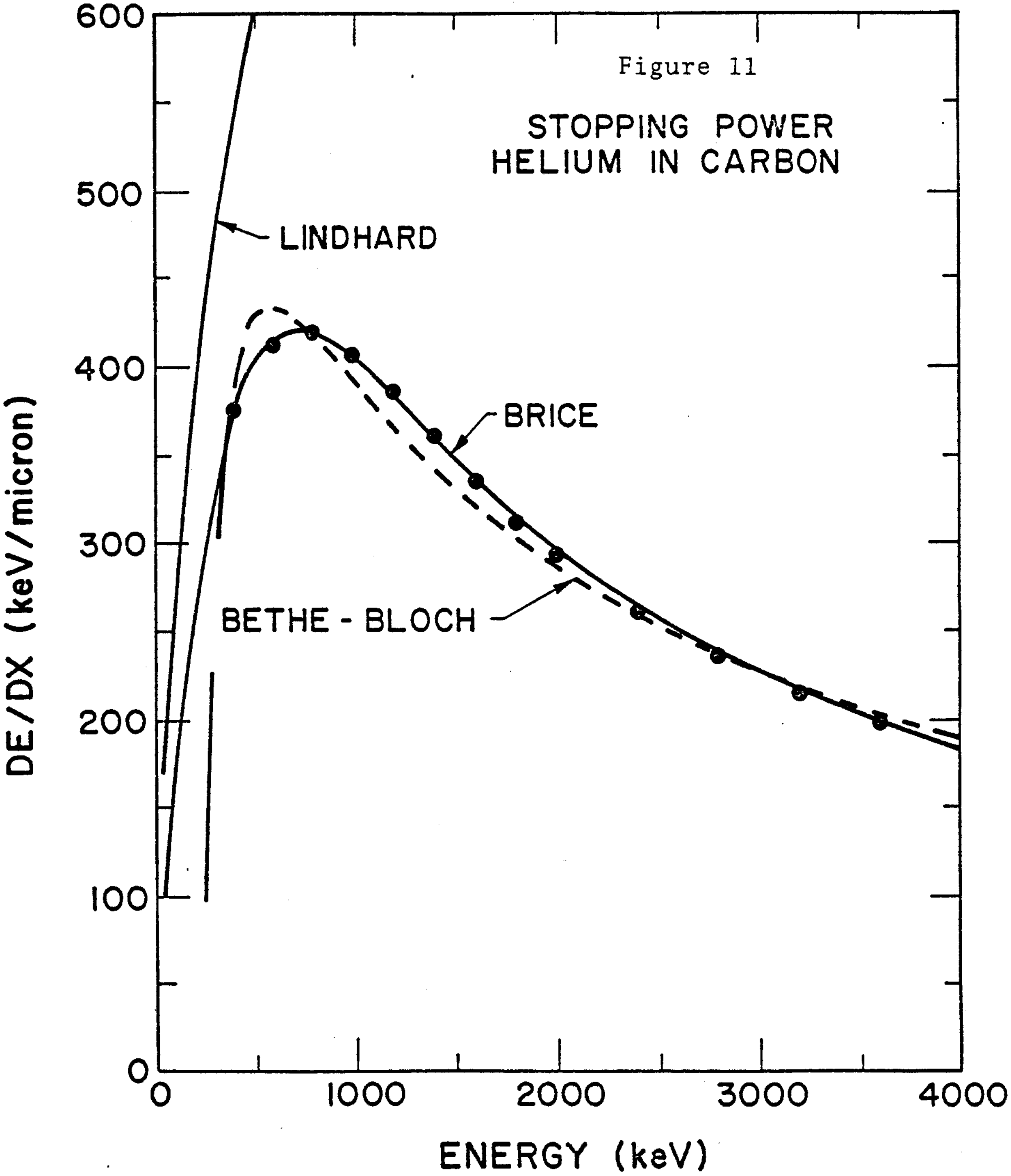

Figure 11

STOPPING POWER
HELIUM IN CARBON
LINDHARD
BRICE
BETHE - BLOCH
DE/DX (keV/micron)
ENERGY (keV)
0
100
200
300
400
500
600
0
1000
2000
3000
4000

IV.2.2 Nuclear Energy Loss

Elastic collisions of a moving particle with the nuclei will be a competing process for reducing the kinetic energy of the particle. The rate of interaction will be determined by the nuclear cross section. Theoretical values for nuclear cross sections are determined by the interatomic potential chosen between the nuclei and the particle.

The most widely accepted model is the nuclear elastic cross section derived by Lindhard[28] in which a relatively simple analytic expression is derived using a shielded Coulomb interaction with a Thomas-Fermi atomic model. The differential cross section is given by:[31]

27) $$d\sigma(E,T) = \pi a^2 f(t)\, dt/t^2$$

where E = particle energy

T = kinetic energy of the struck atom after the collision

a = screening parameter given by:

$$.8853\, a_o/(Z_1^{2/3} + Z_2^{2/3})^{1/2}$$

a_o = Bohr radius

$f(t)$ = is a tabulated scattering function (ref. 31)

$t = E/E_o \sqrt{T/T_m}$

and $E_o = Z_1Z_2e^2 \ (m + m_2)/am_2$

T_m = maximum energy transferable = $\dfrac{4\ m_1m_2E}{(m_1+m_2)^2}$

The total elastic cross section is obtained by integrating Equation 27 over all possible energy transfers. The average energy lost per collision can also be obtained and an expression derived for the energy loss per unit path length. An approximation put in the same non-dimensional form as the electron loss is given by Oen and Robinson[34] as:

$$28) \quad \left(\frac{d\varepsilon}{d\rho}\right)_n = \frac{9}{8\varepsilon}\{\ln[u + (1+u^2)^{1/2}] - u\ (1+u^2)^{-1/2}\}$$

where $\varepsilon = E/E_L$, $\rho = X/X_L$ as before

$u = (2\lambda)^{1/3} \ \varepsilon^{4/9}$

$\lambda = 1.309$

A qualitative measure of the relative roles of electronic loss versus elastic or nuclear loss can be seen in Figure 12 which is taken from data in reference 31 for helium into a carbon target. Obviously the nuclear energy loss is very low over the range of energies listed and, as a general rule, the electronic loss will dominate down to "A" keV where A is the particle mass in amu. Thus for high energy particles the nuclear energy deposition is negligible since a 400 keV alpha particle would dissipate 80% of its energy before the nuclear contribution was .1% of the electronic.

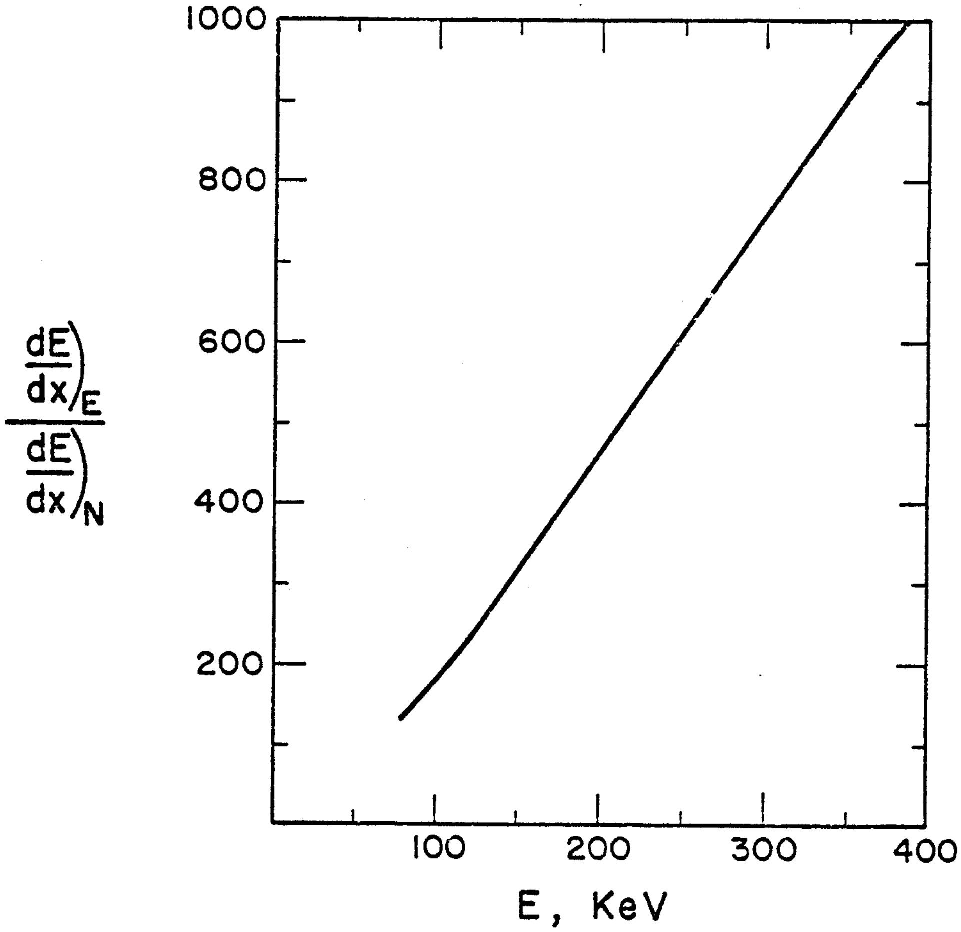

Fig. 12. A comparison of electron and nuclear energy loss for helium in carbon. (Data from Reference 31)

IV.3 Neutron Interactions

The primary interaction rates in first walls to the current of neutrons from a pulsed fusion source will be determined by the corresponding neutron cross sections of the material. Each possible reaction will deposit some local energy and produce products such as neutrons, charged particles, or photons. A discussion of the theory of all possible cross sections would be inappropriate here, but a brief discussion of the amplitudes of the reaction rates will be informative.

The local heating due to neutrons can be determined from the neutron flux and knowledge of an energy dependent Kerma* factor. Recent work by Abdou, et al.,[35] have determined such Kerma factors for most potential fusion materials. These have been used to establish heating rates in magnetic confinement fusion reactors.[36] An example of this work for low Z elements is shown in Figure 13. Carbon is typical of a nuclide in which the elastic scattering is the primary interaction up through the MeV region making the Kerma factor almost proportional to the energy. A rough estimate of the volumetric heating rate from source neutrons can be made by simply multiplying the

---

*KERMA = Kinetic Energy Released in Materials.

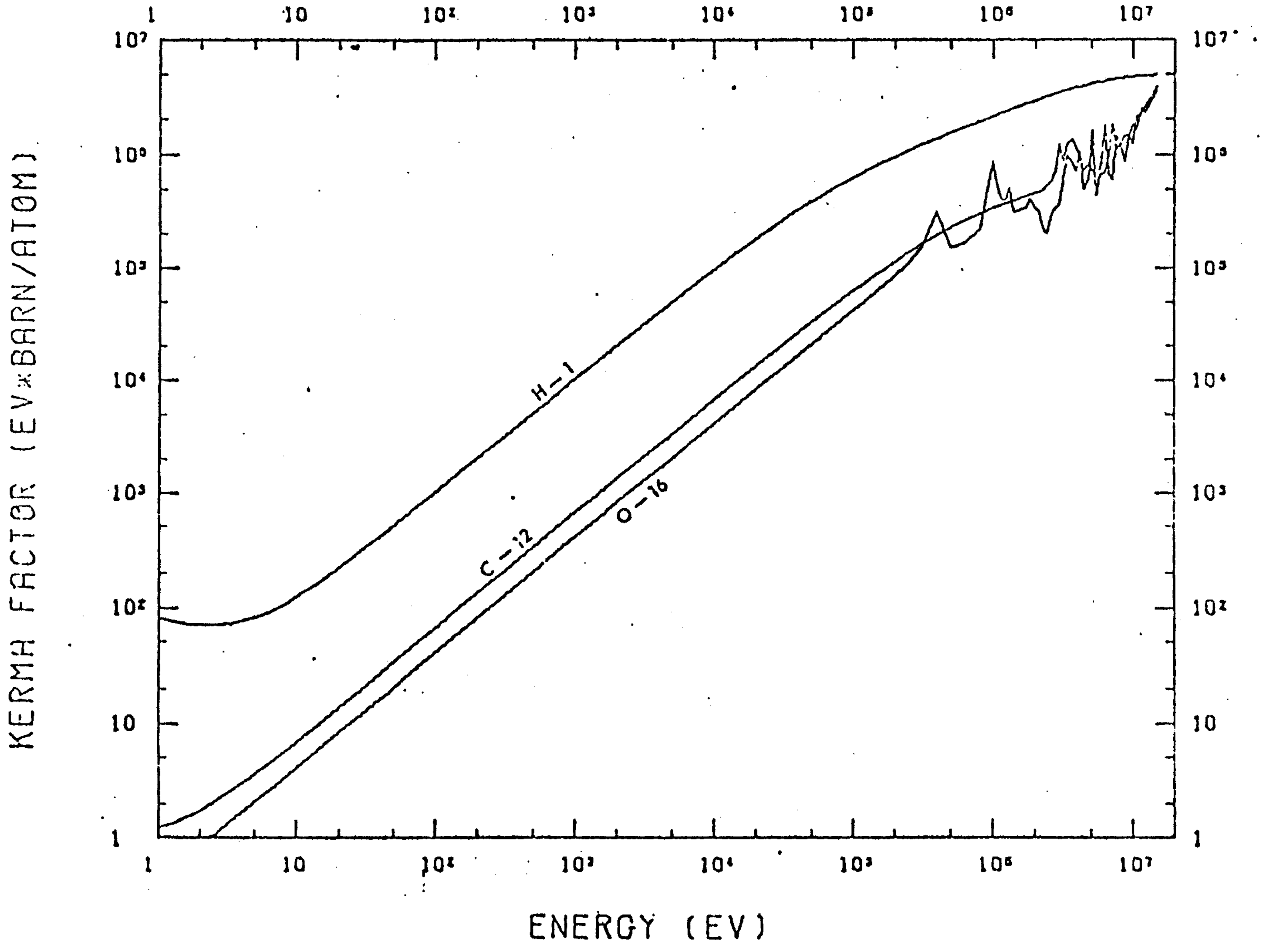

Fig. 13. Neutron Kerma Factors (Ref. 36) .

14 MeV Kerma factor by the integrated neutron wall current for a laser fusion pulse (Table 1).

$$29)\quad 4 \times 10^{6}\ \frac{\text{eV-b}}{\text{a}} \times 10^{-24}\ \frac{\text{cm}^{2}}{\text{b}} \times \frac{1.1\text{x}10^{23}\text{a}}{\text{cm}^{3}} \times \frac{1.6\text{x}10^{-19}\text{J}}{\text{eV}}$$

$$\times\ 10^{13}\ \frac{1}{\text{cm}^{2}} = .7\ \text{J/cm}^{3}$$

This small deposition of energy represents a temperature increase of about .2°C/pulse and thus represents an insignificant perturbation to the pulse heating. This energy will however contribute to the net operating temperature of a first wall.

A proper analysis of the neutron heating can only be done by performing a neutron transport calculation for the entire reactor blanket. Determination of the neutron and gamma flux in the first wall multiplied by the previously discussed KERMA factor will yield the total heating. Calculations of this kind have been performed with the ANISN code[37] for simple spherical blankets and the total heating was found to be about a factor of 2 higher than the simple example above.

The total number of atomic displacements occurring during each pulse can also be estimated in a similar fashion. The displacement cross section for stainless steel is approximately 2220 barns[38] assuming an effective displacement energy of 40 ev. The number of displacements from a source current of 1.7×10^{13} n/cm^2 would be 3.8×10^{-8} dpa. A comparison with time dependent ANISN[37,39] again shows this is about 50% of the total displacements per pulse.

Similar estimates can also be made for gas production and other transmutation reactions. Interaction rate reactions which have threshold energies of a few MeV can be accurately estimated by the above simple procedure since the source current is the primary contribution to the high energy portion of the neutron spectrum.

V. BACKGROUND AND PRECEDENT WORK

V.1 Inertial Confinement Reactor Designs

Fusion by inertial confinement has received a considerable amount of attention in recent years and several groups have proposed reactor concepts using this approach. Although the details of each system vary, certain basic principles are noted in all designs.[40,41]

In each of these systems fuel pellets will be injected into a reactor cavity and a short duration (<10 ns) pulse of energy will be deposited in the periphery of this pellet by: (i) multiple laser beams, (ii) a focused relativistic electron beam, or (iii) a heavy ion beam. Response to this energy deposition in the pellet will be an outward ablation of the surface and an inward compression of the fuel core. When densities and temperatures in the core are sufficiently high, a short duration thermonuclear energy pulse (<1 ns) will occur and proceed until the pellet disassembles. The thermonuclear radiation and the pellet products are then blasted out towards the walls of the cavity. A recent review of the technology to achieve fusion conditions by laser implosion is given by Brueckner in reference 42.

The response of the first wall to this radiation will be determined by the energy partitioning between these products and several different first wall designs have been proposed to safely withstand these irradiations.

One of the earliest laser fusion designs was proposed by Williams, et al.,[43] in which a 1 MJ laser ignited a pellet which produced 100 MJ. A possible first wall consisted of a layer of liquid lithium covering a niobium structure. The function of the liquid lithium is to absorb the ion and photon energy from the microexplosion and ablate, leaving the first wall undamaged. An alternate design for protecting the first wall is magnetic protection as outlined by Frank,[44] et al., which serves to divert the charged particles away from the first wall. An example of the energy partitioning from the pellet explosion for these designs is given in Table 5.

Another design was proposed by Hovingh, et al.[45] which utilized a smaller yield pellet (7 MJ) and lower power laser (.1 MJ). This approach was used to suppress the ablation of a wetted wall by improved pellet design, increased first wall area (through pyramidal first wall topography and increased wall radius), and by reducing the blast energy. Elimination of the ablation eliminated the "blow-off" stress imparted to the first wall in previous designs. Information was also contained in this

TABLE 5

TYPICAL ENERGY RELEASE SPECTRA FOR A 99 MJ PELLET MICROEXPLOSION
(Ref. 44)

	Release Fraction	Particles Per Pulse	Average Energy Per Particle
X-rays	0.01		4 keV peak
α particles (that escape plasma)	0.07	2.2×10^{19}	2 MeV
Plasma kinetic Energy	0.15		
α Particles		1.3×10^{19}	0.6 MeV
Deutrons		1.2×10^{20}	0.3 MeV
Tritons		1.2×10^{20}	0.4 MeV
Neutrons	0.77	3.3×10^{19}	14.1 MeV

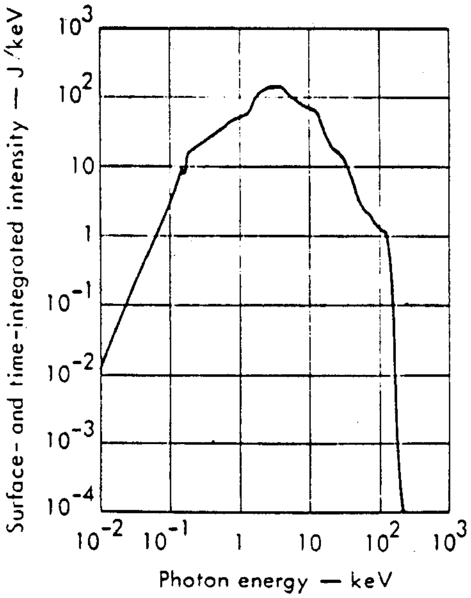

Fig. 14. X-ray Pulse Spectrum of a Megajoule DT Fusion Microexplosion. (Ref. 45)

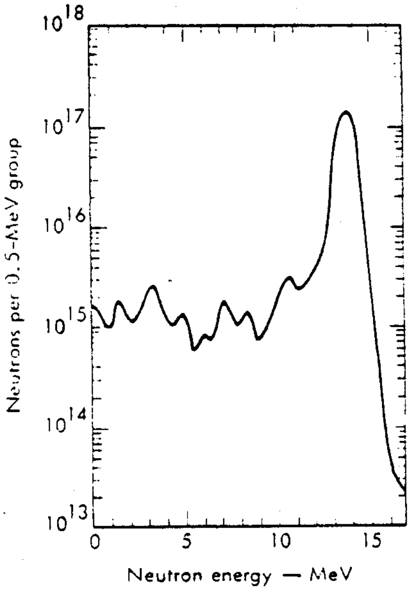

Fig. 15. Neutron Pulse Spectrum of a Megajoule DT Fusion Microexplosion. (Ref. 45)

reference about the typical photon and neutron spectra from a 1 MJ DT fusion microexplosion. These spectra are presented in Figures 14 and 15.

A more recent study by Maniscalco[46] describes a low yield laser fusion reactor which employs a fissile (hybrid) blanket to get energy and fuel multiplication. This concept employs a graphite liner over a stainless steel first wall. The total pellet yield is 10.5 MJ with a laser input to the pellet of 500 KJ.

The first wall response to the microexplosion for this hybrid reactor is described by Hovingh.[20] In addition to x-rays, alphas, neutrons, and pellet debris this analysis considers the laser light which is reflected from the pellet and strikes the first wall. The arrival times for the energy from the pellet and hence the energy deposition time in the first wall is given in Figure 16.

An alternate approach to inertial confinement fusion would utilize relativistic electron beams (REB). Some design considerations for a reactor using REB's is outlined by Varnado and Carlson.[47] Pellets for REB fusion are typically larger and more structured than in laser fusion[48] due to the difficulty in slowing down 1 MeV electrons in short distances. As a result the output spectra are expected to be significantly different. The most significant difference is the large percentage of the energy in x-rays. These x-rays are also quite low in energy which results in

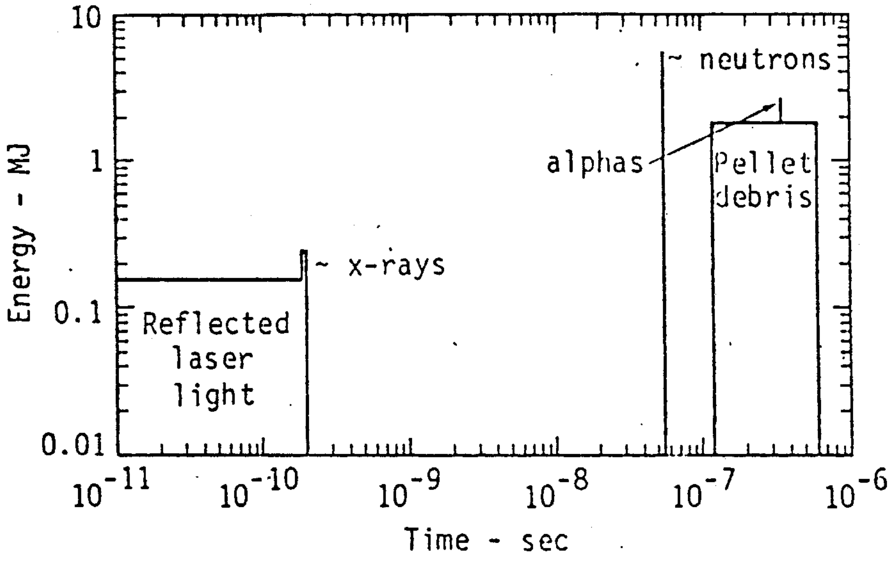

Fig. 16. Time of Arrival of Microexplosion Energy at First Wall Radius of 3.5 m. (Ref. 20)

an extremely short deposition depth. The x-ray spectrum for a 85 MJ microexplosion in a REB fusion system was calculated to be approximately equivalent to a 350 eV blackbody which has peak intensity at 980 eV. A comparison of the relative energy partitioning for all the systems discussed above is given in Table 6.

In all the above references, the response of the first wall to ion irradiation and photon irradiation was evaluated using computer codes such as Chart-D[11] and BUCKL[26]. The latter is used to calculate the energy deposition from photons while the former takes the time dependent energy deposition and determines the vaporization, temperature, and stress wave generation. In all the above

TABLE 6

Reactor Type	E_{in} (MJ)	E_{out} (MJ)	Wall Material	Energy Percentage			
				Neutron	Charged Particle	X-ray	Laser
Laser (Liquid Wall) Ref. 43	1	100	Li/Nb	77	22	1	--
Laser (suppressed ablation) Ref. 45	.1	7	Li/Nb	76	23	1	--
Laser (Hybrid) Ref. 20	.5	10.5	C/SS	73.5	24	1	1.5
E-Beam (Ref. 47)	10.8	96	C	71	12	17	--

studies, however, the synergistic effects of energy deposited from different sources was not investigated[20] nor was a comparison of the displacement damage or subsequent mechanisms. A comparison of the methods used in the above references and the methods proposed in this study will be made in Section VI.

VI. RESPONSE OF MATERIALS TO PULSED IRRADIATION

In this section general models will be developed for the thermal, stress, and displacement response of materials to the radiation spectra discussed in the previous section. Assumptions will be made about the characteristic spectra of an arbitrary pellet and analytical methods to obtain solutions for the response of materials to these spectra will be developed.

VI.1 Spectra and Wall Loading

Specific spectra for certain pellets were discussed in the previous section. These spectra are dependent on the details of the energy source - pellet-fusion interaction and can only be described in detail by sophisticated computer codes such as LASNEX[46] which will not be discussed here. However, the response of a first wall can be determined if the photons, ions, and neutrons are characterized by common spectral forms. The wall loading of various particles for a given spectrum can then be found by determining the spectral dependence of the energy deposition and an assumption about propagation of energy from the source to the first wall.

VI.1.1 Photon Spectra

An often used spectrum for low energy photons is the "Blackbody" or Plankian spectrum[49] which is used when radiation emission is characterized by the temperature of the emitter. A 1 keV blackbody spectrum with a total fluence of 1 Joule/cm^2 is depicted in Figure 17 and is given in practical units by the relation:

30) $$S(E) = \frac{B}{kT}\left(\frac{U^3}{e^U-1}\right) \qquad (\mathrm{J/keV\text{-}cm^2})$$

where $U = E/kT$

kT = characteristic energy, (keV)

$B = 15\ F/\pi^4$

F = total fluence (J/cm^2)

Although the limits on the spectra are 0 and ∞, integration from .1 kT to 10 kT yields 99% of the total fluence.

In a medium with a frequency-independent dielectric constant the propagation of all energies will be at the same velocity. As a result the wall loading from source photons will occur at the same time $\frac{R}{c}$ after creation. The temporal shape of the source will be the temporal shape of the loading pulse. Thus the photon wall loading rate is independent of the spectrum. The production time quoted for D-T pellets is usually around 10 psec.[50]

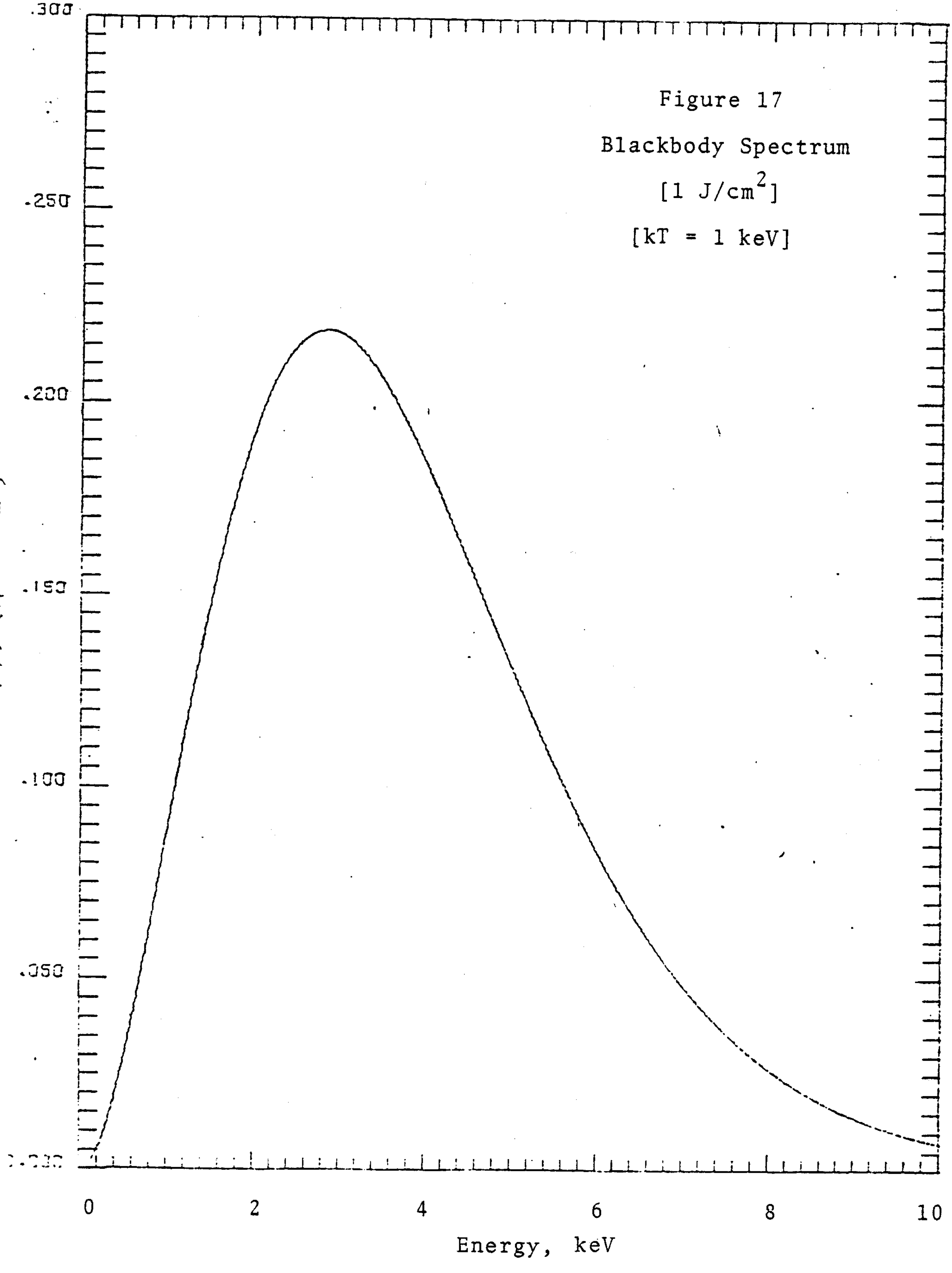
Figure 17
Blackbody Spectrum
[1 J/cm^2]
[kT = 1 keV]
S(E), (J/keV-cm^2)
.300
.250
.200
.150
.100
.050
0.000
0
2
4
6
8
10
Energy, keV

VI.1.2 Ion Spectra

The true ion spectra from a fusion source can again only be determined by a complicated calculation, however, pellet debris calculations[20,40] indicate that reasonable characterization can be made with either a Maxwellian or Gaussian distribution. A Maxwellian is characterized by a mean energy E_m and can be represented in the practical form:

$$31)\qquad S(E) = \frac{2N}{\pi^{\frac{1}{2}} E_m} \left(\frac{E}{E_m}\right)^{\frac{1}{2}} e^{-E/E_m} \qquad (1/\text{keV})$$

where E_m = characteristic energy
E = ion energy (keV)
N = total number of ions or ions/cm^2 if F is to be a fluence

The Gaussian distribution is useful when a spectrum of a specific width is required. Two parameters are necessary to describe the distribution as:

$$32)\qquad S(E) = \frac{N}{\sqrt{2\pi}\,\sigma} e^{-\frac{1}{2}\left(\frac{E-E_m}{\sigma}\right)^2} \qquad (1/\text{keV})$$

where E_m = mean energy (keV)
σ = standard deviation (keV)

Both spectra range from 0 to ∞ but practical limits of $E_m/8$ to 4 E_m yield 91% of the total fluence in a Maxwellian distribution; similarly, a range of $\pm 2\sigma$ yields 95% of the total for a Gaussian distribution.

If the ion production time is short compared to the transit time to the first wall, the entire ion distribution may be assumed to be created as an impulse function in time at a single point in space. The time duration of the loading of the first wall will be determined by the time for each species to arrive. This assumption is only valid for a collisionless plasma which does not have significant self encounters or encounters with gas species which reside in the chamber. If significant collisions occur with chamber gas atoms, a spherical blast wave can be generated[44] and hence a loading pulse applied to the first wall.

In the collisionless case, the loading function for the first wall may be derived for a given wall radius if the spectrum at $t = 0$ and $r = 0$ is specified. This can be done by transforming the distribution from energy to time as:

33) $$S(E)\ dE = -F(t)\ dt$$

34) $$t = B/E^{\frac{1}{2}}\ (\text{sec})$$

where $B = 2284 \times 10^{-9} \; r\sqrt{A}$

r = wall radius (meters)

A = ion mass (amu)

thus

$$F(t) = S(E)\,\frac{2E^{3/2}}{B} \qquad (\mathrm{sec}^{-1}\ \mathrm{cm}^{-2}) \tag{35}$$

The incident energy arrival rate is given by

$$W(t) = F(t)\ 1.6 \times 10^{-16}\ E \quad (\mathrm{J/sec\text{-}cm}^2) \tag{36}$$

where E = keV

and the pressure due to the momentum of the particles is

$$P(t) = 7.29 \times 10^{-17}\ A^{1/2}\ E^{1/2}\ F(t) \quad (\mathrm{dynes/cm}^2)\ \text{or}\ (10^{-6}\ \text{bars}) \tag{37}$$

Equation 35 also represents the temporal distribution of the energy deposition at any point in the material. This is true because the slowing down time for an ion is on the order of 10^{-12} seconds[51] while the time duration of the ion pulse is on the order of 10^{-6} seconds. (A 100 keV Alpha particle has a velocity of 2×10^8 cm/sec and slows down in approximately 10^{-4} cm hence $\Delta\tau = 10^{-4}/10^8$.) Equation 36 is not very useful since it represents the energy which crosses the inner boundary of the first wall and the spatial distribution of the deposition must be specified to obtain a true loading rate. Equation 37 has meaning only if the particles are stopped within the first wall.

VI.1.3 Neutron Spectra

In the past, neutron production from the fusion pellet has been erroneously characterized as a monoenergetic 14.1 MeV neutron source. Reference to Figure 15 indicates that the spectrum has finite width for the thermonuclear neutrons.

This broadening of the neutron spectrum is a natural consequence of the motion of the fusing nuclei. These nuclei have both a directed and thermal velocity. Each velocity component will alter the energy partitioning between the fusion products. The energy of the emitted neutron is a function of these velocities in a center of mass frame between two colliding nuclei and of the angle of emission of the neutron, which is usually assumed isotropic in D + T plasmas. Combination of these effects will give a considerable spread to the neutron spectrum of a fusing source.

This effect has been calculated by Lessor[52] for stationary plasmas which might be typical of Tokamaks or

Mirrors and an example of a spectrum for a 100 keV plasma is shown in Figure 18.

A similar calculation has been performed for a fusing pellet by Shuy,[53] accounting for both thermal and directed motion. The spectrum from this calculation is shown in Figure 19. Both these calculations show broadening of about ± 1 MeV, which is in reasonable agreement with Figure 15. In addition these spectra can be approximated by a Gaussian pulse (Eqn. 32) as previously described.

An important aspect of this spectral broadening is that the temporal loading of the first wall is not determined by the source duration. Instead the pulse duration is determined by the transit time broadening as calculated by Eqn. 35 which accounts for the variation in arrival times for different energies. This effect will determine the interaction rates for neutrons in the first wall.

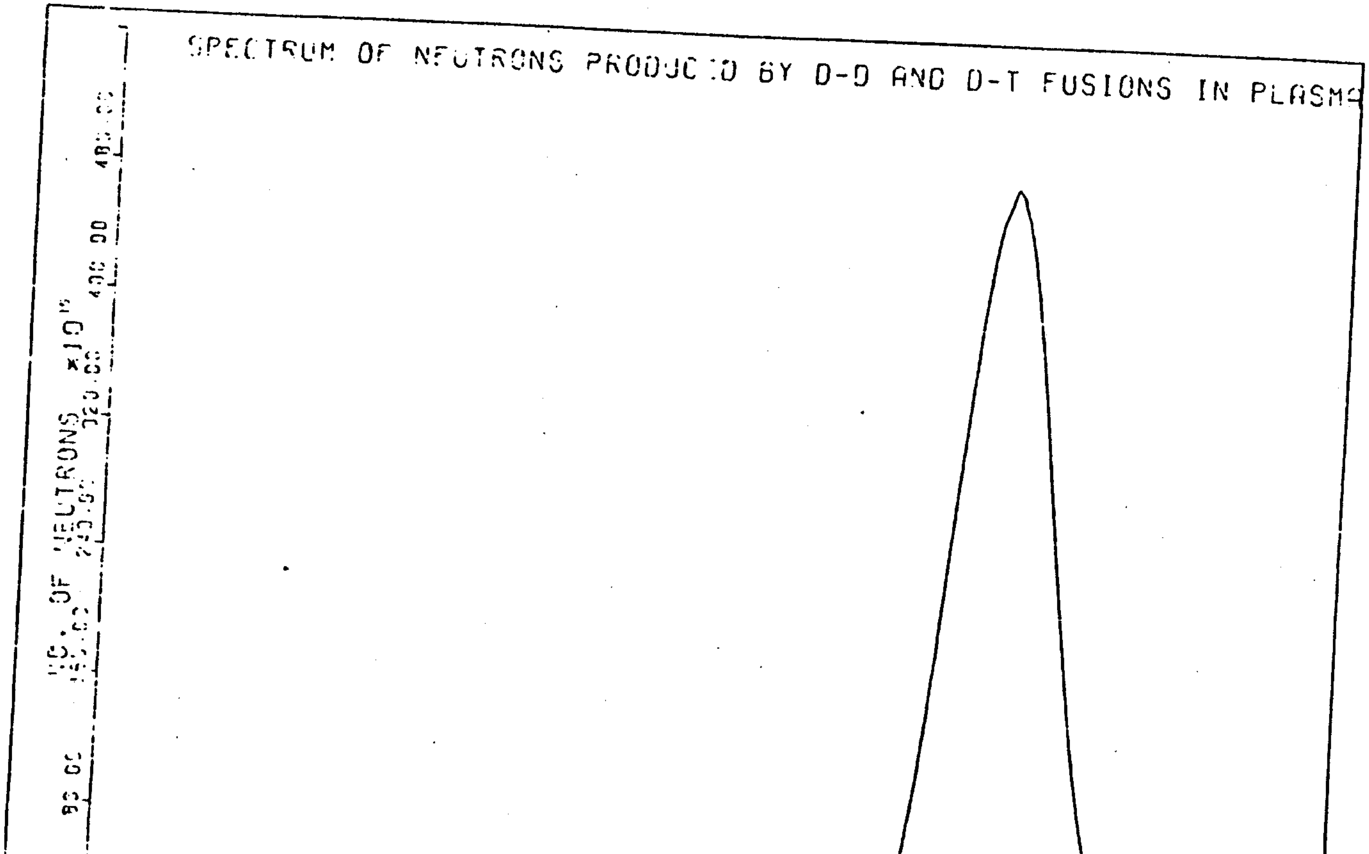

SPECTRUM OF NEUTRONS PRODUCED BY D-D AND D-T FUSIONS IN PLASMA

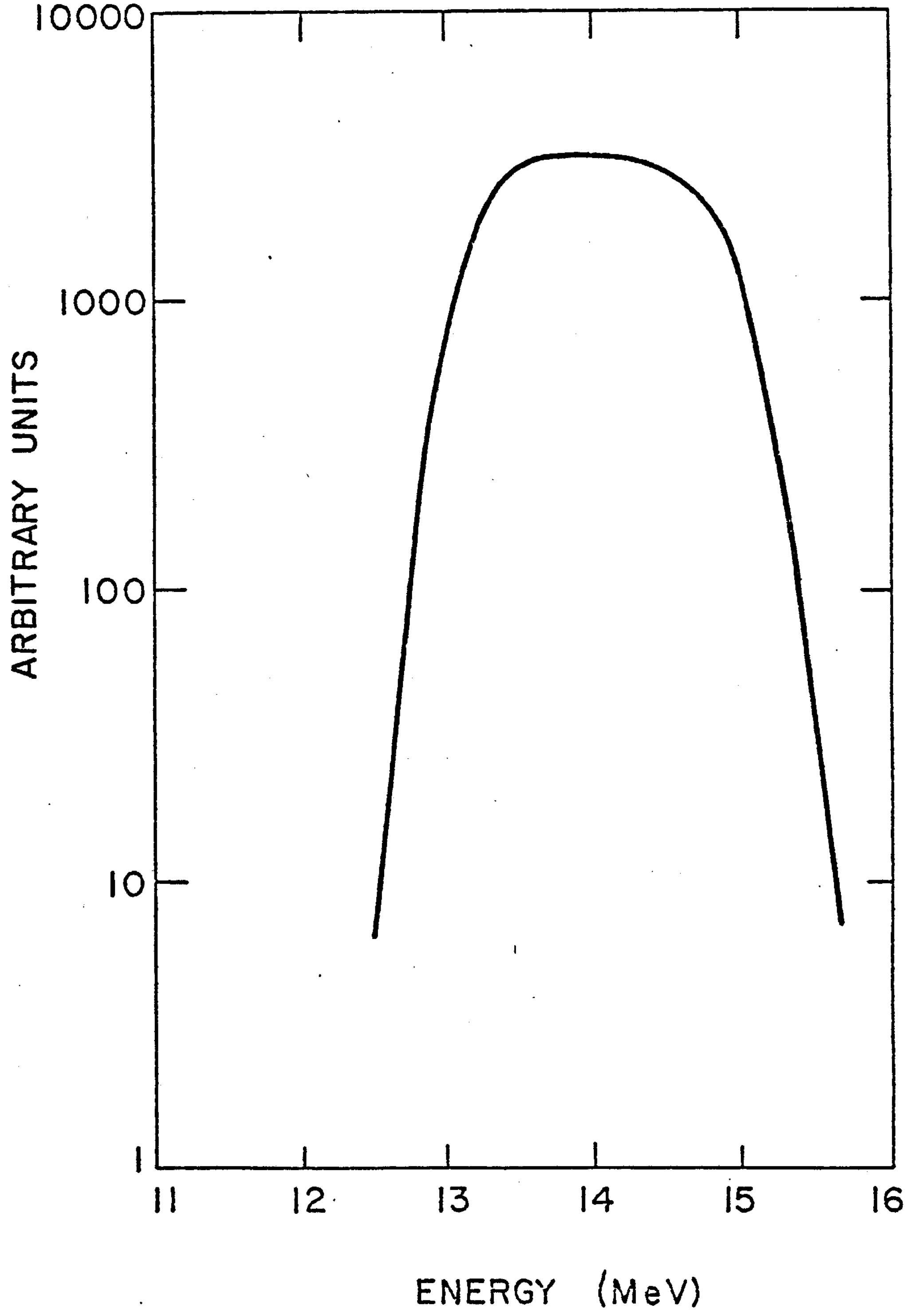

Neutron Energy Spectrum
From D + T Microexplosion
(Ref. 53)

Figure 19

VI.1.4 Summary of Wall Loadings

The photons, neutrons, and ions can be approximated as all created instantaneously with spectra given by the previous generalizations. The wall fluxes from these sources can then be calculated from the relations developed above. An example of the wall loadings for the following three general sources at a radius of 5 meters is given in Figure 20:

		Fluence/Pulse	
	Spectrum	Particles	Energy
Photons --	500 eV Blackbody	$1 \times 10^{15}/cm^2$	$.3\ J/cm^2$
Neutrons --	14 MeV ± 1 MeV (Gaussian)	$10^{13}\ n/cm^2$	$22.4\ J/cm^2$
Alphas --	200 keV (Maxwellian)	$10^{13}\ \alpha/cm^2$	$.48\ J/cm^2$

These spectra are representative of three individual radiation types which are used to demonstrate the response of materials. They do not represent a complete set of radiation types of spectra from an inertially confined fusion microexplosion.

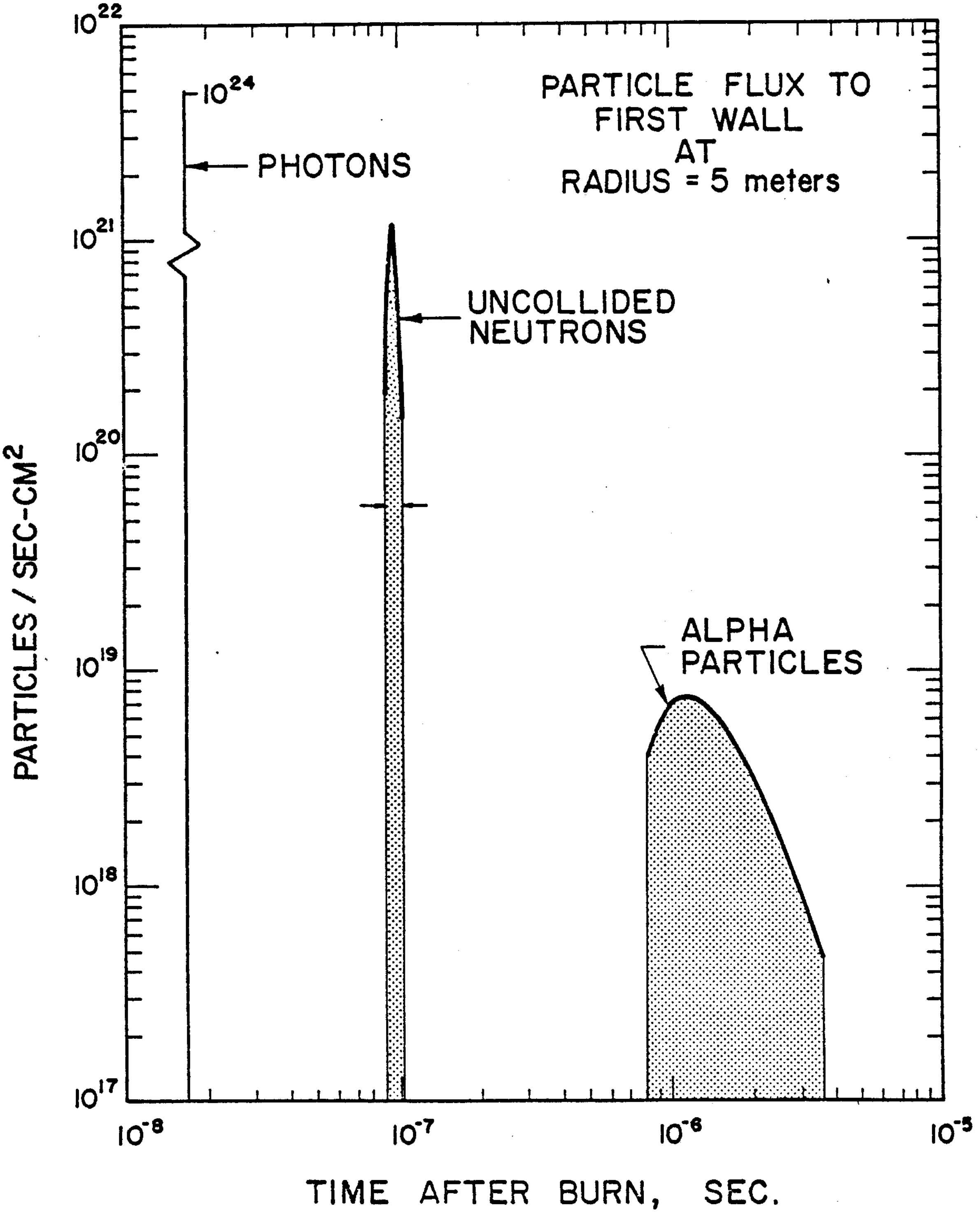
PARTICLE FLUX TO FIRST WALL AT RADIUS = 5 meters
10^24
PHOTONS
UNCOLLIDED NEUTRONS
ALPHA PARTICLES
10^22
10^21
10^20
10^19
10^18
10^17
PARTICLES / SEC-CM^2
10^-8
10^-7
10^-6
10^-5
TIME AFTER BURN, SEC.

Figure 20

VI.2 Energy Deposition

The energy deposited in a material can be calculated from the appropriate relation for energy loss for each radiation type. Photons are exponentially attenuated with absorption coefficients given in Section IV, source neutrons as in Equation 29 and ions by Equation 24. The temporal distribution is determined by Equation 35 upon specification of a spectrum.

The heating rate from the three reference radiation distributions in graphite can be determined from the appropriate energy deposition rate and is displayed in Figure 21. The greatest heating rate is given by the photons which are assumed to be deposited over a period of 1 ns. The correct deposition time would be a combination of the source time and the electron slowing down time, but the latter was not considered here.

The data in Figure 21 can be deceptive since it represents the power into the material. A more meaningful comparison would be the total deposited energy or the time integral of the power curves. These data are shown in Figure 22. In this case the maximum energy deposited is due to the alpha particles.

The response of the material to these radiations is a function of the amplitude and the rate of the deposition,

Figure 21

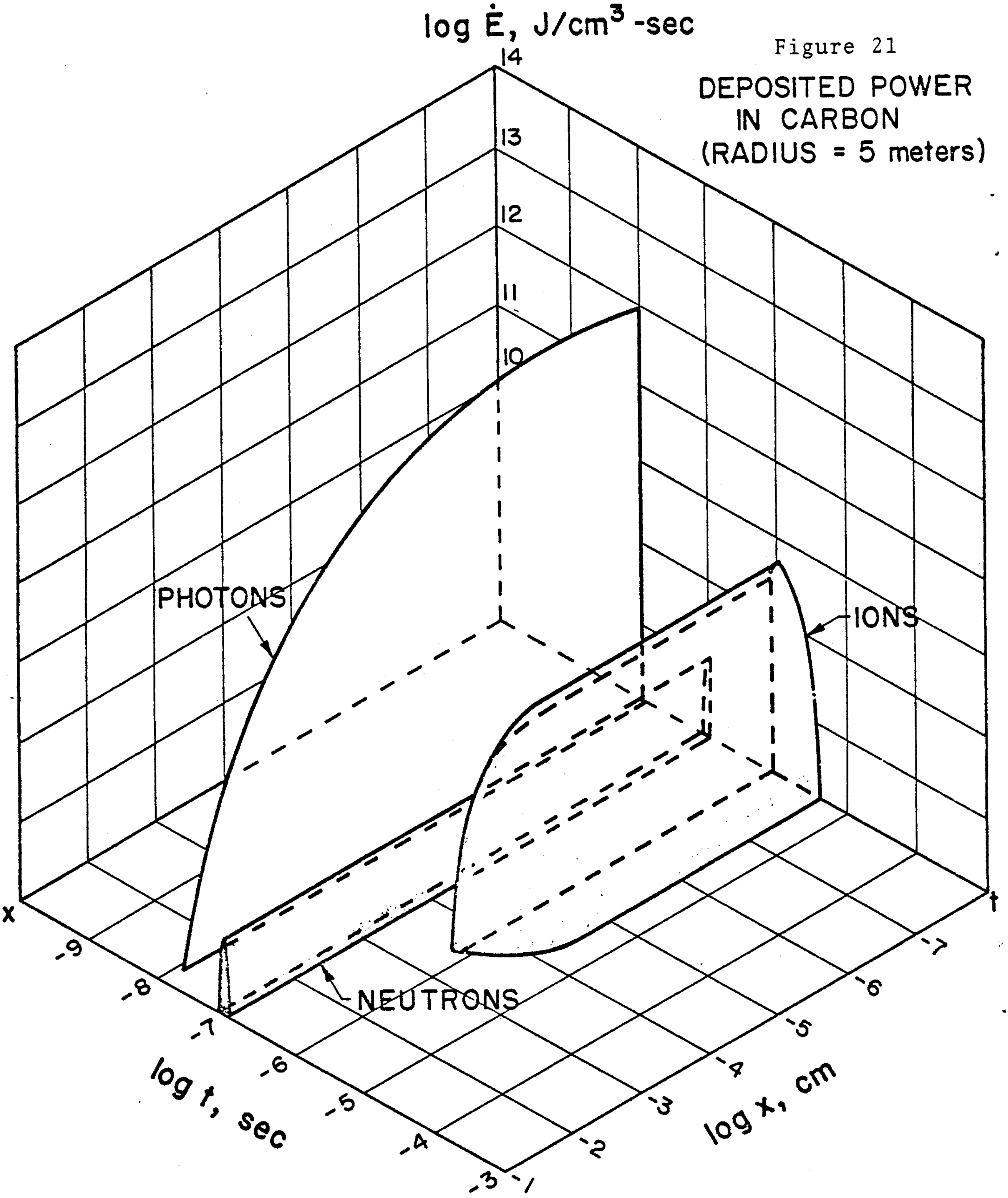

DEPOSITED POWER IN CARBON (RADIUS = 5 meters)

Figure 22

DEPOSITED ENERGY IN CARBON (RADIUS = 5 meters)

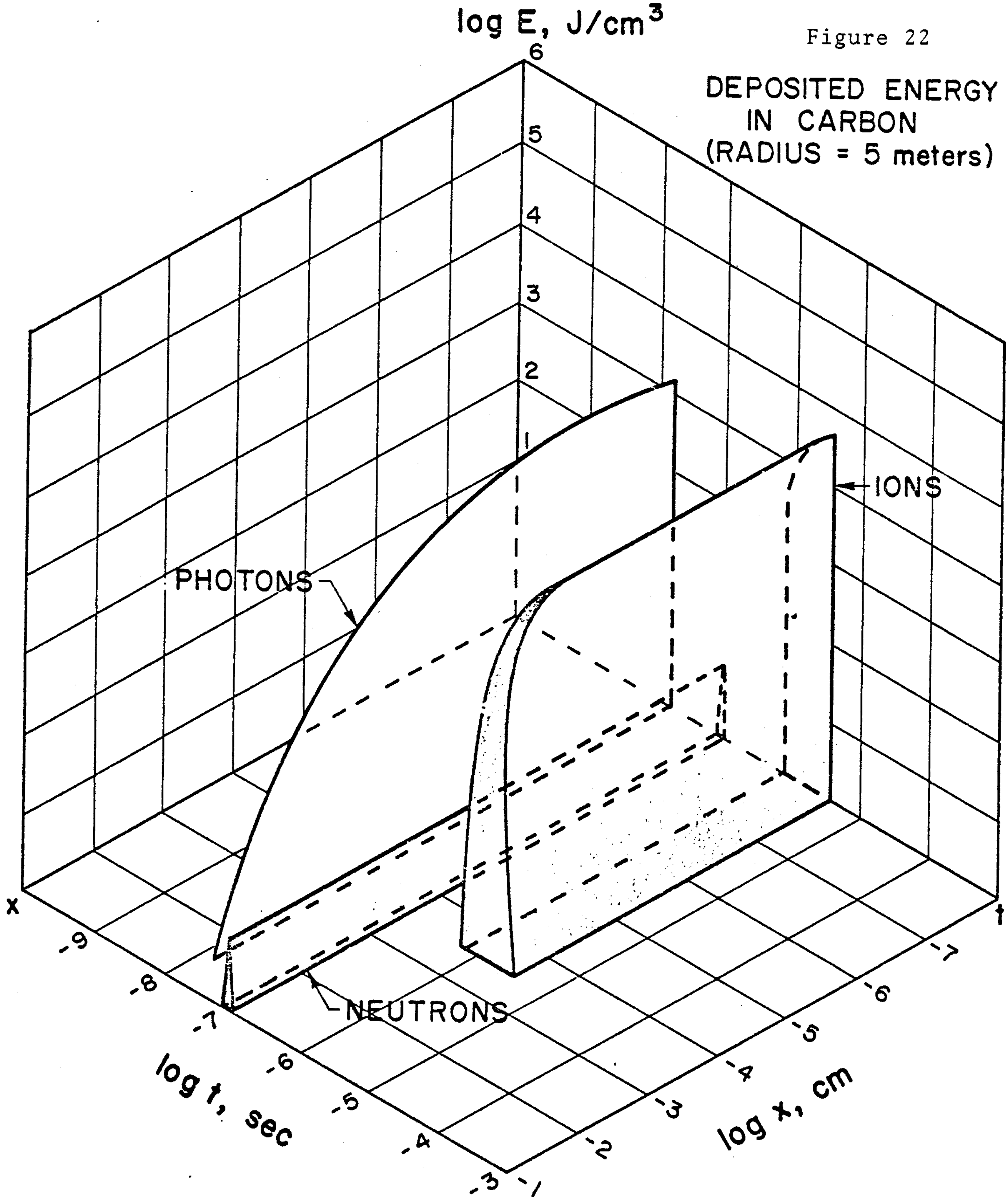

since it is necessary to account for energy which is transferred away from the deposition.

VI.3 Thermal Response

The temperature history associated with the deposition of energy from the various radiation sources discussed in the previous sections can be determined by numerous calculational methods. The emphasis in this study will be a parametric analysis and thus closed form solutions will be developed for thermal response of single phase materials with constant material properties. More refined calculations are readily done via numerical methods which can account for melting, vaporization, and non-linear material properties. An attempt to include these effects will be made when possible.

The temperature excursion from neutron radiation has been shown to be insignificant in pulsed fusion environments hence we only need to develop models for photon and ion deposition.

VI.3.1 Response to Photon Irradiation

If the energy deposition from photons can be described by exponential attenuation (as in the case of photoelectric absorption), it is sufficient to develop a response model for monoenergetic radiation which can then be applied to arbitrary spectra by superposition.

The prompt temperature excursion following a pulse of electromagnetic radiation can be determined easily if the pulse time is shorter than the thermal response time of the irradiated material. If this condition is met, the initial temperature transient can be calculated from an adiabatic model. It is therefore instructive to examine the photon pulse durations which will satisfy these conditions.

VI.3.1.1 Adiabatic Response

An estimate of the thermal response time can be made from examination of the case of monoenergetic photon absorption in which the energy deposition is given by

38) $$q = \mu F_o \; e^{-\mu x}$$

where q = energy/unit volume

F_o = incident intensity, energy/unit area

If the energy were deposited instantaneously, the material would respond adiabatically and the resulting temperature change profile would be of the form

39) $$T(x) = T_o \; e^{-\mu x}$$

where $T_o = \frac{\mu F_o}{\rho C}$

A conservative estimate of the thermal response time can be made examining the heat conduction equation[54]

40) $$k\nabla^2 T + \dot{q} = \rho C \frac{\partial T}{\partial t}$$

Since the first term in Equation 40 represents the power lost (or gained) by a volume element, the maximum rate of energy transfer by conduction can be estimated from the temperature gradient derived from Equation 39:

41) $$\frac{\partial T(o)}{\partial x} = -\mu T_o e^{-\mu(o)} = -\mu T_o$$

(42) $$\frac{\partial^2 T(o)}{\partial x^2} = \mu^2 T_o = \frac{\mu^3 F_o}{\rho C}$$

A comparison of the first and second terms in Equation 40 can then be made for depositions over finite time t , in which

43) $$\dot{q} = \frac{\mu F_o}{\Delta t} e^{-\mu x}$$

hence the rates of terms 1 and 2 in Equation 40 become equal, at $x = 0$, when

44) $$\frac{k\nabla^2 T}{\dot{q}} = \frac{k\mu^2 \Delta t}{\rho C}$$

or the deposition time in which the maximum conduction loss rate is equivalent to the energy deposition rate is

45) $$\Delta t = \frac{\rho C}{k\mu^2} = \frac{1}{\alpha\mu^2}$$

where α = thermal diffusivity, cm^2/sec

μ = absorption coefficient, cm^{-1}

Typical data for graphite and copper are given in Table 7.

TABLE 7

	Δt(sec)	ρ(gm/cm^3)	C($\frac{cal}{gm°K}$)	k($\frac{cal}{cm°K\ sec}$)	μ(cm^{-1}@1keV)
C	$4x10^{-7}$	2.3	.4	.1	5000
Cu	$1.07x10^{-10}$	8.9	.092	.85	95000

Conservative choices would be to chose values of Δt a factor of 10 lower than those shown in Table 7. Thus for pulse times of 10 psec, the response of graphite to 1 keV photons is very nearly adiabatic; whereas, for more strongly absorbing materials like Cu, the adiabatic assumption probably overestimates the temperature.

Using this adiabatic assumption, the temperature excursions from each photon pulse in an inertially confined fusion environment can be found using Equation 39 upon specification of the source spectrum and the photon cross sections. An example of these peak temperatures is shown in Figure 23. The maximum front surface temperature and the maximum temperature at a penetration distance of 1 μm are given as a function of Blackbody temperature. A spatial profile of temperature at various positions within the material is shown in Figure 24 for Blackbody temperatures of .4, .5, .6 keV.

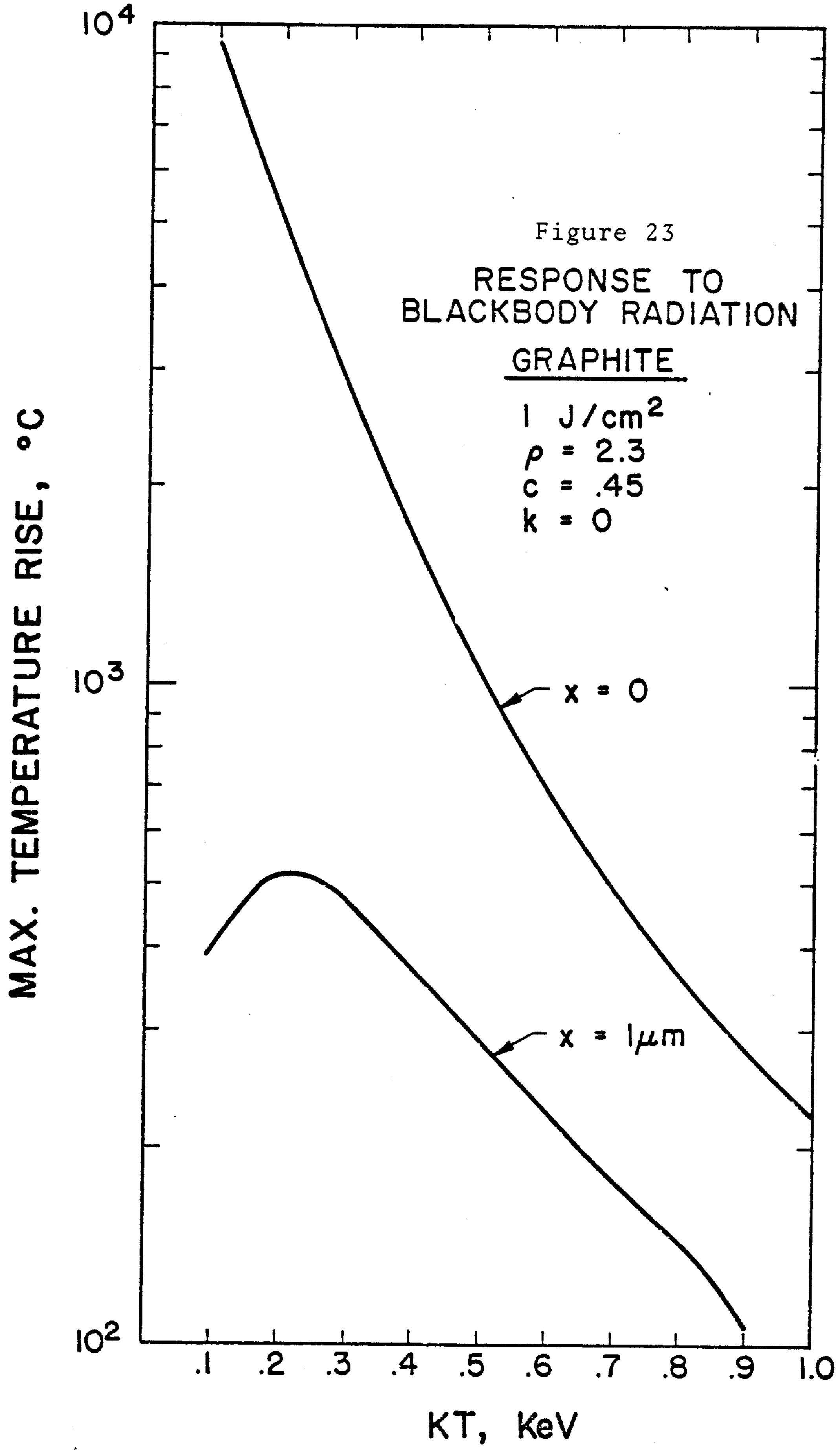

Figure 23

RESPONSE TO BLACKBODY RADIATION

GRAPHITE

1 J/cm^2
ρ = 2.3
c = .45
k = 0

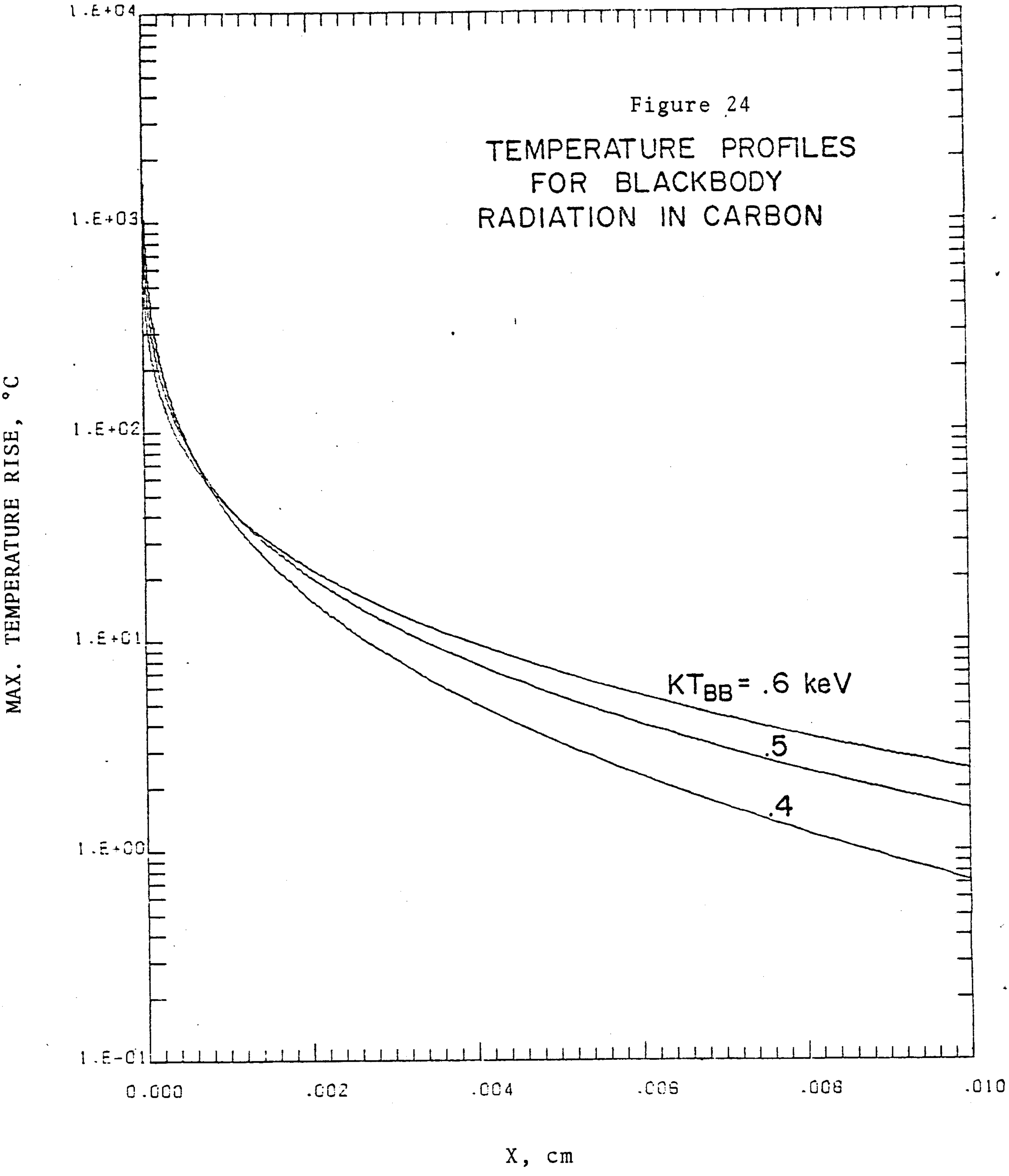
Figure 24
TEMPERATURE PROFILES FOR BLACKBODY RADIATION IN CARBON
1.E+04
1.E+03
1.E+02
1.E+01
1.E+00
1.E-01
MAX. TEMPERATURE RISE, °C
0.000
.002
.004
.006
.008
.010
X, cm
KT_BB = .6 keV
.5
.4

VI.3.1.2 Total Response to Photon Radiation

In addition to the peak temperature it is necessary to determine a complete temperature history at any point in the irradiated material. In the following development a general model will be given for a pulse train of photon irradiations. The impulse response will first be determined for a single pulse and then generalized to many pulses and finally related to photon pulses of finite duration.

The energy deposition can be assumed to be given by

46) $$q(t,x) = \delta(t)\ q(x) = \delta(t)\ q_o e^{-\mu x}$$

From consideration of the adiabatic response the temperature in a finite slab of width L can be formulated as

47) $$\nabla^2 T = \frac{1}{\alpha}\ \frac{\partial T}{\partial t}$$

subject to

$$T(x,0) = f(x) = \frac{q_o}{\rho C}\ e^{-\mu x}$$ [initial condition due to adiabatic response]

$$\frac{\partial T}{\partial x}(0,t) = 0$$ (insulated face)

$$T(L,t) = 0$$ (constant rear surface temperature)

By separation of variables or transform methods, the solution to the above problem can be shown to be[55]

$$48)\quad T(x,t) = \sum_{N=0}^{\infty} \cos B_n \frac{x}{L}\, e^{-B_n^2 \Theta}\, \frac{2}{L}\int_0^L f(x) \cos B_n\, x/L\, dx$$

where $B_n = (\frac{2n-1}{2})\pi$

$\Theta = \frac{\alpha t}{L^2}$

Upon substituting for $f(x)$ and integrating the result is:

$$49)\quad \frac{T\;(x,t)}{q_o/\rho C} = 2 \sum_{N=1}^{\infty} \cos B_n z\; e^{-B_n^2\Theta}\left[\frac{b}{b^2+B_n^2}\right]$$

$$\left[1-e^{-b}\;(\cos B_n - \frac{B_n}{b} \sin B_n)\right]$$

where $b = L$ $\qquad$ $z = x/L$

This is the response to a single photon pulse; a series of pulses as shown in Figure 25 can be accommodated by applying Laplace transform techniques to Equation 47.

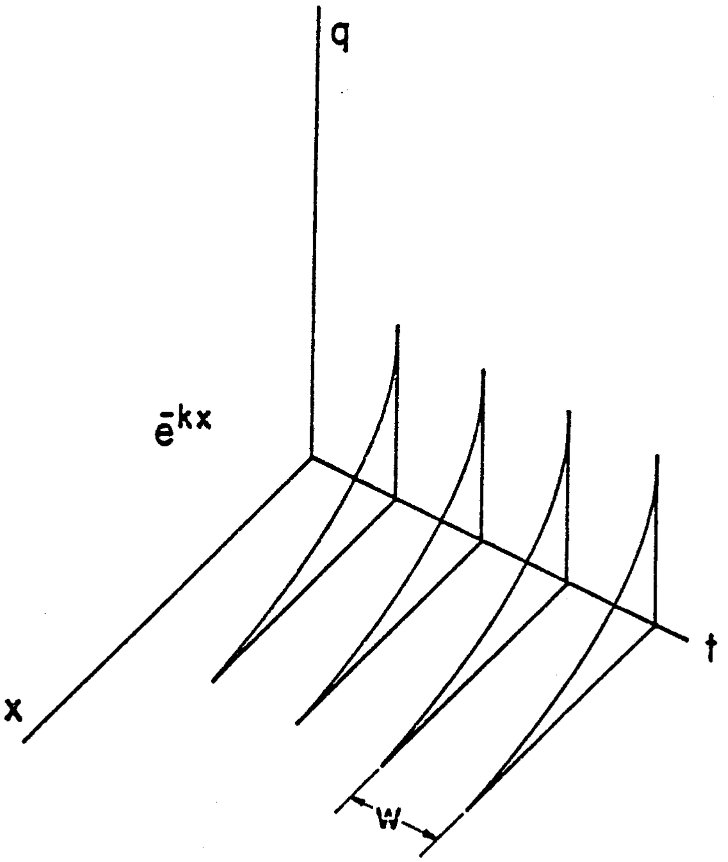

Fig. 25. Energy Deposition From Photon Pulse Train

The temporal behavior of the loading function is thus given by

$$50)\qquad q(t) = \sum_{n=0}^{M-1} \delta(t-n_{\omega}) = \delta(t) + \delta(t-\omega) + ---$$

where M = number of pulses which have occurred

ω = time between pulses

which has a transform of

51) $$V(s) = 1 + e^{-\omega s} + e^{-2\omega s} + \cdots$$

The transfer function for the system is the transform of Equation 49, which is

52) $$H(s) = 2\sum_{N=1}^{\infty} \cos B_n z \, \frac{1}{s+\frac{B_n^2\alpha}{L}} \left[\frac{b}{b^2+B_n^2}\right] \left[1-e^{-b}\left(\cos B_n - \frac{B_n}{b}\sin B_n\right)\right]$$

The response to a series of M pulses is then found by multiplying Equations 51 and 52 and finding the inverse transform as

53) $$\frac{T(x,t)}{T_o} = 2\sum_{n=1}^{\infty} \cos B_n z \, e^{-B_n^2\Theta} \left[\frac{1-e^{-B_n^2\gamma M}}{1-e^{-B_n^2\gamma}}\right] \left[\frac{b}{b^2+B_n^2}\right]$$

$$\left[1-e^{-b}\left(\cos B_n - \frac{B_n}{b}\sin B_n\right)\right]$$

where $B_n = \frac{(2n-1)\pi}{2}$

$\gamma = \frac{\alpha w}{L^2}$

$b = \mu L$

$\Theta = \frac{\alpha\delta}{L^2}$

$T_o = \frac{q_o}{\rho C}$

δ = fraction of pulse interval

α = thermal diffusivity

This solution can be generalized to pulses of finite duration by convolution or reapplying transforms and this analysis will give a result identical to a variation of parameters analysis by Abdel-Khalik.[56] For short photon mean free paths an analysis based on an infinite half space solution would also be convenient and could be evaluated without the detriment of evaluating an infinite series.

An interesting result from the application of Equation 53 is the shape of the temperature profile in a material just before a photon pulse due to the response of a large number of precedent pulses. Figure 26 shows such a prepulse profile for a .5 keV Blackbody of 1 J/cm^2 on a graphite slab 1 cm thick. The spacing between pulses was 1/15 seconds. The small variation in front to back surface temperatures (10°C) is to be contrasted to the prompt temperature excursion of 1000°C under the same irradiation conditions.

A treatment similar to the derivation of Equation 53 can be applied to a slab cooled by convection which results in a similar expansion with different eigenvalues as:

$$54)\quad \frac{T(x,t)}{T_o} = 2 \sum_{n=1}^{\infty} \frac{B_n}{B_n + \sin B_n \cos B_n} \cos B_n z \; e^{-B_n^2 \Theta}$$

$$\left[\frac{1-e^{-B_n^2 \gamma M}}{1-e^{-B_n^2 \gamma}}\right] \left[\frac{b}{b^2 + B_n^2}\right] \left[1-e^{-b} \left(\cos B_n - \frac{B_n}{b} \sin B_n\right)\right]$$

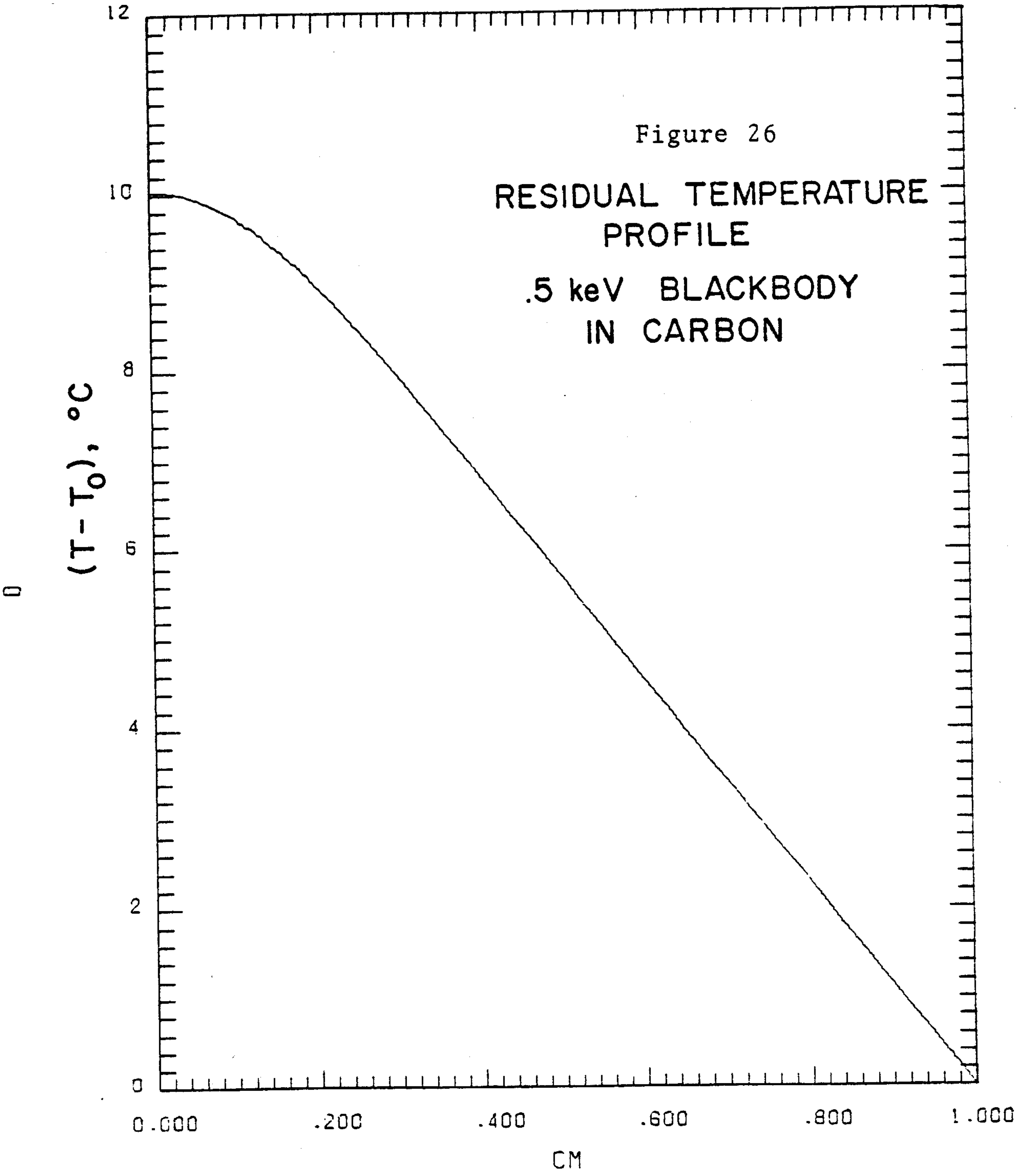

Figure 26

RESIDUAL TEMPERATURE PROFILE

.5 keV BLACKBODY IN CARBON

where B_n are the roots of $\cot B_n = \frac{B_n}{hL/k}$

V.3.2 Thermal Response to Ion Sources

As previously discussed, energetic charged particles have different energy loss mechanisms than photons. Consequently, different models are necessary to predict the thermal response. In this section two models will be shown: one partially developed by previous investigators[60] but further developed by this study and one developed completely during this study.

The response to the deposition of charged particle energy has been determined by various investigators. Behrisch[57] used a model based on energy flux continuity at the irradiated surface (this model is also used for electromagnetic radiation by Ready[58]). Frank, et al.[59] used a model based on uniform spatial and temporal deposition taken from calculations by Axford.[60] Hovingh[20,61] used the same deposition assumption, but evaluated the temperature numerically with the Chart-D code.

VI.3.2.1 Uniform Deposition Model

The work of Frank, et al., considered the response of an infinite half space subject to an energy deposition shown in Figure 27. The solution was only given for the resulting surface temperature as a function of time. The response at any position and time was derived as part of this study.

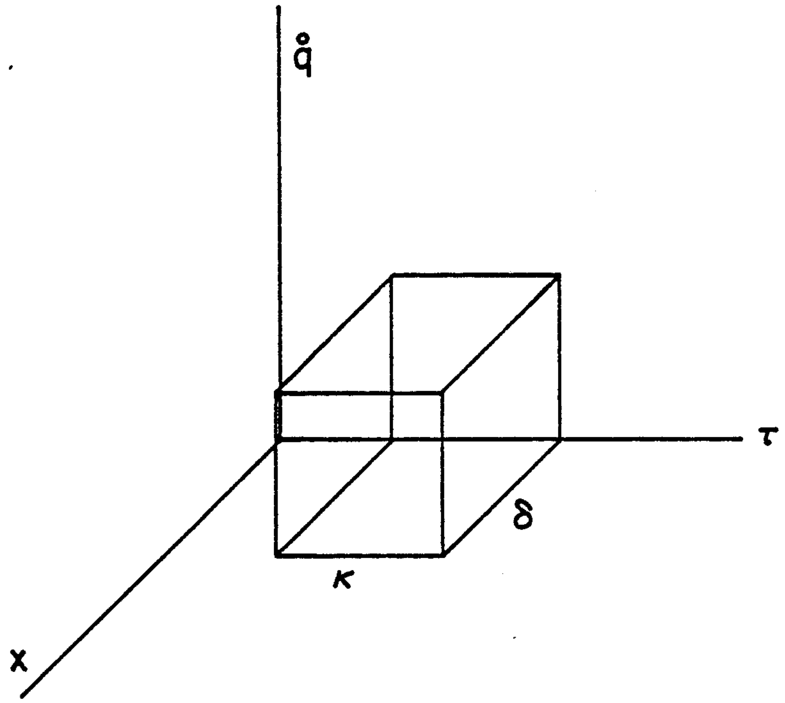

Fig. 27. Uniform Energy Deposition Model

A summary of that derivation follows. The deposition is given by:

55) $$\dot{q}(x,t) = F \frac{1}{\delta} \frac{1}{K} \quad \text{where } F = \frac{\text{incident energy}}{\text{unit area}}$$

δ = deposition region

K = deposition duration

The response to an impulse function in time can be determined from the equations

$$56)\qquad k\nabla^2 T = \frac{\partial T}{\partial t}\;\frac{1}{\alpha}$$

$$\frac{\partial T}{\partial x}(0,t) = 0$$

$$T(x,0) = \frac{F}{\delta\rho C} \qquad 0 < x < \delta$$

$$T(x,0) = 0 \qquad \delta < x < \infty$$

This result can be found by integrating the Green's function[55] for a half space over the deposition interval as:

$$57)\qquad T(x,t) = \frac{F}{\delta\rho C}\,\frac{1}{2}\left[\operatorname{erf}\left(\frac{\delta - x}{2\sqrt{\alpha t}}\right) + \operatorname{erf}\frac{(x+\delta\;)}{2\sqrt{\alpha t}}\right]$$

Another integral over the finite duration of the pulse yields:

$$58)\qquad \frac{T(x,t)}{F/\rho C\delta} = \frac{1}{K}\left\{a_1^2\left[F\left(\frac{a_1}{(t-b)^{\frac{1}{2}}}\right) - F\left(\frac{a_1}{t^{\frac{1}{2}}}\right)\right]\right.$$

$$\left. + \, a_2^2\left[F\left(\frac{a_2}{(t-b)^{\frac{1}{2}}}\right) - F\left(\frac{a_2}{t^{\frac{1}{2}}}\right)\right]\right\}$$

where $a_1 = \frac{\delta - x}{2\sqrt{\alpha}}$ $\qquad a_2 = \frac{\delta + x}{2\sqrt{\alpha}}$

$$F(v) = \frac{-\operatorname{erf}(v)}{2v^2} - \frac{e^{-v}}{\sqrt{\pi}\;v} - \operatorname{erf}(v)$$

α = thermal diffusivity $\quad b = K,\ t > K$

ρ = density $\quad b = t,\ t \leq K$

C = specific heat

The maximum surface temperature can be determined from Equation 47 at $X = 0$ and $t = K$ as

$$59)\quad T(0,K) = \frac{F}{\delta\rho C}\left[\operatorname{erf}(u) - 2u^2 \operatorname{erfc}(u) + \frac{2u}{\sqrt{\pi}} e^{-u^2}\right]$$

where $u = \delta/2\sqrt{\alpha K}$

This result is identical to that of Axford and Frank.[59,60] The response predicted by this model for a deposition of energy into the first μm of a material over duration of 10 ns and 100 ns is shown in Figure 28.

Figure 28

THERMAL RESPONSE TO UNIFORM DEPOSITION PROFILE

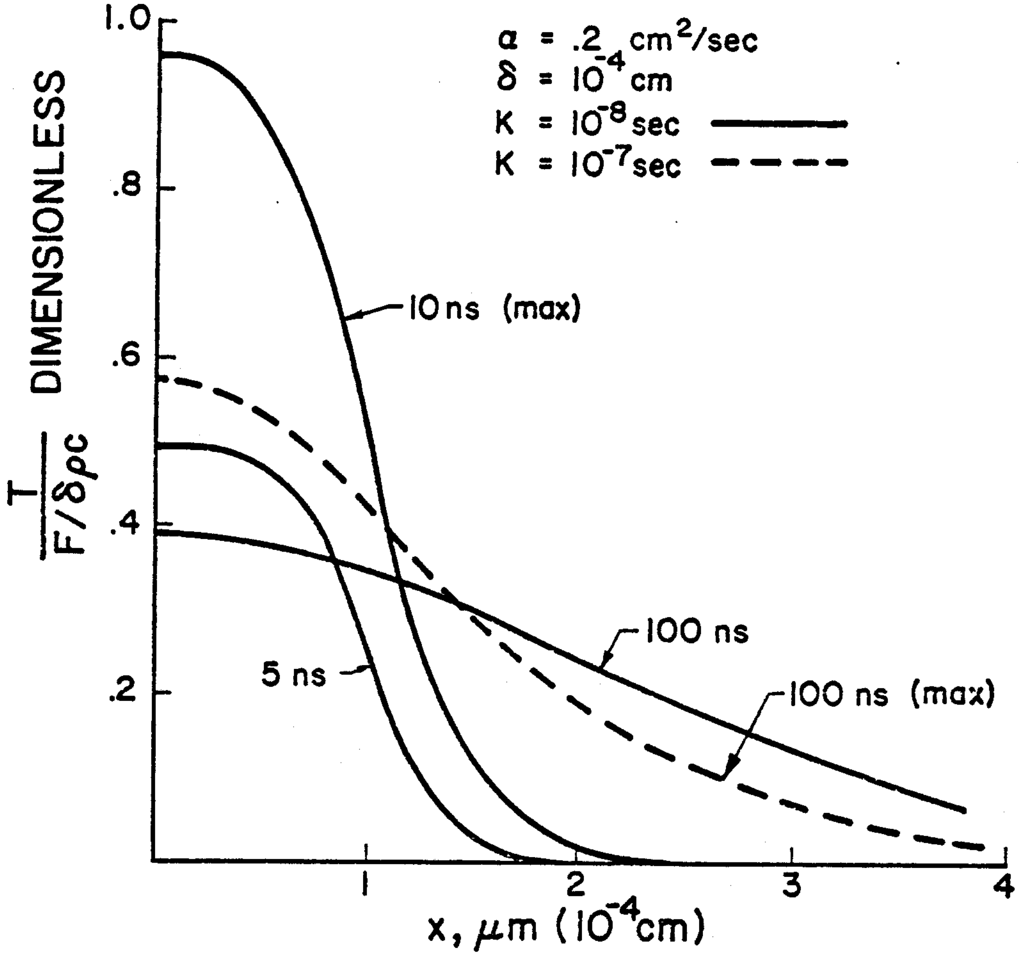

VI.3.2.2 General Model for Low Energy Ions

The previous model (Equation 57) is not suitable for parametric study of ion deposition of arbitrary spectra because it does not adequately account for the energy loss mechanisms. Equation 57 can, however, be applied to arbitrary deposition profiles via superposition techniques.

This deficiency in current models has also led to the development of a new model which would incorporate the appropriate slowing down models and allow for realistic spectra and pulse shaping. This model is currently applicable to the low velocity region for charged particles where the energy loss can be expressed with a modified Lindhard model in the following form:

$$\frac{dE}{dx} = -C\left(\frac{E}{E_o}\right)^{\frac{1}{2}} \tag{60}$$

The average spatial distribution for a particle of energy E_1 can be expressed by the transforming from energy to position by

$$x = \int_{E_1}^{E} \frac{1}{dE/dx}\, dE$$

which yields

$$\frac{dE}{dx}(x) = \frac{xC^2}{2E_o} - C\left(\frac{E_1}{E_o}\right)^{\frac{1}{2}} \tag{61}$$

The volumetric energy deposition rate can be determined if Equation 61 is combined with the energy arrival density of Equation 35 for a spectrum of particles which undergo collisionless transport to the deposition surface.

Thus (letting $E_1 = E$)

62) $$q(x,t) = S(E)\,\frac{2E^{3/2}}{B}\left[\frac{CB}{E_o^{\frac{1}{2}}\,t} - \frac{XC^2}{2E_o}\right], \qquad X < \frac{2BE_o^{\frac{1}{2}}}{tC}$$

$$= 0\ , \quad X > \frac{2BE_o^{\frac{1}{2}}}{tC}$$

where the range on t is

$$\frac{B}{\sqrt{E}_{min}} > t > \frac{B}{\sqrt{E}_{max}}$$

E_{min}, E_{max} = limits of spectrum

The general solution for temperature at position X and time t in a semi-finite solid with insulated boundary at X = 0 can be expressed in terms of the Green's function as

63) $$T(x,t) = \int_t \int_x \frac{q(x',t')}{C}\ G(x,t,x',t')\ dx'\ dt'$$

where

$$64)\quad G(x,t,x',t') = \frac{1}{2\sqrt{\pi\alpha(t-t')}} - \left[e^{-\frac{(x-x')^2}{4\alpha(t-t')}} + e^{-\frac{(x+x')^2}{4\alpha(t-t')}} \right]$$

The most useful form of the solution is to insert equations 62 and 64 into 63 and carry out the integral over the spatial dimension leaving the time dimension for numerical integration so that arbitrary spectra can be accommodated. If this is done the general solution is:

$$65)\quad \rho CT(x,t) = \int_{t_{min}}^{t_{max}} K\, f(t') \left\{ Q_1(t',t,x) + Q_2(t',t,x) + Q_3(t',t,x) \right\} dt'$$

where

$$Q_1(t',t,x) = \frac{A_1}{2t'} \left[\mathrm{erf}\,(f_1) + \mathrm{erf}\,(F_2) \right]$$

$$Q_2(t',t,x) = A_2\,\frac{x}{2} \left[\mathrm{erf}\,(F_2) - \mathrm{erf}\,(F_1) - 2\,\mathrm{erf}(F_o) \right]$$

$$Q_3(t't,x) = A_2\,\frac{\sqrt{\alpha(t-t')}}{\sqrt{\pi}} \left[e^{-F_2^2} + e^{-F_1^2} - 2e^{-F_o^2} \right]$$

$$F_o = \frac{x}{2\sqrt{\alpha(t-t')}} \qquad F_1 = \frac{x_m - x}{2\sqrt{\alpha(t-t')}} \qquad F_2 = \frac{x_m + x}{2\sqrt{\alpha(t-t')}}$$

$$x_m = 2BE_o^{1/2}/t'C \qquad A_1 = \frac{CB}{E_o^{1/2}} \qquad A_2 = \frac{C^2}{2E_o}$$

$$t_{min} = B/\sqrt{E}_{min} \qquad t_{min} = B/\sqrt{E}_{max}$$

$$B = 2284 \times 10^{-9} \text{ R } A^{1/2} \qquad K = 1.6 \times 10^{-16}$$

with units

E_o = keV

C = keV/cm

A = particle mass, amu

R = wall radius, meters

α = thermal diffusivity, cm^2/sec

ρCT = J/cm^3

This analysis can be applied to any interaction in which Equation 60 is valid. This method has been applied to alpha particles bombarding carbon and tantalum with slowing down parameter (C, E_o) determined from calculations by Brice rather than using a formal Lindhard model. Reference to Figure 11 indicates the model is applicable for alpha particles up through about 600 keV. Extension to all energy ranges will be performed in subsequent studies.

Results of this calculation are shown in Figure 29 and 30. In Figure 30, the energy density profile is shown for various times for 10^{13} alpha particle/cm^2 with a 200 keV

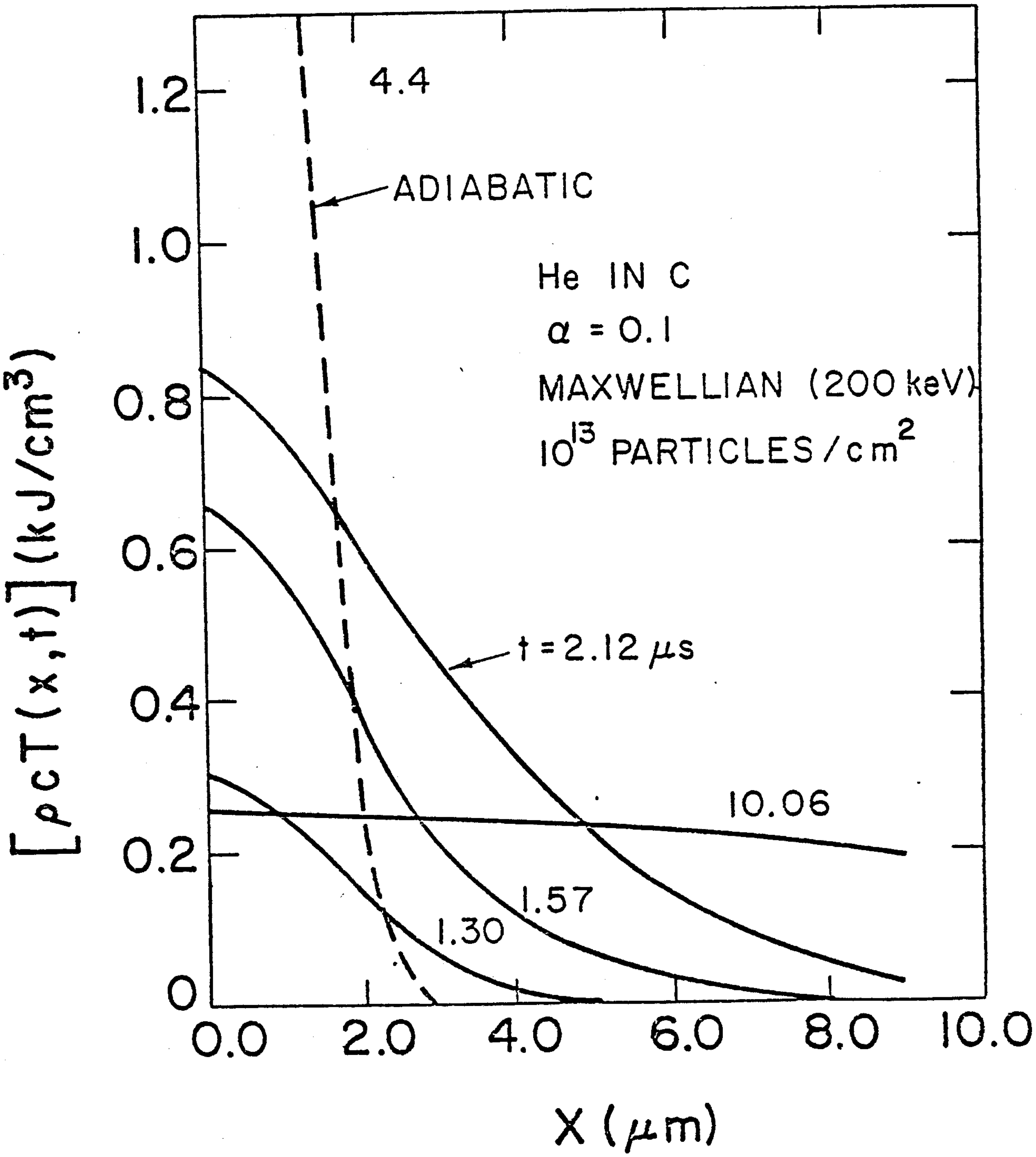

Fig. 29. Thermal Response to Ion Radiation

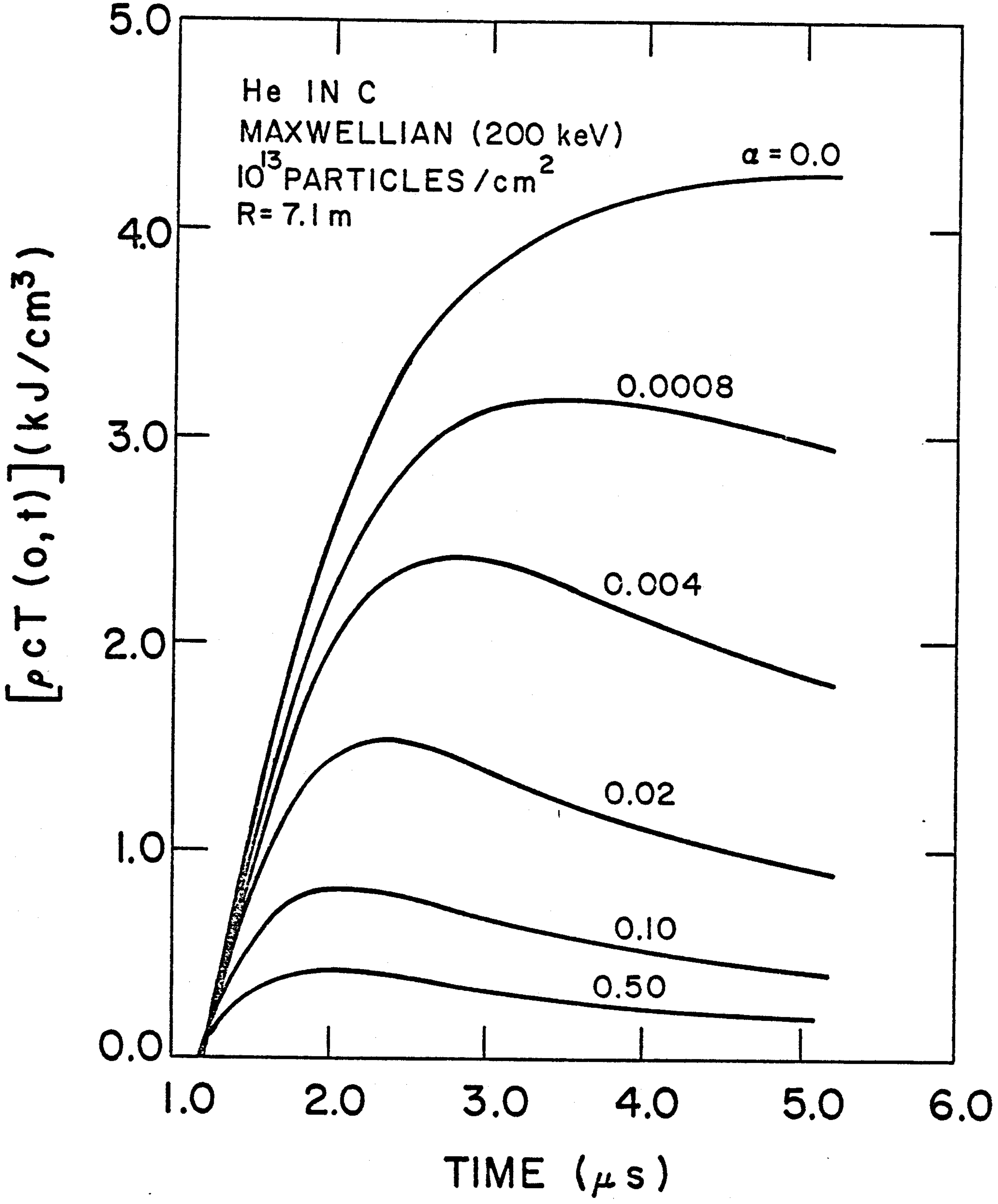

Fig. 30. Thermal Response to Ion Radiation as a Function of Thermal Diffusivity.

Maxwellian spectrum bombarding graphite at a radius of 7.1 meters. This calculation was done to analyze the response of magnetically diverted ions in the University of Wisconsin Laser Fusion Reactor Design.[62] The maximum energy density occurs at 2.12 μsec and is about 1/5 of the value obtained if no energy is lost during the pulse via conduction. Hence the adiabatic assumption is inappropriate in ion bombardment analyses. Figure 30 shows the front surface temperature as a function of time for various thermal diffusivities (conductivities). This analysis shows the sensitivity of the response to material properties (thermal conductivity) and again demonstrates the disparity between allowing reasonable heat conduction and the adiabatic ($\alpha = 0$) value.

This analysis is sufficiently general to include arbitrary spectra for particles described by the model, wall radii, and material properties. In addition, it requires a minimal amount of computer time and can therefore be used for parameter studies.

VI.4 Stress Response

Stresses will be produced in irradiated first walls by the momentum of the bombarding particles, the ablation of the exposed surface, and the thermoelastic response to the deposited energy.

The first of these effects is normally a negligible factor. An estimate of the magnitude of these stresses can be made by applying Equation 37 with the peak particle fluxes given in Figure 20. The pressures corresponding to these data are

neutrons $\underset{\sim}{\sim}$ 8×10^6 dynes/cm^2 = 8 atmospheres (max)
ions $\underset{\sim}{\sim}$ 1.5×10^4 = .015 atmospheres

The value for the neutrons is deceptive since only about 10% of the 14 MeV neutrons will have collisions in the first cm and each collision would represent only a few percent reduction in the momentum of the neutron, hence the real value is several orders of magnitude less than the above. High energy α particles, however, will contribute higher stress values. For example, 10^{13} /cm^2 of 3 MeV alphas deposited over 10 ns will yield about 8 atmospheres of normal stress on the first wall.

The stress developed due to ablation can be readily calculated with general material response numerical codes and will not be discussed here.

The third stress source, the thermoelastic response, can be estimated with methods of linear elasticity and thus is analytically tractable. The ability to develop solutions for a wide variety of energy depositions makes these methods interesting for parametric analyses.

The generation of thermoelastic stress waves is due to a thermodynamic requirement for a local expansion which occurs in a time which is short compared with the time for the material to relax.

The defining relations of thermally developed stress waves can be developed as follows:

In an isotropic material, the stress tensor is given as:

66) $$\sigma_{ij} = \lambda\, e_{\mu\mu}\, \delta_{ij} + 2\, Ge_{ij} - \beta\delta_{ij}\, \Theta$$

where $\beta = \frac{\alpha E}{1-2\nu} = (3\lambda + 2G)\alpha$

λ, G = Lame's constants

E = Young's modulus

ν = Poisson's Ratio

α = thermal coefficient of linear expansion

e_{ij} = strain tensor, $e_{\mu\mu} = e_{11} + e_{22} + e_{33}$

$\Theta = T - T_o$ where T_o = reference temperature in stressed state

In the case of uniaxial strain, this relation yields the axial stress in terms of the axial strain and temperature as:

$$\sigma = \lambda e + 2Ge - \beta\,\Theta$$

or

67) $$\sigma = (K + 4/3G)e - 3\alpha K\,\Theta$$ where K = Bulk modulus

$$K = \frac{E}{3(1-2\nu)}$$

$$e = \text{strain} = \frac{\partial u}{\partial x}$$

The equation of motion in one dimension is

68) $$\frac{\partial \sigma}{\partial x} = \rho\,\frac{\partial u^2}{\partial t^2}$$

Equations 67 and 68 can be combined to give the stress wave equation

69) $$\frac{\partial^2 \sigma}{\partial x^2} - \frac{1}{c^2}\frac{\partial^2 \sigma}{\partial t^2} = \frac{3\alpha K}{c^2}\,\frac{\partial^2 \Theta}{\partial t^2}$$

where c = dilational wave speed

$c^2 = (K + 4/3G)/\rho$

The temperature is given by a combination of the heat conduction equation and the energy equation as:

70) $$k\,\frac{\partial^2 \Theta}{\partial x^2} = \rho c\,\frac{\partial \Theta}{\partial t} + T\beta\,\frac{\partial e}{\partial t}$$

Equations 69 and 70 are coupled equations which express the relation between temperature and stress in a uniaxial strain system. These equations have been treated by many investigators. Most applications treat them in an "uncoupled" manner in which the last term in Equation 70 is ignored. This term represents the work done per unit volume by dilatational forces and is usually small in comparison with energy transfer by conduction.

A solution for step and ramp function temperature boundary-conditions on an infinite half space was developed by Sternberg and Chakravorty[64] while a complete coupled solution for exponentially increasing surface temperature was presented by Daimaruya and Naito.[65] White[66] treated a variety of surface temperature conditions.

For energy deposition into the material, Morland[67] developed a solution for electromagnetic radiation in a semi-infinite solid. This model was later extended to viscoelastic materials with Hegemier.[68] A specific application for laser irradiation was treated by Penner and Sharma.[69]

In the latter three papers the solutions were developed on the assumption that the propagation of stress waves occurs in times which are much shorter than the times for temperature relaxation. The creation of thermoelastic stress can only occur if the energy is deposited in times which are short compared with the time for a stress wave to transit the deposition region. Since wave velocities are on the order of 10^5 cm/sec, this corresponds to pulse durations which are less than

$$t_d < \ell/c$$

or

$$t_d < 10^{-8} \text{ sec}$$

for deposition over 10 μm intervals.

The amplitude of the stress generated by an instantaneous deposition can be determined from Equation 66 with the condition that $e_{ij} = 0$. In this case, for uniaxial strain

$$\sigma_1 = \beta\Theta \, , \qquad \beta = \frac{\alpha E}{1-2\nu}$$

for graphite[70]

$$\alpha = 8 \times 10^{-6} \, {}^{o}C^{-1}, \; E \simeq 2 \times 10^{6} \text{ psi} = 1.38 \times 10^{10} \text{ N/m}^2$$

$$\nu = .12$$

therefore

$$\sigma/\Theta = 21 \text{ psi}/{}^{o}C, \; .15 \text{ MN/m}^2 / {}^{o}C$$

For the photon, radiation deposited into graphite as shown in Figure 23, an intensity of $1 J/cm^2$ of .5 keV Blackbody radiation will yield a stress of 150 MN/m^2 (21000 psi).

This value is the initial compressive stress before the stress wave motion occurs. The amplitude of the rarefaction wave which develops as the wave propagates into the material is about 1/2 of this value.

These stress waves will be attenuated as they propagate into the material but they may be of sufficient magnitude to cause surface spallation or failure by producing fatigue crack growth.[71]

In this study a general formulation will be made based on the extension of the models discussed above to deposition profiles typical of photon and ion radiations and to deposition times characteristic of the source spectra with transit time broadening.

VI.5 Displacement Response

The radiation damage in a pulsed fusion first wall will be due to neutron and ion bombardment. The displacement rate from neutrons will be determined by the duration of the primary and back scattered neutron fluxes. The neutron damage, like the energy deposition, will also be uniformly distributed through the first wall, at least on a macroscopic scale. As discussed earlier approximately 50%-70% of the displacements will be due to the source neutrons.

The damage production by the ions will be limited to the first few microns near the exposed surface. The spatial extent of the damage will be determined by the amount of energy lost by the ion which is attributable to nuclear collisions at any location. The temporal behavior of the damage production will be determined by particle flux (Figure 20) at the surface since the slowing down time will normally be insignificant (10^{-12} seconds).

The amount of displacement damage by ions can be determined at any location in the material at which the energy of the ion is known by[72]

$$58)\qquad \dot{D}(x) = F_i(x) \int_{E_d}^{\Lambda E_i} \sigma(E_i, E)\ \nu(E)\ dE$$

where F_i = local ion flux at position x

E_d = effective displacement energy

ΛE_i = maximum PKA energy

σ = cross section for transfer of energy E to PKA from ion of energy E_i

$\nu(E)$ = number of displaced atoms from PKA of energy E

The local displacement rate can be estimated by assuming suitable cross sections in Equation 58 and integrating. The spatial distribution of damage however requires knowledge of the energy at a given location. Consequently, the transport equations for the ions must be solved with proper partitioning of nuclear and electronic energy losses and with consideration of the statistical variation in the particle's energy and hence penetration. This calculation of range and energy partitioning is done by the numerical techniques of Winterbon,[73] Brice,[74] or Manning and Mueller.[75]

The deposition of bombarding species is also determined by these methods since the expected value of the range parallel and normal to the ion's original path and the spatial moments are calculated.[76,77,78]

In this study a wide variation of incident ion energies must be evaluated if arbitrary pellet spectra are to be addressed. In addition, efficient calculations of both damage and ion implantation must be performed so that a comparison with thermal and stress response can be made without incurring excessive calculational costs. Consequently, approximations will be made to the solutions mentioned above in a manner similar to the energy deposition calculations discussed earlier. These approximations will then be used to determine the response for the ion spectra to be considered.

VI.6 Synergistic Response

The combination of the time and space dependent temperature, stress, and displacement responses which a material will exhibit in an inertially confined fusion reactor environment creates a multifold interaction problem. Some of the phenomena which will be influenced by the combination of these parameters include:

- Void Swelling - both nucleation and growth of voids due the neutron and ion damage production
- Creep - due to the equilibrium operating stresses
- Fatigue - due to the cyclic loading of the pulsed system
- Blistering - due to the agglomeration of gas bubbles near the irradiated surface
- Sputtering - due to ejection of near surface atoms by bombarding radiation fluxes
- Embrittlement - due to gas migration to grain boundaries and hardening of the atomic matrix due to dislocation build up.

Investigation of any of these phenomena will be possible after development of a general model for temperature, stress, and damage.

VI.6.1 Effect on Void Growth

The growth of voids in metals is typically modeled by methods similar to those employed in homogeneous chemical kinetics. These analyses are normally referred to as "rate theory".[79] This method was originally applied to quasi-steady state phenomena but is now being extended to include the transient effects of pulsed damage.[80]

The analysis consists of writing a set of rate equations for the vacancy and interstitial concentrations as:

$$\frac{dC_I}{dt} = \text{Production - recombination - leakage to sinks}$$

$$\frac{dC_V}{dt} = \text{Production - recombination - leakage to sinks}$$

where production includes radiation produced and thermally emitted.

Certain sinks like dislocations preferentially attract interstitials allowing the excess vacancies to migrate to neutral sites such as voids. The net swelling can be determined by the flux of vacancies to voids as given in the rate of change of void radius as:

$$\frac{dR}{dt} = \frac{\Omega}{R} \{ D_V \; [C_V - C_V^\circ \exp (\frac{2\gamma\Omega}{RKT})] \; - D_i C_i \}$$

where R = void radius
Ω = atomic volume
D_V = vacancy diffusivity
C_V = vacancy concentration
C_V° = equilibrium vacancy concentration
D_i = interstitial diffusivity
C_i = interstitial concentration
γ = surface energy

This equation is evaluated in conjunction with the rate equations for vacancy and interstitial concentrations with appropriate inclusion of sink and source strengths.

The temperature dependence of void growth is primarily due to the sensitivity of the diffusion coefficients and the equilibrium vacancy concentration. At low irradiation temperatures the vacancies are immobile and cannot aggregate before considerable recombination takes place, thus yielding low swelling. At high temperatures the equilibrium concentration of vacancies overwhelms those which are radiation produced and the voids are forced to dissolve via thermal emission. Consequently a peak swelling temperature occurs in which conditions are optimum for void growth. An example of this temperature dependence taken from reference 79 is shown in Figure 31. This peak temperature is predicted to increase with increasing damage rate by the rate theory model and this prediction is verified by experiments comparing reactor irradiation with ion bombardment.[8]

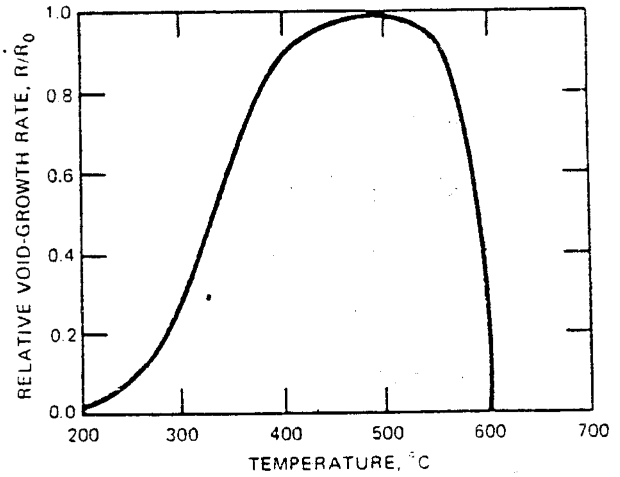

Fig. 31. Predicted Temperature Dependence of the Void-growth Rate in Stainless Steel Under Fast-neutron Irradiation. (After Ref. 79)

The temperature dependence discussed above cannot be compared directly with the temperature environment in a pulsed fusion first wall. The conditions for these analyses were constant temperatures and constant damage rate. In the pulsed environment there will be periods of high damage and constant temperature followed by periods of no damage and high temperature. In the latter case the thermal emission of vacancies from the voids during the period between irradiations (pulse annealing) can substantially reduce the void size before the defects from the subsequent damage pulse arrive at the void.

The previous temperature dependence is based on the assumption of a stress free material with no gas generation. The stress dependence of swelling can be seen if the void growth relationship by Brailsford and Bullough[79] is written as:

$$\dot{R} = \dot{R}_o \, F(n) + \dot{R}_e$$

where: $\dot{R}_o$ is the void growth rate without recombination and thermal emission

$F(n)$ is a factor containing the homogeneous recombination

$\dot{R}_e$ is the void shrinkage term which contains the effect of thermal emission

The presence of an internal gas pressure and finite stress affects only the thermal emission term, $\dot{R}_e$, which becomes significant at temperatures greater than the peak swelling temperature. Gas pressure and stress will affect the equilibrium concentration of vacancies and $\dot{R}_e$ can be written:[72]

$$\dot{R}_e = \frac{D_v C_v^{\circ} \Omega^2 Z_v \rho_d (\sigma + p - \frac{2\gamma}{R})}{RkT (Z_v \rho_d + 4\pi RN)}$$

where Z_v = combinatorial number for vacancies

ρ_d = dislocation density

σ = mean stress, + = tension, - = compression

p = gas pressure

N = void density

This factor, $\dot{R}_e$, is normally negative when $\frac{2\gamma}{R} > \sigma + p$, which results in void shrinkage; however, when $\sigma + p > \frac{2\gamma}{R}$ stress enhanced void growth occurs. Thus at high temperatures, stress (or large amounts of helium which would increase p) can cause significant modification to the swelling behavior. Examples of this stress dependence are shown in Figure 32 and 33.

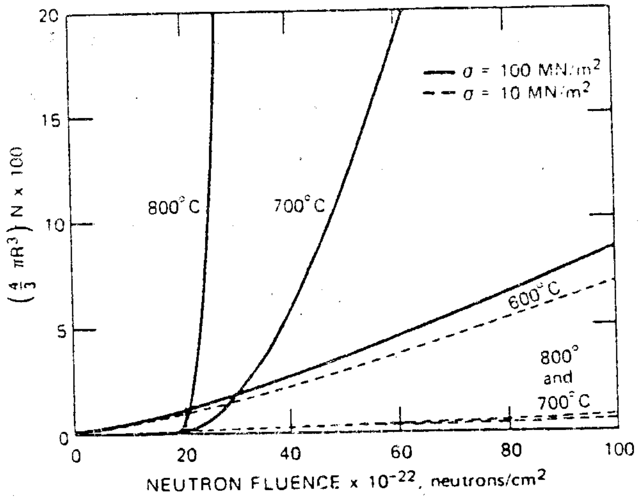

Fig. 32. Predicted stress-enhanced swelling for various stress levels and temperatures as a function of fluence. (Ref. 81)

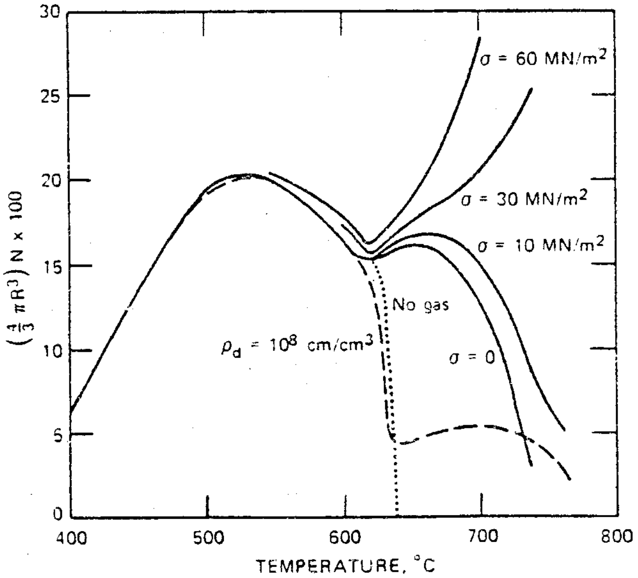

Fig. 33. Predicted temperature dependence of stress-enhanced void growth in steel. The solid curves apply to a dislocation density of 10^9 cm^{-2} and a helium production rate of 10^{-6} ppma/sec. (Ref. 72)

In a pulsed fusion environment the stress field in the first wall will be short in duration and alternate between compression and tension. Combination of these stress excursions with a dynamic rate theory model can be used to assess the effect of the thermoelastic stresses on void swelling.

An example of the synthesis of a general model for the temperature, stress and displacement conditions with a dynamic rate theory formulation is given in figure 34. The analysis sequence which would be followed is outlined and, in addition, the numerical techniques which are currently available for a detailed calculation of certain elements of the total analysis are listed. A self consistent analysis would consist of a general model incorporating the more pertinent aspects of each of these techniques. Specific comparisons between approximate analytical solution and specific numerical methods can be made to evaluate the validity of any phase of the calculation.

VI.6.2 Other Significant Effects

Numerous other effects due to the transient displacement, stress and temperature fields can be addressed. All possible combinations will not be considered in this study. An example of the more interesting phenomena is the implantation and diffusion of direct injected gas ions and transmutation gases.

Figure 34

ANALYSIS FLOW CHART

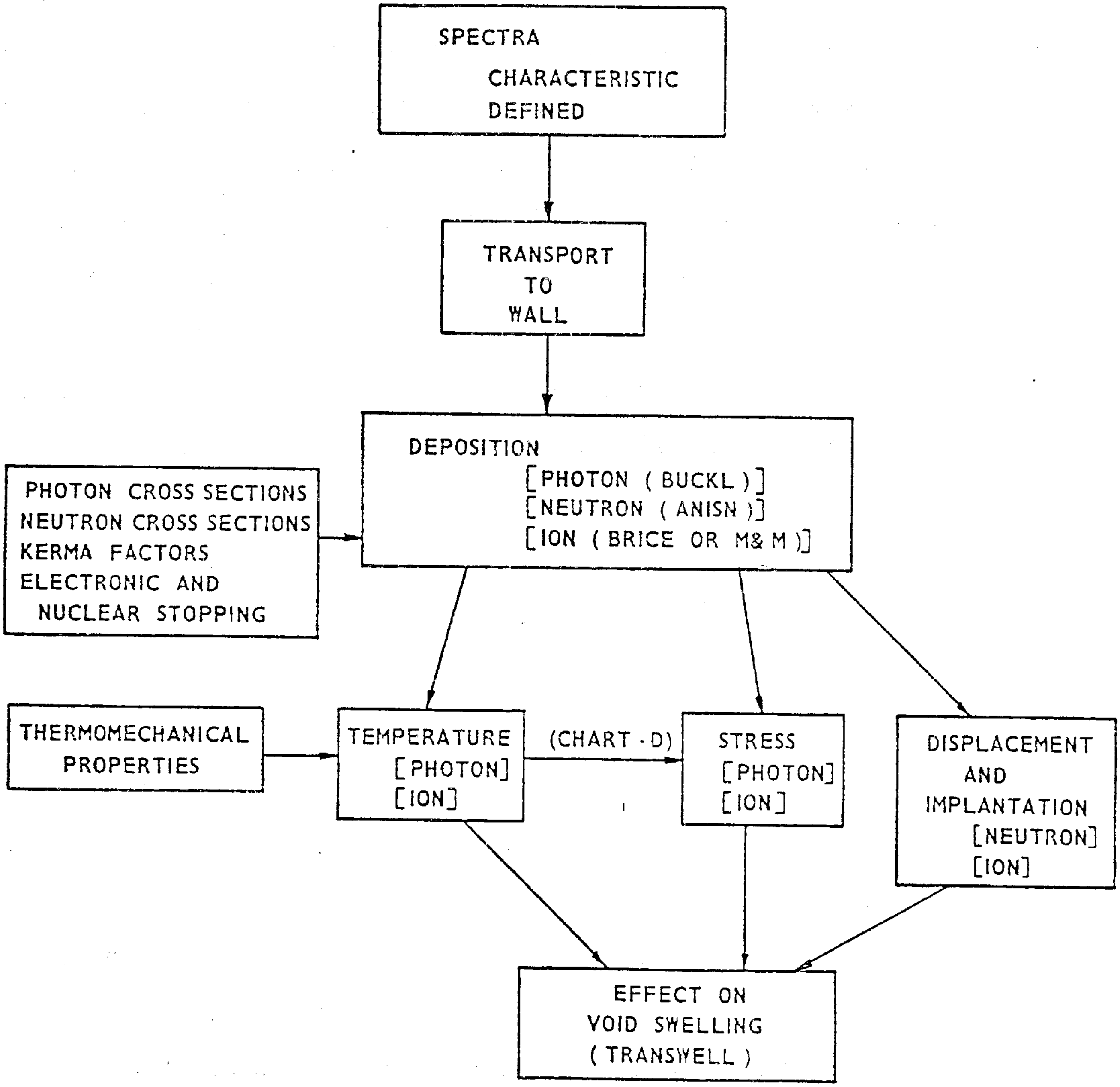

Another is the interaction of pulse heating and stress waves on the defect structure in a material. This phenomena has seen some investigation in recent times. Smidt and Metz[82] bombarded thin foils with a short pulse laser and found abnormally high concentrations of vacancies in nickel and vanadium. These vacancies condensed into voids in the nickel and faulted loops in vanadium. Analyses reveal that the vacancies could not be attributed entirely to quenching but perhaps to stress wave interactions.

In another related study, Muss[83] observed high dislocation loop densities in molybdenum which had been explosively loaded to a few hundred kilobars. Analysis revealed that the loops were primarily vacancy-type.

The ejection of micrometer-sized particles from the surface of a neutron irradiated material has been investigated by Guinan.[84] He concluded that shock waves and transient thermal stresses produced in near surface displacement cascades may be responsible for the emission of such particles.

These and other phenomena could lead to numerous investigations of various interactions based on the response conditions derived from this study.

Summary

This document has summarized the basic phenomena associated with transient irradiation of materials by thermonuclear sources. The mechanisms for nuclear and electronic interaction by charged particles, neutrons and photons are reviewed. Methods for determining the corresponding responses for temperature, stress and displacement damage are outlined.

Data were presented for the interactions and subsequent response of carbon for a wide range of photon and ion interactions. Further work will be to extend the investigation to other materials such as stainless steel, niobium, molybdenum, etc., and to extend the response models to all particle and photon spectra of interest.

These preliminary assessments have revealed that a complex interdependence exists between the radiation damage and the transient damage production and the transient temperature and stress state in a material. In addition, all effects will show a strong spatial dependence. The coupling of these term and space dependent phenomena will likely yield significant effects in materials on both a microstructural and macroscopic level. Future efforts will be devoted to quantification of these effects.

VIII. REFERENCES

1. Vook, F. L., et al.: Effects of Radiation on Materials; Physics Today, Sept. 1976.
2. Badger, B., et al.; UWMAK-III, A Non Circular Tokamak Power Reactor Design, Nuclear Engineering Dept. Report UWFDM-150, (Univ. of Wisconsin), July 1976.
3. An Engineering Design Study of a Reference Theta-Pinch Reactor (RTPR), Prepared for USAEC by Argonne National Laboratory and Los Alamos Scientific Laboratory, LA-5336 ANL-8019, March 1974.
4. Booth, L. A.; Central Station Power Generation by Laser-Driven Fusion; LA-4858, Vol. 1, Los Alamos Scientific Laboratory, February 1972.
5. Varnado, S. G.; et al.; Preliminary Systems Considerations for an Electron Beam Induced Fusion Power Plant, Sandia Laboratories, SAND-74-0160, 10/74.
6. Kulcinski, G. L.; Radiation Damage by Neutrons to Materials in DT Fusion Reactors, IAEA-CN-33/S 3-1; Reprint from Plasma Physics and Controlled Nuclear Fusion Research, 1974, Vol. II, International Atomic Energy Agency, Vienna, 1975.
7. Kulcinski, G. L.; et al.; Comparison of Displacement and Gas Production Rates in Current Fission and Future Fusion Reactors; Special Technical Production 570, American Society for Testing and Materials, 1976.
8. Johnston, W. G., et al.; Nickel Ion Bombardment of Type 304 Stainless Steel; Comparison with Fast Reactor Swelling Data; Journal of Nuclear Materials, No. 47, 1973, pp. 155-167.
9. Defects and Radiation Damage in Metals; Thompson, M. W.: Cambridge University Press, 1969.

10. Ghoniem, N. M., and Kulcinski, G. L.; "Void Growth Kinetics Under an Irradiation Pulse, UWFDM 138, December 1975.

11. Thompson, S. L.; Improvements in the CHART-D Energy Flow Hydrodynamic Code V, Sandia Laboratories, SLA-73-0477, Oct., 1973.

12. Holzhauser, P., and Lawrence, R. J., WONDY III--An Improved Program for Calculating Problems of Motion in one Dimension, Sandia Laboratories, SC-DR-68-217, June, 1968.

13. McMaster, W. H., et al.; Compilation of X-ray Cross Sections. Section I; UCRL-50174, California Univ., Livermore; Lawrence Radiation Lab., January 1970.

14. Biggs, Frank; Lighthill, Ruth; Analytical Approximation for X-Ray Cross Sections II, SC-PR-71 0507, Sandia Labs., Albuquerque, N. Mex., December 1971.

15. Handbook of Spectroscopy, Vol. I; Robinson, J. W.; CRC Press, Cleveland, Ohio.

16. The Atomic Nucleus; Evans, R. E.; McGraw-Hill, 1955. pp. 672-745.

17. Adams, K. G.; Biggs, F.; Efficient Computer Access to the Sandia Photon Cross Sections, SC-PR-72-0683, Sandia Labs., Albuquerque, N. Mex., December 1973.

18. Biggs, F.; Lighthill, R.; Analytical Approximations for Total and Energy Absorption Cross Sections for Photon-Atom Scattering; SC-PR-720685; Sandia Labs, Albuquerque, N. Mex., December 1972.

19. Jackson, J. D.; Classical Electrodynamics; 2nd Ed. John Wiley and Sons, 1975. pp. 284-292.

20. Hovingh, J.; First Wall Studies of a Laser-Fusion Hybrid Reactor Design; Proc. of 2nd Topical Mtg. on the Technology of Controlled Nuclear Fusion; Richland, Washington, 1976.

21. Principles of Optics; Born, Max and Wolf, Emil; 5th Ed., Pergamon Press, 1975.

22. Simmons, G. L.; Hubbell, J. H.; Comparison of Photon Interaction Cross Section Data Sets 11. Biggs-Lighthill and ENDF/B; NBS-10818, National Bureau of Standards, Washington, D.C., March 1972.

23. Simmons, G. L.: Hubbell, J. H.; Comparison of Photon Interaction Cross Section Data Sets VII. Biggs-Lighthill (Rev.) and ENDF/B; NBSIR 73-241, National Bureau of Standards, Washington, D. C., July 1973.

24. Handbook of Chemistry and Physics; CRC Press, Cleveland, Ohio.

25. Engle, W. W., Jr.; A Users Manual for ANISN, K-1693, Oak Ridge Gaseous Diffusion Plant, March 1967.

26. Cole, Randall K., Jr.; Buckl: A Program for Rapid Calculation of X-ray Deposition, SC-RR-69-855, Sandia Labs., Albuquerque, N. Mex., July 1970.

27. Radiation Damage in Crystals; Chadderton, Lewis T.; John Wiley and Sons, Inc.; New York.

28. Lindhard, J., et al.; Range Concepts and Heavy Ion Ranges; Mat. Fys. Medd. Dan. Vid. Selsk. 33, No. 14 (1963).

29. Chesire, J. M., Dearnaley, G.; and Jim Poate, Phys. Letters 27A, 318, 1968.

30. Brice, David K.; Three-Parameter Formula for the Electronic Stopping Cross Section at Non-relativistic Velocities, Vol. 6, No. 5, Physical Review A, November 1972.

31. Ion Implantation Range and Energy Deposition Distributions, Vol. 1, Brice, D. K.: IFI/Plenum, New York. 1975.

32. Ziegler, J. G.; Chu, W. K.; The Stopping of ^{4}He Ions in Elemental Matter, Thin Solid Films, 19 (1973), 281-287.

33. Northcliffe, L. C. and Schilling, R. F.; Range and Stopping-Power Tables for Heavy Ions; Nuclear Data Sec. Vol. 7, No. 3-4, 1970.

34. Oen, Ordean S. and Robinson, Mark T; Slowing-Down Time of Energetic Ions in Solids, Journal of Applied Physics, Vol. 46, No. 12, Dec. 1975.

35. Abdou, M. A., Maynard, C. W., and Wright, R. Q.; MACK: A Program to Calculate Neutron Energy Release Parameters (Fluence-To-Kerma Factors) and Multigroup Neutron Reaction Cross Sections from Nuclear Data in ENDF Format; ORNL-TM-3994, UWFD Memo 37.

36. Badger, B., et al.; UWMAK-I, A Wisconsin Toroidal Fusion Reactor Design; UWFDM-68, Nuclear Eng. Dept., Univ. of Wisconsin, (November 1973); Vol. 1.

37. Beranek, F. and Conn, R.; Time Dependent Neutronics and Photonics Analysis of ICTR; 7/21/76.

38. Kulcinski, G. L.; et al.; Radiation Damage Limitations in the Design of the Wisconsin Tokamak Fusion Reactor, Nuclear Technology, Vol. 22, April 1974.

39. Beranek, F. and Conn, R., Neutronics in UWICTR Liner and Wall; 11/3/76.

40. Hyde, Roderick, et al.; Physics and Engineering Considerations in Laser CTR Reactor Design; Proc of 1st Topical Mtg. on Technology of Controlled Nuclear Fusion, San Diego, Ca., 4/74, p. 154.

41. Finch, F. T., et al.; Laser Fusion Power Plant Systems Analysis; Proc. of 1st Topical Mtg. on Technology of Controlled Nuclear Fusion, San Diego, Ca., 4/74, p. 142.

42. Assessment of Laser-Driven Fusion; EPRI ER-203 (Research Project 470-1), Prepared by K. A. Brueckner and Assoc., Inc.; Electric Power Research Institute, Palo Alto, Ca.; September 1976.

43. Williams, J., et al.; A Conceptual Laser Controlled Thermonuclear Reactor Power Plant; Proc. of 1st. Topical Mtg. on Technology of Controlled Nuclear Fusion, San Diego, Ca., 4/74, p. 70.

44. Frank, T., et al.; A Laser Fusion Reactor Concept Utilizing Magnetic Fields for Cavity Wall Protection; Proc. of 1st Topical Mtg. on Technology of Controlled Nuclear Fusion, San Diego, Ca., 4/74, p. 83.

45. Hovingh, J., et al.; The Preliminary Design of a Suppressed Ablation Laser-Induced Fusion Reactor; Proc. of 1st Topical Mtg. on Technology of Controlled Nuclear Fusion, San Diego, Ca., 4/74, p. 96.

46. Maniscalco, J. A.; A Conceptual Design Study for a Laser Fusion Hybrid; Proc. of 2nd Topical Mtg. on Technology of Controlled Nuclear Fusion, Richland, Washington, 1976.

47. Varnado, Samuel, G. and Carlson, Gary, A.; Considerations in the Design of Electron-Beam-Induced Fusion Reactor Systems; Nuclear Technology, Vol. 29, June 1976.

48. Electron-Beam-Fusion Progress Report, Directorate of Physical Research 5200, Sandia Labs, Albuquerque, N. Mex., SAND76-0148, 1975.

49. Handbook of Physics; Condon, E. U., and Odishaw, H. Editors; 2nd Ed., McGraw-Hill, 1967. pp. 7-126 -- 7-138.

50. Williams, J. M., and Frank, T. G.; Laser-Controlled Thermonuclear-Reactor Materials Requirements; Nuclear Technology; Vol. 22; June 1974, p. 350.

51. Wolfer, W. G., Personal Notes of Slowing Down Time of the PKA's in Ni Produced by 14 MeV Neutrons; 7/15/76.

52. Lessor, D. L.: Neutron and Alpha Particle Energy Spectrum and Angular Distribution Effects from Plasma D-T Fusions BNWL-B-409, NTIS, 4/1975.

53. Shuy, G.; Calculations of neutron pulse spreading from D-T Pellet, Personal Communication, 9/1976.

54. Principle of Heat Transfer; Kreth, F; International, 1965.

55. Conduction of Heat in Solids; Carslaw, H. S. and Jaeger, J. C.: 2nd Ed., Oxford, 1959.

56. Abdel-Khalik, S. I., and Hunter, T. O.; Assessment of Surface Heating Problems in Laser Fusion Reactors; Submitted to Heat Transfer Conference-1977, January 1977.

57. Behrisch, R.; First-Wall Erosion in Fusion Reactors; Nuclear Fusion, No. 12, 1972, p. 695.

58. Effects of High-Power Laser Radiation; Ready, John F., Academic Press, New York, 1971.

59. Frank, T. G.; Heat Transfer Problems Associated with Laser Fusion; 16th National Heat Transfer Conference, St. Louis, Mo., August 1976.

60. Axford, R. A.; Direct Evaluation of Transient Surface Temperatures and Heat Fluxes; LA-6051, Los Alamos Scientific Lab., N. Mex., August 1975, p. 8.

61. Hovingh, J.; First Wall Response to Energy Deposition in Conceptual Laser Fusion Reactors; California Univ.; Livermore (USA). Lawrence Livermore Lab., February 1976, p. 13.

62. Conn, R. W., et al.; Studies of the Technological Problems of Laser-Driven Fusion Reactors -- Annual Report-1; reprint, Nuclear Engineering Dept., Univ. of Wisconsin, Madison (December 1976).

63. Foundations of Solid Mechanics; Fung, Y. C.; Prentice-Hall, Inc., 1965.

64. Sternberg, Eli and Chaknavorty, J. G.; On Inertia Effects in a Transient Thermoelastic Problem; Journal of Applied Mechanics, Vol. 26, No. 4, December 1959.

65. Daimaruya, Masashi and Naito, Masachika; A Transient Coupled Thermoelastic Problem in the Semi-Infinite Medium; Bulletin of the Japanese Society of Mechanical Engineers.

66. White, R. M.; Generation of Elastic Waves by Transient Surface Heating; Journal of Applied Physics; Vol. 34, No. 12, December 1963.

67. Morland, L. W.; Generation of Thermoelastic Stress Waves by Impulsive Electromagnetic Radiation; AIAA Journal, Vol. 6, No. 6, June 1968.

68. Hegemier, G. A., Morland, L. W.; Stress Waves in a Temperature-Dependent Viscoelastic Half-Space Subjected to Impulsive Electromagnetic Radiation; AIAA Journal, Vol. 7, No. 1, January 1969.

69. Penner, S. S., and Sharma, O. P.: Interaction of Laser Radiation with an Absorbing Semi-Infinite Solid Bar; Journal of Applied Physics, Vol. 37, No. 6, May 1966.

70. Fusion Reactor Studies: Potential of Low Z Materials for the First Wall; EPRI 115-2, Prepared by General Atomic Co.; Electric Power Research Institute, Palo Alto, CA,; September 1975.

71. Weertman, J.; Potential Fatigue Problems in First-Wall Laser-Controlled Fusion Reactors; LA-5664-MS; Los Alamos Scientific Laboratory, November 1974

72. Fundamental Aspects of Nuclear Reactor Fuel Elements, D. R. Olander, TID-26711-P1, USERDA, 1976.

73. Ion Implantation Range and Energy Deposition Distributions, Vol. 2., K. B. Winterbon, IFI/Plenum, New York. 1975.

74. Brice, D. K.; Spatial Distribution of Ions Incident on a Solid Target As a Function of Instantaneous Energy; Radiation Effects 1971, Vol. II, pp. 227-240.

75. Manning, I. and Mueller, G. P.; Depth Distribution of Energy Deposition by Ion Bombardment, Computer Physics Communication, 6, 1973.

76. Oen, O. S., et al.; Ion Radiation Damage, in Applications of Ion Beams to Metals, ed. by S. T. Picraux, E. P.

77. Schiott, Hans E.; Projected Ranges of Light Ions in Heavy Substances, Canadian Journal of Physics, Vol. 46, No. 6, March 1968.

78. Kaminsky, M.; et al.; Correlation Between Blister Skin Thickness, The Maximum in the Damage-Energy Distribution, and Projected Ranges of He$^+$ Ions in Metals: V; Journal of Nuclear Materials 59 (1976) 86-89.

79. Brailsford, A. D., and Bullough, R.; The Rate Theory of Swelling Due to Void Growth in Irradiated Metals; Journal of Nuclear Materials, No. 44, 1972, pp. 121-135.

80. Ghoniem, N., and Kulcinski, G.; Fully Dynamic Rate Theory (FDRT) Simulation of Radiation Induced Swelling of Metals; UWFDM-180, Dept. of Nuclear Eng., Univ. of Wisconsin, November 1976.

81. Brailsford, A. D., and Bullough, R.; Journal of Nuclear Matter, 48:87 (1973).

82. Smidt, F. A., Jr. and Metz, S. A.; Production of Vacancy Condensates by Laser Bombardment; Proceedings of 1971 International Conference on Radiation Induced Voids in Metal, Albany, New York, 1971.

83. Murr, L. E., Inal, O. T., and Morales, A. A.; Direct Observations of Vacancies and Vacancy-Type Defects in Molybdenum Following Uniaxial Shock-Wave Compression; Acta Metallurgica, Vol. 24, pp. 261-270, 1976.

84. Guinan, M.; Shock Wave Interactions Arising from Near Surface Displacement Cascades; Lawrence Livermore Laboratory, Univ. of Ca.; Livermore, Ca., UCRL-75286, January 1974.